Action-detected 2D spectroscopy

Technical development and practical applications

Amarotti, Edoardo

2025

Citation for published version (APA):
Amarotti, E. (2025). *Action-detected 2D spectroscopy: Technical development and practical applications*. Lund University.

Action-detected 2D specroscopy

Technical development and practical applications

EDOARDO AMAROTTI
CHEMICAL PHYSICS | FACULTY OF SCIENCE | LUND UNIVERSITY

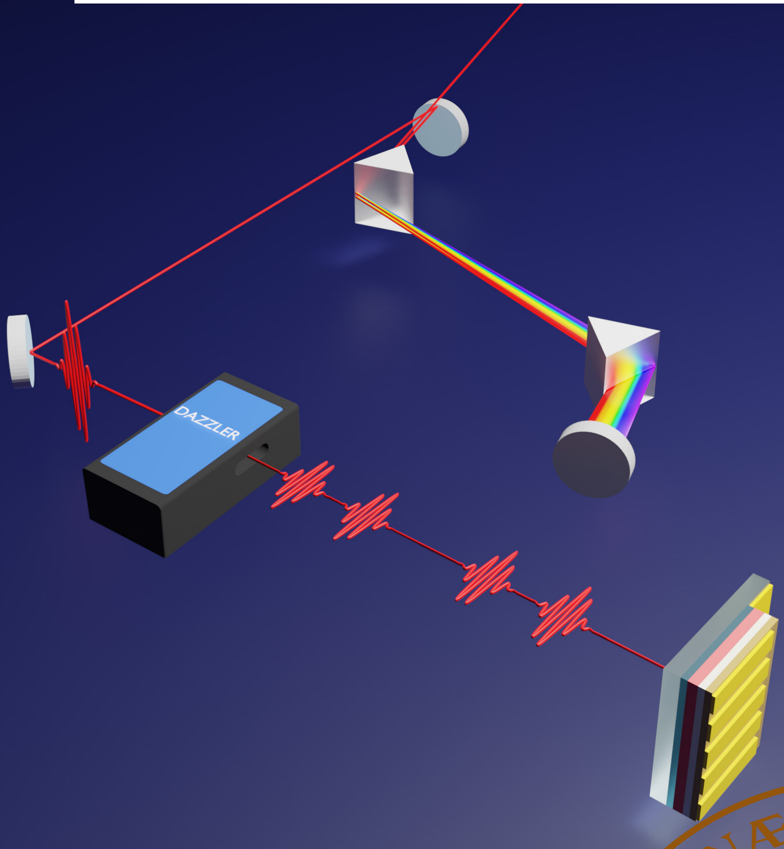

Printed by Media-Tryck, Lund 2025 NORDIC SWAN ECOLABEL 3041 0903

LUND UNIVERSITY

Faculty of Science
Department of Chemistry
Division of Chemical Physics

ISBN 978-91-8096-124-0

9 789180 961240

Action-detected 2D spectroscopy

Technical development and practical applications

Edoardo Amarotti

LUND
UNIVERSITY

DOCTORAL DISSERTATION
Thesis advisors: Prof. Tõnu Pullerits, Dr. Luca Bolzonello
Faculty opponent: Prof. Howe-Siang Tan

by due permission of the Faculty of Science, Lund University, Sweden.
To be defended at lecture hall KC:A at the Department of Chemistry on
Friday, the 7th of November 2025 at 9:00.

Organization
LUND UNIVERSITY

Department of Chemistry
Box 124
SE–221 00 LUND
Sweden

Document name
Doctoral dissertation

Date of disputation
2025-11-07

Sponsoring organization

Author(s)
Edoardo Amarotti

Title and subtitle
Action-detected 2D spectroscopy: Technical development and practical applications

Abstract

This doctoral thesis presents a comprehensive investigation into action-detected two-dimensional electronic spectroscopy (A-2DES), from the technical development of a state-of-the-art apparatus to its application in elucidating ultrafast dynamics in advanced materials and biological systems. The work is founded on the design and implementation of an A-2DES setup centered on a single acousto-optic pulse shaper, a configuration that offers inherent phase stability and compactness. A significant portion of this research was dedicated to the rigorous characterization and mitigation of instrumental artifacts, particularly pulse-shaper-induced nonlinearities and distortions arising from data acquisition protocols. The development of robust post-processing and background-subtraction strategies was crucial for ensuring the high fidelity of the spectroscopic data. The validated methodology was subsequently applied to three distinct systems, showcasing the versatility of coherent multidimensional spectroscopy. First, coherent 2DES was used to study a highly polydisperse ensemble of CdSe quantum dots, directly visualizing the effects of quantum confinement on the electronic structure and resolving the size-dependent biexciton binding energy, a key many-body interaction. Second, photocurrent-detected 2DES was employed to investigate operational perovskite solar cells, providing direct insight into how the A-site cation composition (formamidinium vs. methylammonium) influences sub-picosecond charge carrier cooling and relaxation dynamics. These measurements, performed on fully encapsulated devices, established a direct link between microscopic carrier dynamics and the functional photocurrent output, with a detailed kinetic model quantitatively describing the phonon-assisted intraband relaxation cascade. Finally, a comparative study of the light-harvesting complex II (LHCII) at cryogenic temperatures using both coherent- and action-detected 2DES revealed the complementary nature of these techniques. While coherent 2DES clearly mapped population relaxation and energy transfer pathways between chlorophyll states, the action-detected spectra were dominated by features attributed to incoherent mixing, providing a sensitive probe of efficient exciton-exciton annihilation. Collectively, this research establishes A-2DES not merely as an alternative to conventional coherent techniques but as a distinct and powerful tool that offers unique access to the functional dynamics and many-body interactions governing energy conversion and dissipation. The work presented herein provides a validated framework for A-2DES and demonstrates its broad utility in addressing fundamental questions in materials science and biophysics.

Key words
2D spectroscopy, action spectroscopy, quantum dots, perovskite, solar cell devices, LHCII

Classification system and/or index terms (if any)

Supplementary bibliographical information

Language
English

ISSN and key title

ISBN
978-91-8096-124-0 (print)
978-91-8096-125-7 (pdf)

Recipient's notes

Number of pages
138

Price

Security classification

I, the undersigned, being the copyright owner of the abstract of the above-mentioned dissertation, hereby grant to all reference sources the permission to publish and disseminate the abstract of the above-mentioned dissertation.

Signature ______________________ Date 2025-7-4

DOKUMENTDATABLAD enl SIS 61 41 21

Action-detected 2D spectroscopy

Technical development and practical applications

Edoardo Amarotti

LUND
UNIVERSITY

Cover illustration front: A schematic representation of the AOPDF pulse-shaper-based action-detected 2D electronic spectroscopy apparatus. This illustration was used as background of a poster presentation that was honored with a poster prize at the 2024 International Conference on Coherent Multidimensional Spectroscopy (CMDS) in York.

Funding information: The thesis work was financially supported by the European Union's Horizon 2020 research and innovation program under the Marie Skłodowska-Curie grant agreement no. 945378.

Lund University
Faculty of Science
Department of Chemistry
Division of Chemical Physics

ISBN: 978-91-8096-124-0 (print)
ISBN: 978-91-8096-125-7 (pdf)

Printed in Sweden by Media-Tryck, Lund University, Lund 2025

NORDIC SWAN ECOLABEL
Printed matter
3041 0903

Media-Tryck is a Nordic Swan Ecolabel
certified provider of printed material.
Read more about our environmental
work at www.mediatryck.lu.se

MADE IN SWEDEN

Dedicated to Giacomo, Giuseppe e Cristina

Contents

Multidimensional spectroscopy

Publications

List of publications

This doctoral thesis is based on the following publications, which will be referred to in the text by their Roman numerals.

I **Photocurrent detected 2D spectroscopy via pulse shaper: insights and strategies for optimally untangling the nonlinear response.**
E. Amarotti, L. Bolzonello, S.-H. Lee, D. Zigmantas, N.-G. Park, N. van Hulst, T. Pullerits
Opt. Express **2025**

I designed and built the experimental setup, contributed to the preparation of the samples, and carried out the measurements. I also performed the data analysis and wrote the majority of the manuscript.

II **Direct visualization of confinement and many-body correlation effects in 2D spectroscopy of quantum dots.**
E. Amarotti, Z. Wang, A. Hedse, N. Lenngren, K. Žídek, K. Zheng, D. Zigmantas, T. Pullerits.
Adv. Optical Mater. **2024**, 12, 2302968.

I performed the data analysis and wrote the majority of the manuscript.

III **Excited states and their dynamics in CdSe quantum dots studied by two-color 2D spectroscopy.**
Z. Wang, N. Lenngren, E. Amarotti, A. Hedse, K. Žídek, K. Zheng, D. Zigmantas, T. Pullerits.
J. Phys. Chem. Lett. **2022**, 13 (5), 1266–1271

I was involved in large part to the writing of the manuscript.

IV **Investigating organic A-cation influence on carrier dynamics of encapsulated perovskite solar cells using PC-2DES.**
E. Amarotti, L. Bolzonello, Q. Shi, S.-H. Lee, D. Zigmantas, T. Pascher, N.-G. Park, N. van Hulst, T. Pullerits
Manuscript

I carried out the measurements. I also performed the data analysis and wrote part of the manuscript.

V **Complementary insights into cryogenic LHCII dynamics: a comparative study of coherent and action-detected 2D electronic spectroscopies.**
E. Amarotti, A. Kumar, A. Sahu, M. Schenker, L. Bolzonello, D. Bina, D. Zigmantas, T. Pullerits
Manuscript

I carried out the measurements with co-authors. I also performed the data analysis and wrote majority of the manuscript.

All papers are reproduced with permission of their respective publishers.

Publications not included in this thesis:

VI **Beating signals in CdSe quantum dots measured by low-temperature 2D spectroscopy.**
Z. Wang, A. Hedse, E. Amarotti, N. Lenngren, K. Žídek, K. Zheng, D. Zigmantas, T. Pullerits.
J. Chem. Phys. **2024**, 157 (1), 014201.

VII **Harvesting a wide spectral range of electronic coherences with disordered quasi-homodimeric assemblies at room temperature.**
J. R. Hamilton, E. Amarotti, C. N. Dibenedetto, M. Striccoli, R. D. Levine, E. Collini, F. Remacle.
Adv. Quantum Technol. **2022**, 5, 2200060.

VIII **Time-frequency signatures of electronic coherence of colloidal CdSe quantum dot dimer assemblies probed at room temperature by two-dimensional electronic spectroscopy.**
J. R. Hamilton, E. Amarotti, C. N. Dibenedetto, M. Striccoli, R. D. Levine, E. Collini, F. Remacle.
Nanomater. **2023**, 13 (14), 2096.

Popular science summary

For a long time, the study of molecular interactions has faced a significant challenge. The beginning and end of a chemical reaction could be observed, but the incredibly fast, foundational steps in between remained a blur because they happen in a millionth of a billionth of a second. This research has been about building and applying a new kind of technique capable of capturing a ”movie” of these molecular events as they unfold. This method is the so called ultrafast spectroscopy. One of its more powerful version is the two-dimensional spectroscopy. Instead of a simple snapshot, it employs a sequence of ultra-short laser pulses to create a detailed map. This map not only shows the different energy levels in a material but also reveals how these energy levels are connected and how they interact. The specific version of this technique employed in this work is even more direct. Rather than just observing a faint flash of light that the material emits after being excited, it measures a real-world action it performs, such as the electricity it generates or the fluorescence it emits. This ”action-detected” approach provides a direct link between the initial flash of light and the function the material is designed to perform. A large part of this work was dedicated to building and perfecting this instrument. Like any high-precision tool, it is prone to errors and artifacts that can be mistaken for real signals. Methods were developed to correct these measurements, ensuring that the resulting data accurately reflected the properties of the materials themselves, not the idiosyncrasies of the machine. Once the tool was validated, it was directed at a few fascinating subjects. First, quantum dots, tiny semiconductor crystals so small that their properties are governed by quantum mechanics, were investigated by using the well-known 2D electronic spectroscopy (2DES). By studying a mixture of broadly size-distributed quantum dots, it was possible to see how their size directly changes their energy landscape. Next, the future of solar energy was addressed through the study of perovskite solar cells via action-detected 2D spectroscopy (A-2DES). These materials represent a new class of solar technology that promises both high efficiency and low production cost. The technique was used to look inside a fully operational solar cell, measuring the electrical current it produced as the signal. This allowed for the real-time observation of the very first steps in the conversion of sunlight into electricity. By changing the chemical composition of the perovskite material, it was possible to see how these initial, ultrafast steps were affected, providing clues for understanding the photophysics behind their high efficiency. Finally, one of nature's own masterpieces of solar technology was examined: the light-harvesting complex II (LHCII). This molecule is the primary antenna in photosynthesis and is exceptionally efficient at capturing photons. Here, the action-detected method was compared with the more traditional one. While the traditional method showed how energy flows through the complex, the action-detected method revealed traces of exciton-exciton annihilation. In essence, this work has been about creating a new window into the ultrafast world. By building a better tool and using it to observe the fundamental interactions of light and matter, the secrets of both cutting-edge technologies and nature's most refined systems can be uncovered.

Multidimensional spectroscopy

CHAPTER 1

Introduction

Light is Earth's primary energy input. It sets our climate and seasons, drives weather and water cycles, and powers the chemistry that builds living matter. Without sunlight, most ecosystems would stall; with it, they grow, reproduce, and evolve. It is possible to consider light as one of the elements on which the diet of every leaving species is based. The main reason is that almost all food begins with photosynthesis. Plants, algae, and some microbes use sunlight to turn water and carbon dioxide into sugars, then assemble those into starches, oils, and proteins. Animals eat that stored energy, and we eat plants and animals, so the calories in bread, fruit, milk, eggs, and meat are ultimately solar energy packaged in molecules. For practical purposes, to eat is to draw on sunlight: captured by producers, passed through food webs, and released by our metabolism as the energy that keeps us alive. Beyond life's spark, light carries a remarkable set of traits. It is the fastest messenger in the universe, yet it can be slowed and redirected by glass or water. It can be interpreted as waves that interfere and diffract, but can also be seen as discrete packets of photons, whose energies define its spectrum. It can be polarized and phased, it disperses into color, reflects from mirrors, and refracts through lenses. With these behaviors, light doesn't just illuminate, it encodes information about whatever it touches. Harnessed by science, those qualities become tools. With the advent of lasers in 1960,[1] light became an engineered resource, allowing control over wavelength, bandwidth, polarization, phase, beam shape, and timing, from continuous output to femtosecond pulses. Femtosecond laser pulses have revolutionized spectroscopy by allowing to directly observe molecular processes, such as energy transfer and molecular reactions, as they happen in real-time. Before these tools, spectroscopy was like looking at a series of still photographs; the beginning and final states of a system were visible, but the ultrafast motion in between was a blur. Femtosecond pulses act like an incredibly fast camera shutter, enabling to capture a sequence of these events and effectively create a ”movie” of the molecular action. This direct view makes it possible to track the precise sequence of events to distinguish what initiates a change from what follows. Concepts that were once largely theoretical, like the electronic coupling between different parts of a molecule, become directly observable phenomena.

The pursuit of resolving ever-faster molecular events has driven a continuous evolution in ultrafast spectroscopic techniques, constantly pushing the boundaries of what can be observed. Foundational methods like transient absorption (TA), [2,3] while powerful, often produce congested one-dimensional spectra where the dynamics of different processes overlap, making them difficult to disentangle. To overcome this fundamental limit, the field advanced toward more complex multidimensional techniques, most notably two-dimensional electronic spectroscopy (2DES), also known as coherent-2DES (C-2DES). [4,5] The primary advantage of 2DES is its ability to spread spectral information across a second frequency axis, generating cross-peaks that directly map the electronic couplings and energy transfer pathways between molecular states, thus making abstract concepts like coherence and dissipation directly observable. The frontier has been pushed even further with the development and refinement of action-detected 2DES (A-2DES), a powerful variant that offers distinct advantages. Instead of measuring the third-order signal generated by the system after the change of macroscopic polarization, A-2DES monitors a resulting action, such as fluorescence or photocurrent, which provides exceptional sensitivity and directly links the initial light-matter interaction to a specific functional outcome, making it uniquely suited for studying optoelectronic devices and biological systems.

1.1 Aim and outline

In this thesis I present the research carried out during my PhD, centered on the design, construction, and application of A-2DES. The work has two goals. First, to develop and rigorously characterize a state-of-the-art A-2DES apparatus based on a single acousto-optic pulse shaper, including the identification and mitigation of experimental artefacts to ensure high-fidelity data. Second, to use this instrument to investigate the ultrafast photophysics in two distinct, relevant systems: a functioning perovskite solar cell (photocurrent detection) and the isolated light-harvesting complex II, LHCII (fluorescence detection). Together, these studies provide new insight into charge generation in next-generation photovoltaics and excitonic coupling in biological light harvesting, while establishing a robust methodology for future work. The dissertation is organized as follows. Chapter 2 introduces key concepts in ultrafast optics and the properties of ultrashort laser pulses. Chapter 3 lays out the theoretical and practical framework of ultrafast spectroscopy, moving from nonlinear response theory to C-2DES, and culminating in a detailed introduction to A-2DES. Chapter 4 describes the A-2DES setup: integration of the acousto-optic pulse shaper, implementations for photocurrent and fluorescence detection, and the data-processing pipeline, including strategies to correct artefacts and safeguard spectral integrity. Chapter 5 reports C-2DES measurements on quantum dots with broad size dispersion, clarifying how inhomogeneity shapes coherent responses and spectral line shapes. Chapter 6 presents photocurrent-detected 2DES on a perovskite solar cell, tracing charge-carrier dynamics relevant to device operation. Chapter 7 presents fluorescence-detected 2DES on LHCII at cryogenic temperature, mapping excitonic interactions within the complex. Chapter 8 summarizes the main findings and outlines perspectives and opportunities for future research.

CHAPTER 2

Concepts of ultrafast optics

The light coming from the sun, or even a normal lightbulb, can be seen as a chaotic flood of photons, all heading in different directions and out of sync with each other. It's bright and useful for seeing, but the energy is scattered and unfocused. A laser does something remarkable: it organizes that chaos. It forces photons into a disciplined beam where they all travel in the same direction, with their waves perfectly aligned in the so called 'coherent' light. Instead of a chaotic crowd, a perfectly synchronized army marching in step is obtained. This order is what gives laser light its unique properties and intensity. A laser pulse then takes this a step further by chopping that organized beam into incredibly short, intense packets of energy. Imagine the power from a continuous stream being packed into a burst that lasts for just a femtosecond, a millionth of a billionth of a second. This creates a flash of immense power and precision, a tool made of light that can be used to do everything from cutting steel to observing chemical reactions as they happen.

In this chapter, concepts and elements of ultrafast optics are introduced to provide the theoretical background to understand the work developed in this thesis.

2.1 Laser pulse

The four Maxwell's equations represent the core of classical electromagnetism, elegantly describing the temporal and spatial evolution of electric and magnetic fields. From these principles emerges the concept of electromagnetic radiation, whose most fundamental form is the monochromatic wave oscillating through space with a single, pure frequency. By neglecting the spatial dependence, a monochromatic wave can be described mathematically as:[6]

$$E(t) = A\cos(2\pi\nu_0 t + \varphi) \tag{2.1}$$

where A, ν_0, and φ define amplitude, frequency and initial phase of the wave, respectively. The frequency (ν [Hz]) defines also the energy of the wave through the Planck-Einstein relation:

$$E = h\nu_0 = \frac{h\omega_0}{2\pi} \tag{2.2}$$

where h is the Planck constant[7] and ω_0 is the angular frequency ([rad/s]).

This equation masterfully bridges the wave nature of light with its particle-like (corpuscular) behavior, encapsulating the dual nature of light by relating the continuous oscillation of a wave to the discrete energy quanta, or photons, that it carries. Consequently, the frequency of the wave directly dictates the energy of its associated photons: higher frequencies yield higher-energy quanta, while lower frequencies correspond to lower-energy ones.

When two or more monochromatic waves overlap spatially and temporally, their inherent wave nature leads to interference, allowing the synthesis of more complex electromagnetic fields. The resulting polychromatic wave, formed by the superposition of multiple monochromatic components, can exhibit two distinct behaviors depending on the phase relationships between them. If the constituent waves are out of phase (incoherent superposition), as a crowd of people talking at once, their interference is random and chaotic, resulting in no discernible pattern. If, however, the multiple monochromatic waves are perfectly in phase (coherent superposition), like a choir singing in perfect unison, they can interfere constructively to create a short, intense, and well-defined burst of radiation. This second scenario provides a powerful phenomenological description of a laser pulse. It can be conceptualized as a precisely engineered polychromatic wave where a defined number of different monochromatic waves are phase-locked, marching in perfect step to create a single, unified pulse, as visualized in fig. 2.1. In this context, the duration of the laser pulse is intrinsically connected to the number of monochromatic components that constitute it: shorter pulses in time-domain correspond to broader spectral bandwidths in frequency-domain (fig. 2.2). For Gaussian-shaped pulses with perfectly coherent frequency components, this relationship is quantified by the time-bandwidth product (TBP):[8,9]

$$\mathrm{TBP} = \Delta\tau \cdot \Delta\nu = \frac{2\ln 2}{\pi} = 0.441 \tag{2.3}$$

where $\Delta\tau$ is the time duration of the laser pulse and $\Delta\nu$ is the frequency bandwith, both considered at the full width at half maximum (FWHM) of the spectrum in the respective domain. The shortest achievable pulse duration for a given bandwidth characterizes a transform-limited (TL) pulse. Since performing differentiation, integration, superposition,

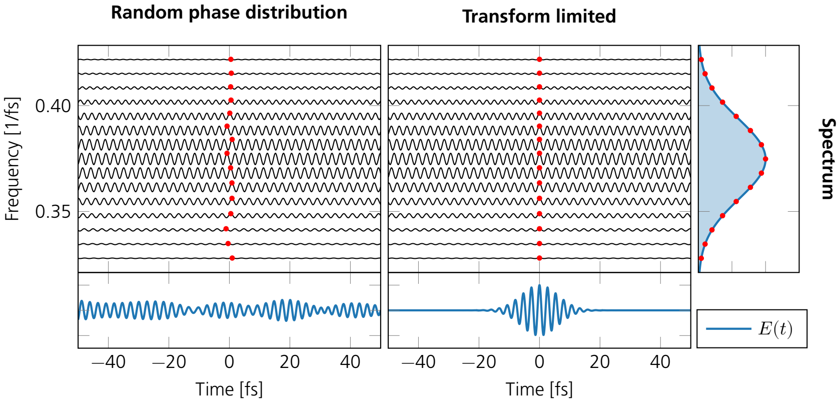

Figure 2.1: **The effect of phase coherence on the superposition of frequencies.** This figure describe how a temporal pulse is composed from a set of discrete frequency components. The left column depicts the incoherent superposition of the frequency components defined by the spectrum on the right side with randomized relative phases. Their superposition yields a low-intensity, continuous-wave-like signal. In contrast, if the same frequency components experience a coherent superposition, then at a fixed point in time, the corresponding waves are perfectly aligned and in phase. This will generate a short, high-intensity pulse in the time domain, which is characteristic of a TL pulse. The spectral amplitude distribution for the frequency components, which is identical for both scenarios, is displayed in the rightmost panel.

and Fourier analysis with trigonometric functions can become cumbersome, it is usually more convenient to switch to a complex representation. In this way it is possible to rewrite eq. 2.1 as follows[10]:

$$E(t) = \mathrm{Re}\{Ae^{-i\omega_0 t}\} = \mathrm{Re}\{|A|e^{i\varphi}e^{-i\omega_0 t}\} \tag{2.4}$$

with the complex amplitude A defined as:

$$A = |A|e^{i\varphi} \tag{2.5}$$

containing an amplitude term $|A|$ and a complex term containing the phase information φ. The complex amplitude is then multiplied to another complex quantity containing the oscillating term specified by the angular frequency ω_0.

When we consider multiple monochromatic waves located in the visible and adjacent spectral range, their coherent superposition allows generation of ultrashort laser pulses on the femtosecond scale (10^{-15} s). This superposition is expressed in a formula analogous to the one in eq. 2.4 where the polychromacity is reflected in a time dependence of the complex envelope[11,12]:

$$E(t) = \mathrm{Re}\{A(t)e^{-i\omega_0 t}\} = \mathrm{Re}\{|A(t)|e^{i\varphi(t)}e^{-i\omega_0 t}\} \tag{2.6}$$

Here, the complex amplitude in time-domain is defined as:

$$A(t) = |A(t)|e^{i\varphi(t)} \tag{2.7}$$

where $|A(t)|$ is the temporal amplitude and $\varphi(t)$ is the temporal phase. Also in this case, the complex amplitude is multiplied by the complex quantity containing the carrier frequency

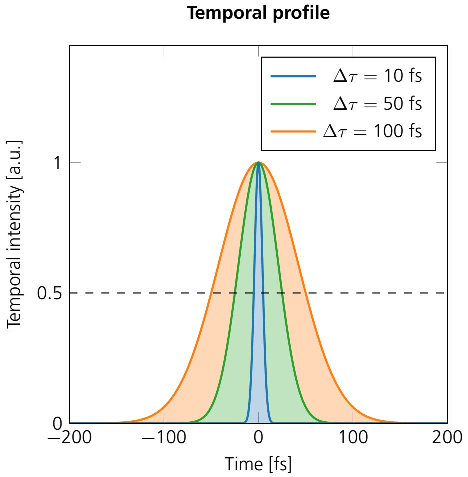

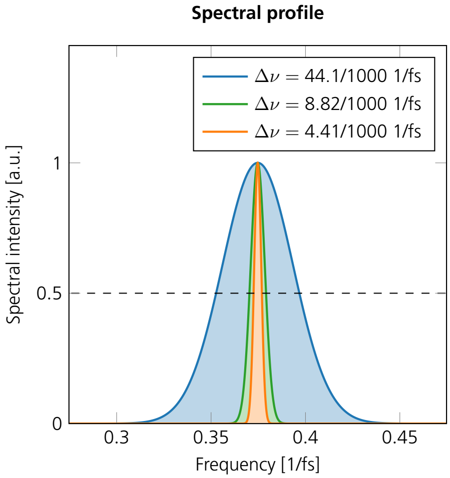

Figure 2.2: **Time-bandwidth relationship for Gaussian ultrashort pulses.** The figure illustrates how decreasing the pulse duration (left panel) broadens its spectral bandwidth in the frequency domain (right panel). This relationship follows the TBP described by Eq. 2.3.

ω_0, usually chosen to be close to the center of gravity of the spectrum. From comparison of eq. 2.4 with eq. 2.6, it is clear how the superposition of monochromatic waves in a ultrashort laser pulse gains a temporal dependence of the complex amplitude term: while for a monochromatic wave, the temporal envelope $|A|$ is constant and does not change over time, for an ultrashort pulse the same term gains a temporal dependence starting at zero, rising to a maximum, and then falling back to zero, confining the pulse to a very short duration; in a similar fashion, while for a monochromatic wave, the phase term φ is constant and does not change over time, for an ultrashort pulse the same term gains a temporal dependence which simply shapes how the carrier frequency evolves within the pulse. This concept will be presented in sec. 2.2.

As for the time-frequency relation in eq. 2.2, the pulse field in the frequency-domain is the Fourier transform of the time-domain field[13]:

$$\tilde{E}(\omega) = \int_{-\infty}^{\infty} E(t)e^{i\omega t}dt \tag{2.8}$$

while the inverse Fourier transform can bring us back to the time domain:

$$E(t) = \frac{1}{2\pi}\int_{-\infty}^{\infty} \tilde{E}(\omega)e^{-i\omega t}d\omega \tag{2.9}$$

Analogously to eq. 2.6, it is possible to decompose the electric field in the frequency-domain as:

$$\tilde{E}(\omega) = \mathrm{Re}\{A(\omega)\} = \mathrm{Re}\{|A(\omega)|e^{i\phi(\omega)}\} \tag{2.10}$$

Here, the complex amplitude in frequency-domain is defined as:

$$A(\omega) = |A(\omega)|e^{i\phi(\omega)} \tag{2.11}$$

where $|A(\omega)|$ is the spectral amplitude and $\phi(\omega)$ is the spectral phase. The complementary representations of ultrashort pulses in time (eq. 2.6) and frequency (eq. 2.10) domains are summarized graphically in fig. 2.3, where the concept of intensity is visualized: in time-domain, it represents the time-dependent instantaneous power of the pulse and in frequency-domain it defines the spectral intensity, which is the quantity that can be measured through a spectrometer.[14] Mathemathically, the intensity can be written for both domains as:

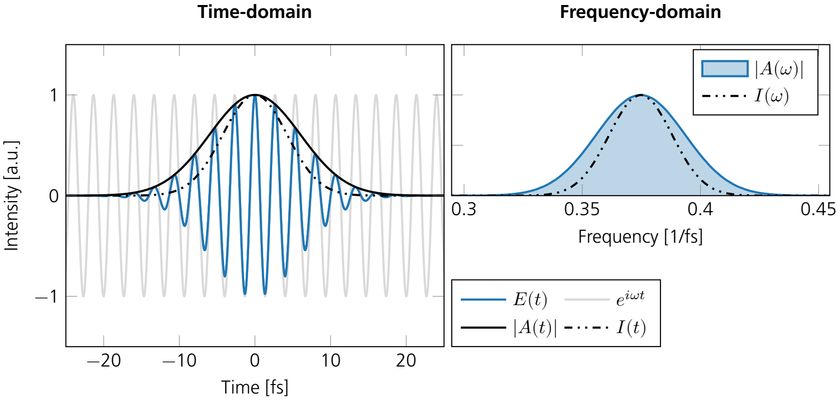

Figure 2.3: Ultrashort pulse representation in time and frequency domain. Time-domain (left) and frequency-domain (right) representations of an ultrashort gaussian pulse of 10 fs centered at 800 nm, highlighting the different components. .

$$I(t) = |A(t)|^2 \tag{2.12}$$

$$I(\omega) = |A(\omega)|^2 \tag{2.13}$$

In the next section, the implications of non-zero temporal and spectral phases will be explored.

2.2 Pulse dispersion

As an ultrashort pulse propagates through a dispersive material, the medium's frequency-dependent refractive index $n(\omega)$ causes the pulse's constituent frequencies to travel at different velocities:

$$\phi(\omega) = \frac{\omega}{c} n(\omega) L \tag{2.14}$$

where c is the speed of light in vacuum and L is the thickness of the dispersive material. Because of their intrinsically broad spectral content, ultrashort pulses are particularly sensitive to this effect: the resulting desynchronization between frequencies drastically alters their phase relationship, profoundly distorting the pulse's temporal structure Since the temporal profile is defined by the temporal phase $\phi(t)$, non-linear changes in time of this quantity, introduced by dispersion, will be reflected in time-dependent oscillation period of the electric field. Stated otherwise, the frequency changes with time during the pulse. It is possible to calculate this instantaneous frequency ω_{inst} by taking the time derivative of the total phase of the complex signal $E(t)$:

$$\omega_{\text{inst}} = \frac{d}{dt}[\omega_0 t + \varphi(t)] = \omega_0 + \frac{d\varphi(t)}{dt} \tag{2.15}$$

where ω_0 is the central carrier frequency and the term with the derivative of $\varphi(t)$ determines the time varying phase. Therefore, as visualized in fig. 2.1, for each phase shift of different frequency components $\phi(\omega)$ in the ultrashort pulse, the temporal shape will change accordingly. In fig. 2.4 is shown the effect of the dispersion on a 10 fs pulse centered at 800 nm, for which 3 mm fused silica introduced dispersion that broadens the pulse in time, reducing then its peak intensity. Even if it is difficult to notice by eye, the dispersed pulse is not symmetric, which reflects all the higher orders coming by the decomposition of the phase components from eq. 2.6 and eq. 2.10 by using a Taylor series expansion around the

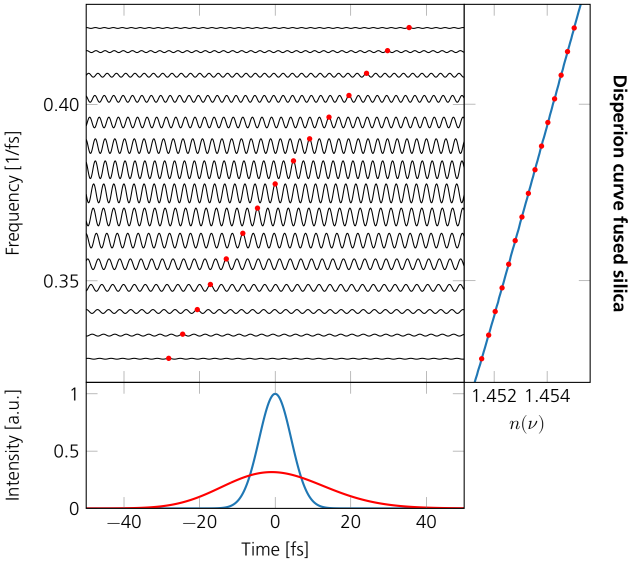

Figure 2.4: Ultrashort pulse broadening through dispersive material. The figure simulates broadening of a 10 fs pulse centered at 800 nm through a 3 mm of fused silica. The dispersion curve for the fused silica is reported on the right side of the figure for the frequency range of interest. On the left side, it is reported the phase shift of some of the frequency component within the spectral range of the pulse, where a red dot has been placed on the maximum point of each wave that was perfectly in phase before the transmission through the material. The shift has been visualized symmetric in respect to the central wavelength even if in real life scenario all the frequency components would have been delayed in time. On the bottom panel, the initial pulse is reported in blue and the dispersed pulse is reported in red. For the dispersed pulse, the group delay contribution was not considered so that the pulse can be still centered at 0 fs.

central frequency (ω_0) in frequency-domain[15]:

$$\phi(\omega) = \sum_{k=0}^{\infty} \frac{1}{k!} \left. \frac{d^k \phi(\omega)}{d\omega^k} \right|_{\omega_0} \cdot (\omega - \omega_0)^k \tag{2.16}$$

or around the pulse center (t_0) in time-domain:

$$\varphi(t) = \sum_{k=0}^{\infty} \frac{1}{k!} \left. \frac{d^k \varphi(t)}{dt^k} \right|_{t_0} \cdot t^k \tag{2.17}$$

0th order For $k = 0$, the solution of eq. 2.16 and eq. 2.17 is expressed by a constant term which is identical for both domains due to Fourier transform linearity[16]:

$$\phi_0 = \varphi_0 \tag{2.18}$$

In both cases, this quantity is called carrier envelop phase (CEP) which defines the phase between a specific point in the envelope of the electric field and the carrier.

1st order For $k = 1$:

$$\phi(\omega) = \left. \frac{d\phi(\omega)}{d\omega} \right|_{\omega_0} \cdot (\omega - \omega_0) \tag{2.19}$$

$$\varphi(t) = \left. \frac{d\varphi(t)}{dt} \right|_{t_0} \cdot t \tag{2.20}$$

In the frequency domain, the linear phase term corresponds to the group delay (GD), which manifests as a temporal shift of the entire pulse without altering its shape or duration. Physically, this means that all frequency components are delayed by the same constant amount, resulting in a uniform temporal displacement. Importantly, the temporal envelope of the pulse remains unchanged, where only its position in time is affected. Analogously, in the time domain, a linear temporal phase imparts a constant frequency shift (or spectral translation) to the pulse, effectively moving its central frequency without modifying the overall spectral bandwidth. In both cases, the operation corresponds to a simple shift, either in time or frequency, without introducing any distortion or broadening with the pulse retaining its original shape in the complementary domain.

2nd order For $k = 2$:

$$\phi(\omega) = \frac{1}{2} \cdot \left. \frac{d^2 \phi(\omega)}{d\omega^2} \right|_{\omega_0} \cdot (\omega - \omega_0)^2 \tag{2.21}$$

$$\varphi(t) = \frac{1}{2} \cdot \left. \frac{d^2 \varphi(t)}{dt^2} \right|_{t_0} \cdot t^2 \tag{2.22}$$

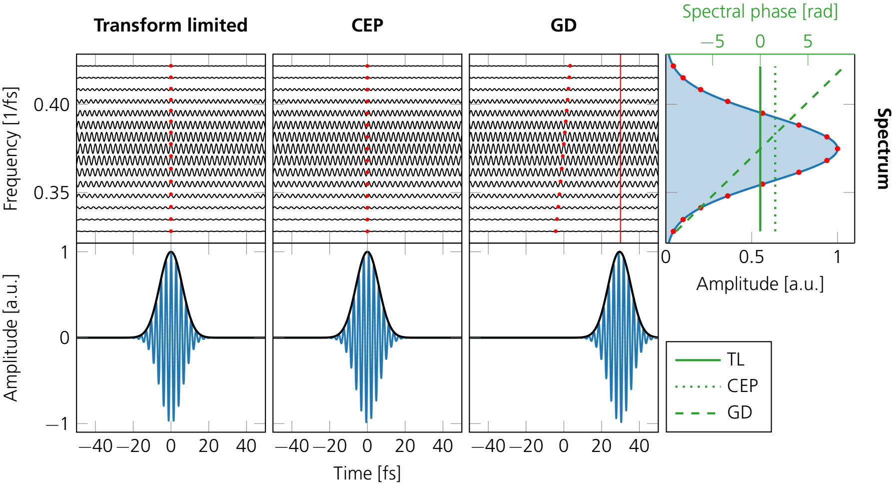

Figure 2.5: Effect of CEP and GD on transform limited pulse. This figure illustrates the concept of CEP and GD. The panel on the right reports a transform limited pulse with a flat spectral phase. The influence of CEP = $\pi/2$ is a constant phase offset across all frequencies that determines the precise timing of the carrier wave's oscillation within the envelope, thus altering the field's maximum at a given point in time. The influence of GD = 30 fs corresponds to a simple temporal shift of the entire pulse envelope, given by a linear and non-flat spectral phase Red markers on the frequency component diagrams highlight how spectral phase deviations, relative to the TL case, modify pulse structure across various dispersion orders.

In the frequency domain, the quadratic phase term represents the effect of group delay dispersion (GDD), a phenomenon where different spectral components of a pulse experience frequency-dependent delays. More precisely, each frequency component is delayed by an amount that increases linearly across the spectrum. As a result, an initially short and temporally well-localized pulse undergoes temporal broadening as it propagates through a dispersive medium. This broadening introduces a chirp, meaning that the instantaneous frequency of the pulse in the time domain is no longer constant but varies continuously throughout its duration. When the GDD is positive, higher frequencies lag behind lower ones, resulting in a pulse that stretches and develops an up-chirp, a gradual increase in frequency over time. Conversely, for negative GDD, lower frequencies are delayed more, producing a down-chirp where the frequency decreases with time. In both cases, the pulse becomes longer and less intense, with the sign of GDD determining the direction of the frequency sweep. Analogously, from the time-domain perspective, the quadratic phase term results in spectral broadening: the pulse's frequency content spreads out due to the time-varying phase, mirroring the way temporal duration increases due to dispersion in the spectral domain.[12]

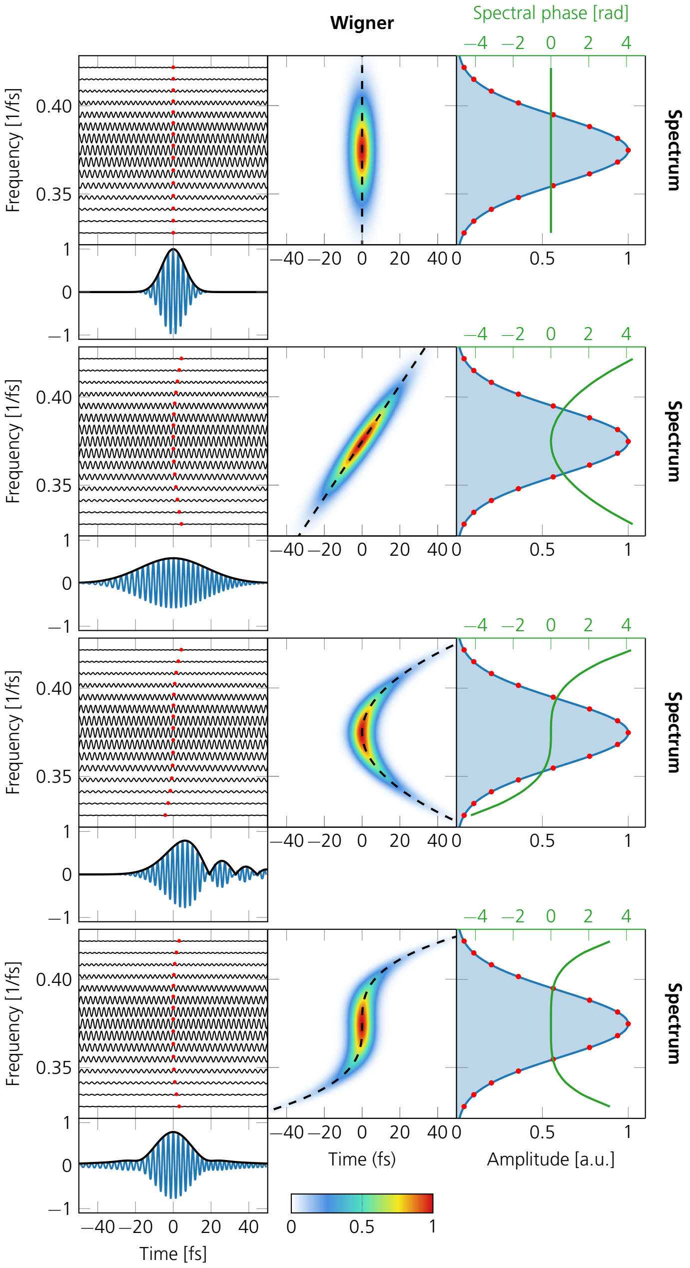

Figure 2.6: Visualization of how increasing orders of spectral phase dispersion affect an ultrashort laser pulse. This figure shows the effect of different orders of spectral phase dispersion on an ultrashort pulse. From top to bottom, it displays: an ideal, TL pulse; a linearly chirped and broadened pulse from GDD = +100 fs^2; an asymmetric pulse with post-pulses from TOD = +1000 fs^3; and a complexly distorted pulse with satellite peaks from FOD = +10000 fs^4. The central Wigner distributions, with the dotted group delay relation drawn on top, visualize these effects as a progressive tilting, curving, and twisting of the pulse in the time-frequency domain.Red markers on the frequency component diagrams highlight how spectral phase deviations, relative to the TL case, modify pulse structure across various dispersion orders.

3^{rd}, 4^{th} and higher orders For $k > 2$:

$$\phi(\omega) = \frac{1}{6} \cdot \left. \frac{d^3\phi(\omega)}{d\omega^3} \right|_{\omega_0} \cdot (\omega - \omega_0)^3 + \frac{1}{24} \cdot \left. \frac{d^4\phi(\omega)}{d\omega^4} \right|_{\omega_0} \cdot (\omega - \omega_0)^4 + \cdots \tag{2.23}$$

$$\varphi(t) = \frac{1}{6} \cdot \left. \frac{d^3\varphi(t)}{dt^3} \right|_{t_0} \cdot t^3 + \frac{1}{24} \cdot \left. \frac{d^4\varphi(t)}{dt^4} \right|_{t_0} \cdot t^4 + \cdots \tag{2.24}$$

Beyond second-order effects, higher-order phase distortions are typically analyzed in the frequency domain, as the spectral phase is much easier to measure than the corresponding temporal field.[16] Nevertheless, it is insightful to generalize that higher-order dispersion manifests in the time domain as increasingly complex, non-uniform variations in instantaneous frequency across the pulse, resulting in rich temporal dynamics beyond simple broadening or linear chirp. In frequency domain, the first and second term of eq. 2.23 show the cubic and quartic phase which can be called third order dispersion (TOD) and fourth order dispersion (FOD), respectively. TOD introduces significant asymmetry in the time domain. It leads to pulse distortion characterized by oscillatory substructures, often appearing as pre-pulses or post-pulses, depending on the sign of the dispersion. For a positive sign, physically this corresponds to a scenario where the central frequency arrives earlier, while frequency components on either side are delayed, creating temporal interference patterns and chirp asymmetry. FOD, on the other hand, produces a more symmetric temporal distortion, manifesting as broadening with extended tails on both sides of the pulse. The dispersion features described are displayed in fig. 2.5 and fig. 2.6.

CHAPTER 3

Principles of nonlinear spectroscopy

Normally, when light hits an object, the interaction is usually simple and predictable. A mirror reflects the object in front of it, a prism splits white light into a rainbow, and the response is directly proportional to the input light. It's like gently tapping a bell: it rings with a clear, expected note. This is the world of linear optics, where materials behave in a straightforward way. But when an intense light from a laser pulse is used, the rules change. Hitting that same bell with an incredibly powerful and short strike doesn't just make it ring, but it can results in new harmonics and overtones, a response that is no longer simple or proportional. This is nonlinear optics. The light is so strong that it fundamentally alters the material it passes through, forcing it to "talk back" in unexpected ways, even creating new colors of light that weren't there to begin with.

Nonlinear spectroscopy is the art of listening to this complex conversation. Instead of just hearing the fundamental note, it is possible to analyze all the rich echoes and overtones to learn far more about the bell itself: the system under investigation. To do this, several techniques that employs a sequence of laser pulses have been developed. In this thesis work, the focus is on 2DES, where a series of multiple pulses gently perturbate the system: first two interactions excite the sistem while the subsequent "probes" how the system has reacted. By systematically varying the delays between these pulses, it is possible to create a 2D map of the system's energy landscape. On this map, peaks along the diagonal show the fundamental states, or the "notes" the system can play. But the real power of the technique is in the off-diagonal cross-peaks. These are the signatures of the echoes, the crosstalk between different states. In fact, they show directly which parts of a molecule are connected and how energy flows between them. It is possible to retrieve this response in different ways. In C-2DES, it is directly recorded as the coherent light signal emitted by the system. A more recent technique, A-2DES, is more indirect: instead of the echo itself, the measured observable this time is a population related one, like fluorescence or photocurrent. This chapter charts a course through the fundamental principles of nonlinear spectroscopy, progressing from its core concepts to a detailed exploration of the third- and fourth-order processes that govern the powerful C-2DES and A-2DES techniques central to the work of this thesis.

3.1 Light-matter interaction

The interaction of light and matter, central to spectroscopy, is often described within a semiclassical framework: the material system is treated quantum mechanically, while light is modeled as a classical electromagnetic field.[17,18] In this picture, the field acts as an external perturbation that drives transitions between quantum states without explicitly tracking the state of light. Since the experiments presented here focus on the material response, the quantum fluctuations of light can be neglected, and the field treated classically. This approximation greatly simplifies the problem, allowing attention to be restricted to the quantum dynamics of matter while avoiding the complexities of quantized fields. An applied electric field induces a polarization P in the dielectric, which in turn modifies the field. Their relationship, neglecting spatial dependence, is expressed by the electric displacement vector, D:

$$D = \epsilon_0 E + P \tag{3.1}$$

Here, the constant ϵ_0 is the vacuum permittivity, E is the macroscopic electric field and P is the polarization of the material.[19] The polarization induced in the material can be written as a power series expansion of the electric field:

$$\begin{aligned} P(t) &= \epsilon_0[\chi^{(1)}E(t) + \chi^{(2)}E^2(t) + \chi^{(3)}E^3(t) + \dots] \\ &= P^{(1)}(t) + P^{NL}(t) \end{aligned} \tag{3.2}$$

In this expansion, $\chi^{(n)}$ represents the electric susceptibility tensor of the n^{th} order.[20] Linear optical effects, such as absorption and refraction, arise from the first-order polarization response $P^{(1)}(t)$. In contrast, nonlinear optical phenomena originate from higher-order contributions, collectively described by the nonlinear polarization $P_{\mathrm{NL}}(t)$. These terms become significant only under strong electric fields, such as those generated by ultrafast laser pulses. Among them, the third-order polarization, $P^{(3)}(t)$, represents the lowest-order nonlinear response capable of accessing the dynamics of excited states. Within Maxwell's wave equation, this nonlinear polarization acts as a source term, giving rise to new electric fields generated by the interaction of intense light with matter.[19,21] These fields constitute the spectroscopic signal detected in experiments:

$$\nabla^2 E(t) - \mu_0 \frac{\partial^2 D^{(1)}(t)}{\partial t^2} = \mu_0 \frac{\partial^2 P^{NL}(t)}{\partial t^2} \tag{3.3}$$

3.2 Time-dependent wavefunction evolution

A time-dependent quantum mechanical framework is crucial for describing the time-resolved measurements inherent to time-resolved spectroscopy. The evolution of a system's state, represented by its wavefunction $|\Psi(t)\rangle$, is dictated by the time-dependent Schrödinger equation:

$$\frac{d|\Psi(t)\rangle}{dt} = -\frac{i}{\hbar}\hat{H}(t)|\Psi(t)\rangle \tag{3.4}$$

When the Hamiltonian $\hat{H}$ does not change with time, the solution is obtained by applying the time-evolution operator, $\hat{u}(t, t_0)$, to the state at an initial time, $|\Psi(t_0)\rangle$ [22]:

$$|\Psi(t)\rangle = e^{-\frac{i}{\hbar}\hat{H}(t-t_0)}|\Psi(t_0)\rangle = \hat{u}(t, t_0)|\Psi(t_0)\rangle \tag{3.5}$$

where the time-evolution operator $\hat{u}(t, t_0)$ is defined as:

$$\hat{u}(t, t_0) \overset{\text{def}}{\equiv} e^{-\frac{i}{\hbar}\hat{H}(t-t_0)} \tag{3.6}$$

The time-evolution operator $\hat{u}(t, t_0)$ plays a central role in determining the temporal dynamics of a quantum system. Specifically, it enables the propagation of an initial state $|\Psi(t_0)\rangle$ at time t_0 to a later time t, encapsulating the full time dependence of the system's evolution. Therefore, it is essential to know the equation of motion for the time-evolution operator, which is derived by substituting eq. 3.6 into the time-dependent Schrödinger relation described in eq. 3.4. This yields:

$$\frac{\partial \hat{u}(t, t_0)}{\partial t} = -\frac{i}{\hbar}\hat{H}(t)\hat{u}(t, t_0) \tag{3.7}$$

which governs the time evolution of the operator $\hat{u}(t, t_0)$ and, consequently, the evolution of any arbitrary initial wavefunction $|\Psi(t_0)\rangle$, with relaxed restrictions of the time-independent Hamiltonian. By solving this equation, one can obtain the state of the system at any later time $t > t_0$, assuming the Hamiltonian $\hat{H}(t)$ is known. Eq. 3.7, when solved by integration using an iterative scheme, leads to:

$$\begin{aligned}\hat{u}(t, t_0) - \hat{u}(t_0, t_0) &= \frac{i}{\hbar}\int_{t_0}^{t} d\tau\ \hat{H}(\tau)\hat{u}(\tau, t_0) \\ &= \frac{i}{\hbar}\int_{t_0}^{t} d\tau\ \hat{H}(\tau)\left[1 - \frac{i}{\hbar}\int_{t_0}^{t} d\tau'\ \hat{H}(\tau')\hat{u}(\tau', t_0)\right]\end{aligned} \tag{3.8}$$

Repeating this iterative procedure n times yields to the generic solution:

$$\hat{u}(t, t_0) = 1 + \sum_{n=1}^{\infty} \left(-\frac{i}{\hbar}\right)^n \int_{t_0}^{t} d\tau_n \int_{t_0}^{\tau_n} d\tau_{n-1} \dots \int_{t_0}^{\tau_2} d\tau_1 \; \hat{H}(\tau_n) \dots \hat{H}(\tau_2)\hat{H}(\tau_1) \quad (3.9)$$

To ensure the integrals reflect the forward progression of time, the temporal integration variables, which were initially ordered from t down to t_0 in eq. 3.8, had been relabeled into a chronological sequence, as visualized in fig. 3.1. The situation is more intricate for a time-dependent Hamiltonian, as is the case in spectroscopy where a light field perturbs the system. The total Hamiltonian is divided into a time-independent part, $\hat{H}_0$, representing the unperturbed system, and a time-dependent part, $\hat{V}(t)$, for the radiation-matter interaction, which is assumed to be a perturbation of $\hat{H}_0$:

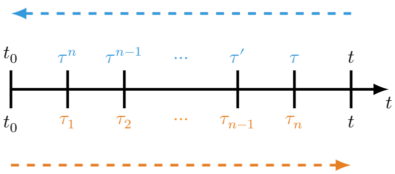

Figure 3.1: Time ordering for time-evolution operator. The figure graphically visualize the variable change in the expression of the time-evolution operator from eq. 3.8 to eq. 3.9.
.

$$\hat{H}(t) = \hat{H}_0 + \hat{V}(t) \quad (3.10)$$

For this scenario, shifting to the interaction picture (also known as the Dirac picture), in which the time dependency is present in both the observable and wavefunction, is advantageous. The wavefunction in the interaction picture, $|\Psi_I(t)\rangle$, is defined in relation to the Schrödinger picture wavefunction, $|\Psi_S(t)\rangle$, as:

$$|\Psi_S(t)\rangle = e^{-\frac{i}{\hbar}\hat{H}_0(t-t_0)}|\Psi_I(t)\rangle = \hat{u}_0(t, t_0)|\Psi_I(t)\rangle \quad (3.11)$$

for which the time-evolution operator is defined as:

$$\hat{u}_0(t, t_0) \overset{\text{def}}{\equiv} e^{-\frac{i}{\hbar}\hat{H}_0(t-t_0)} \quad (3.12)$$

In the Schrödinger picture, the full time evolution of the system includes contributions from both the unperturbed Hamiltonian $\hat{H}_0$ and the time-dependent perturbation $\hat{V}(t)$. In contrast, the interaction picture allows these two types of time dependence to be separated. Specifically, the time dependence of the state vector $|\Psi_I(t)\rangle$ reflects the evolution due to the perturbation $\hat{V}(t)$, while the evolution associated with the stationary background dynamics governed by $\hat{H}_0$ is encapsulated in $\hat{u}_0(t, t_0)$. Therefore, the Schrödinger equation can be expressed in the interaction picture using the definition in eq. 3.11:

$$\frac{\partial \Psi_I(t)}{\partial t} = -\frac{i}{\hbar}\hat{V}_I(t)\Psi_I(t) \tag{3.13}$$

where

$$\hat{V}_I(t) = \hat{u}_0^{\dagger}(t, t_0)\hat{V}(t)\hat{u}_0(t, t_0) \tag{3.14}$$

with the $\hat{u}_0^{\dagger}(t, t_0)$ indicates the Hermitian conjugate of the time-evolution operator. This formulation highlights that solving eq. 3.14 allows us to isolate and study only the dynamics driven by the perturbation $\hat{V}_I(t)$. As such, the interaction picture is particularly well suited for perturbative treatments, as it cleanly separates the effect of the perturbation from the background evolution. However, this wavefunction-based approach has its limits: the time-evolution operator acts on a single, specific wavefunction $\Psi(t_0)$, making it suitable for describing either a single molecule or an ensemble of identical molecules all prepared in the exact same initial state. To describe a general statistical ensemble in which different molecules may be in different initial states $\Psi(t_0)$, the powerful framework of the density matrix formalism is introduced, which enables a complete and consistent treatment of mixed quantum states.

3.3 Density matrix

For a system comprising a statistical collection of molecules, like a sample in a solution, a single wavefunction is not enough for a complete description. The density matrix formalism is necessary to handle systems in mixed states, which have a statistical distribution of quantum states due to interactions with a thermal environment.[23,24] For a pure quantum state, $|\Psi(t)\rangle$, the density operator is given by:

$$\hat{\rho}(t) \overset{\text{def}}{\equiv} |\Psi(t)\rangle\langle\Psi(t)| \tag{3.15}$$

A mixed state, however, is represented as a statistical average over a set of states $|\Psi_n\rangle$, each with a corresponding probability p_n:

$$\hat{\rho}(t) \overset{\text{def}}{\equiv} \sum_n p_n |\Psi_n(t)\rangle\langle\Psi_n(t)| \tag{3.16}$$

The elements on the diagonal of the density matrix, $\rho_{nn} = \langle n|\hat{\rho}|n\rangle$, correspond to the populations of the energy eigenstates $|n\rangle$, which is the probability of finding the system in that specific state. The off-diagonal elements, $\rho_{nm} = \langle n|\hat{\rho}|m\rangle$ where $n \neq m$, are known as coherences, that determine the coherent superpositions between the states $|n\rangle$ and $|m\rangle$.

These coherences oscillate at a frequency equal to the energy gap, $\omega_{nm} = (E_n - E_m)/\hbar$, and decay over time due to environmental interactions.[24,25]
But what is the advantage of using this formalism? In quantum mechanics, calculating an observable usually involves averaging over all possible states. When using wavefunctions, this often requires integrating over continuous variables, which can be mathematically and numerically challenging. However, the density matrix formalism naturally lends itself to situations where the quantum system can be described in a discrete basis. In those cases, observables are calculated as traces or matrix products,[26,27] which reduce to sums which simplifies both the conceptual understanding and the practical computation:

$$\langle \hat{A} \rangle = \langle \Psi | \hat{A} | \Psi \rangle = \mathrm{Tr}\left[\hat{A} \cdot \hat{\rho}\right] \tag{3.17}$$

Therefore, just as the wavefunction can describe the time evolution of a quantum system, the density matrix offers an equivalent framework for capturing this evolution, applicable even for complicated system. By considering a system represented by a pure state for sake of simplicity, the time evolution of the density matrix is expressed by the Liouville-Von Neumann equation adopting the interaction picture:

$$\frac{\partial \rho_I(t)}{\partial t} = -\frac{i}{\hbar}\left[\hat{H}_I(t), \rho_I(t)\right] \tag{3.18}$$

where

$$\rho_I(t) = \hat{u}_0^{\dagger}(t, t_0)\hat{\rho}(t)\hat{u}_0(t, t_0) \tag{3.19}$$

Analogously to eq. 3.7, the perturbative expansion of eq. 3.18 is:

$$\begin{aligned}
\hat{\rho}_I(t) = \hat{\rho}_I(t_0) &- \frac{i}{\hbar}\int_{t_0}^{t} dt_1 \left[\hat{V}_I(t_1), \hat{\rho}_I(t_0)\right] \\
&+ \left(-\frac{i}{\hbar}\right)^2 \int_{t_0}^{t} dt_2 \int_{t_0}^{t_2} dt_1 \left[\hat{V}_I(t_2), \left[\hat{V}_I(t_1), \hat{\rho}_I(t_0)\right]\right] + \dots \\
&+ \left(-\frac{i}{\hbar}\right)^n \int_{t_0}^{t} dt_n \int_{t_0}^{t_n} dt_{n-1} \dots \\
&\dots \int_{t_0}^{t_2} dt_1 \left[\hat{V}_I(t_n), \left[\hat{V}_I(t_{n-1}), \left[\dots, \left[\hat{V}_I(t_1), \hat{\rho}_I(t_0)\right] \dots\right]\right]\right]
\end{aligned} \tag{3.20}$$

$$\hat{\rho}_I(t) = \hat{\rho}_I^{(0)} + \hat{\rho}_I^{(1)} + \hat{\rho}_I^{(2)} \dots + \hat{\rho}_I^{(n)} \tag{3.21}$$

Here, $\hat{\rho}_I^{(n)}$ denotes the n^{th}-order term in the expansion of the density matrix, which is directly proportional to the observed polarization signal in n^{th}-order nonlinear spectroscopy where each perturbation $\hat{V}_I(t)$ can be associated to a interaction of the laser pulse with the system under investigation.

3.4 Response function

Response function theory provides a way to relate measured signals to the intrinsic optical properties of a system. It links the macroscopic response of a material to external perturbations, such as electromagnetic fields, with its microscopic quantum-mechanical description given by the density matrix.[24,28] In practice, this theory connects experimental observables to the underlying quantum dynamics, including state transitions, coherence, and population changes. The spectroscopic methods implemented in this thesis fall into two distinct categories based on the nature of the detected signal. The difference between them has profound theoretical consequences, as the form of the response function used to model the experiment changes depending on the nature of the signal, which is related to the macroscopic observable expressed in eq. 3.17. For coherent techniques, the observable is the macroscopic polarization induced in the sample, which radiates the signal field. In TA and C-2DES, the spectroscopic signal is related to the third-order polarization. For incoherent techniques, the observable is a direct measure of the population within a specific quantum state, often detected via a secondary process like fluorescence or photocurrent. For A-2DES experiments, the signal is associated instead to the fourth-order excited population, reflecting a different order of light-matter interaction.

Coherent detection

For coherent spectroscopic methods, such as TA and C-2DES, the fundamental observable is the macroscopic polarization. This polarization is generated within the sample by the applied pulse sequence and gives rise to the measured signal. Macroscopically, polarization arises from the collective behavior of many microscopic dipoles in the material and is defined as the average dipole moment per unit volume, consistent with Eq. 3.17. Since each microscopic dipole corresponds to the dipole moment of an individual quantum system, the macroscopic polarization $P(t)$ can be expressed as the expectation value of the dipole moment operator $\hat{\mu}(t)$ per unit volume:

$$P(t) = \langle \Psi(t)|\hat{\mu}(t)|\Psi(t)\rangle = \sum_{k=0}^{m} \mathrm{Tr}\left\{\hat{\mu}_I(t)\hat{\rho}_I^{(k)}(t)\right\} \tag{3.22}$$

For the third-order polarization, $P^{(3)}(t)$, the solution is derived by plugging eq. 3.20 into eq. 3.22:

$$\begin{aligned} P^{(3)}(t) = &\int_0^\infty d\tau_3 \int_0^\infty d\tau_2 \int_0^\infty d\tau_1 R^{(3)}(\tau_1, \tau_2, \tau_3) \\ &\cdot E_3(t-\tau_3)E_2(t-\tau_3-\tau_2)E_1(t-\tau_3-\tau_2-\tau_1) \end{aligned} \tag{3.23}$$

where the perturbation $\hat{V}_I(t)$ from eq. 3.20 is expressed under the dipole approximation:

$$\hat{V}_I(t) = -\hat{\mu}_I(t)E(t) \tag{3.24}$$

and the response function $R^{(3)}(\tau_1, \tau_2, \tau_3)$ is given by:

$$R^{(3)}(\tau_1, \tau_2, \tau_3) = \left(-\frac{i}{\hbar}\right)^3 \mathrm{Tr}\left\{\mu \cdot \left[\mu_3, \left[\mu_2, \left[\mu_1, \rho_{eq}\right]\right]\right]\right\} \tag{3.25}$$

with ρ_{eq} representing the unperturbed system before any interaction and where the operator had been rewritten for simplicity as:

$$\begin{aligned}
\mu_1 &= \hat{\mu}_I(0) \\
\mu_2 &= \hat{\mu}_I(\tau_1) \\
\mu_3 &= \hat{\mu}_I(\tau_1 + \tau_2) \\
\mu &= \hat{\mu}_I(\tau_1 + \tau_2 + \tau_3)
\end{aligned}$$

The response function $R^{(3)}(\tau_1, \tau_2, \tau_3)$ encapsulates all the information regarding the material's quantum dynamics and is mathematically represented by the expectation value of nested commutators involving the dipole operator.[24,25] Therefore, changes in the macroscopic polarizations are induced by three successive interactions with electric fields E_1, E_2, and E_3 occurring at times t_1, t_2, and t_3. Here, the time delays between interactions are defined as $\tau_1 = t_2 - t_1$ (coherence time), $\tau_2 = t_3 - t_2$ (population time), and $\tau_3 = t - t_3$ (coherence time). In this expression, ρ_{eq} represents the density matrix of the system at thermal equilibrium before any interactions occur.

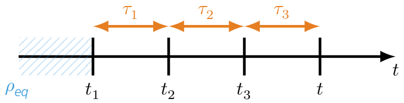

Figure 3.2: Time ordering and variables of the third-order response function. In this figure, the time variables defined to describe the response function are visualized. The t_i times represent the time interaction of the light-matter interaction, while the τ_i determine the time difference between them.

It is important to recognize that only the initial interactions with light, which drive the system out of equilibrium, are mathematically described by commutators. These first 3 interactions, occurring at t_1, t_2, and t_3, sequentially modify the system's density matrix, $\rho^{(3)}$ through a chain of quantum commutators. Each step in this preparation sequence must follow the previous one, meaning the time intervals between them are always positive, which ensures causality. The final step, however, plays a completely different role since it is not another commutator that further alters the state. Instead, it's the process where the previously generated coherences create a macroscopic polarization. This polarization then radiates the light field that is ultimately measured as the signal. In this way, the mathematical separation between the first 3 interactions and the last reflects a physical division between the preparation of quantum coherences and their subsequent emission as light which effectively probe the system.

Incoherent detection

For incoherent spectroscopic methods, such as A-2DES, the fundamental observable is the population of a specific quantum state, not a coherently emitted field. This population change is generated within the sample by the applied pulse sequence and is measured via a secondary process, such as fluorescence or photocurrent. Macroscopically, this signal corresponds to the number of quantum systems (e.g., molecules) that have transitioned into a final population state $|n\rangle$. Therefore, in this situation, the macroscopic signal $S(t)$ can be expressed as the expectation value of the operator $\hat{S}$:

$$S(t) = \langle\Psi(t)|\hat{S}(t)|\Psi(t)\rangle = \sum_{k=0}^{m} \mathrm{Tr}\left\{\hat{S}_I(t)\hat{\rho}_I^{(k)}(t)\right\} \tag{3.26}$$

The operator can be defined as:

$$\hat{S} = \sum_{n} \Gamma_n |n\rangle\langle n| \tag{3.27}$$

acting as a projector onto the full excited-state manifold, where each state n is weighted by a factor Γ_n.[27,29,30] In fluorescence-detected experiments Γ_n corresponds to the state's radiative quantum yield,[30–32] whereas in photocurrent-detected measurements it represents the state's internal quantum efficiency related to the charge-separation process.[33–35]
For a fourth-order population signal, $S^{(4)}(t)$, the solution is derived by considering the fourth-order term of the density matrix, $\rho^{(4)}(t)$. The signal is directly proportional to the response function which is, analogously to eq. 3.25, given by:

$$\begin{aligned} S^{(4)}(t) = \int_0^{\infty} d\tau_3 \int_0^{\infty} d\tau_2 \int_0^{\infty} d\tau_1 R^{(4)}(\tau_1, \tau_2, \tau_3, \tau_4) E_4(t) \\ \cdot E_3(t - \tau_4 - \tau_3) E_2(t - \tau_4 - \tau_3 - \tau_2) E_1(t - \tau_4 - \tau_3 - \tau_2 - \tau_1) \end{aligned} \tag{3.28}$$

where:

$$R^{(4)}(\tau_1, \tau_2, \tau_3, t) = \left(-\frac{i}{\hbar}\right)^4 \mathrm{Tr}\left\{S \cdot \left[\mu_4, \left[\mu_3, \left[\mu_2, \left[\mu_1, \rho_{eq}\right]\right]\right]\right]\right\} \tag{3.29}$$

with ρ_{eq} representing the unperturbed system before any interaction and where the operator had been rewritten for simplicity as:

$$\begin{aligned} \mu_1 &= \hat{\mu}_I(0) \\ \mu_2 &= \hat{\mu}_I(\tau_1) \\ \mu_3 &= \hat{\mu}_I(\tau_1 + \tau_2) \\ \mu_4 &= \hat{\mu}_I(\tau_1 + \tau_2 + \tau_3) \\ S &= \hat{S}_I(\tau_1 + \tau_2 + \tau_3 + t) \end{aligned}$$

The temporal delays between interactions are defined exactly as in the coherent case It is essential to recognize that for incoherent detection, all four dipole operators, which represent the system's interactions with the individual electric fields, are located within the nested commutators and serve to prepare the quantum state. In fact, unlike in coherent detection, the final interaction does not induce a polarization that radiates a signal. Instead, the fourth interaction plays the role of converting the system from a coherence into the final population state that is directly measured after a time t from the fourth interaction with the field.

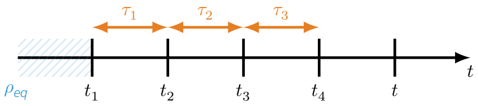

Figure 3.3: Time ordering and variables of the fourth-order response function. In this figure, the time variables defined to describe the response function are visualized. The t_i times represent the time interaction of the light-matter interaction, while the τ_i determine the time difference between them.

3.5 Feynman diagrams

The explicit solution of eq. 3.23 and eq. 3.28 contains many terms, arising from the number of electric-field interactions and from the explicit expansion of the commutators within the corresponding response functions. When performing an experiment involving n distinct incident electric fields, each of these can be expressed as the sum of individual complex fields, including their complex conjugates, even if it is usually described as a real quantity for convenience:

$$\begin{aligned} E_{\text{tot}}(\vec{r}, t) &= \sum_{j=1}^{n} E_j(\vec{r}, t) + E_j^*(\vec{r}, t) \\ &= \sum_{j=1}^{n} |A_j(t)| \left(e^{+i(\vec{k}_j\vec{r} - \omega_j t + \varphi_j)} + e^{-i(\vec{k}_j\vec{r} - \omega_j t + \varphi_j)} \right) \end{aligned} \tag{3.30}$$

which is defined using the formalism developed in the previous chapter, explicitly accounting for propagation direction via the wavevectors k, and considering a transform-limited pulses by neglecting any time-dependent phase. Therefore, each interaction would lead to $(2n)^n$ terms. However, if we adopt the following assumptions, the number of terms arising from the electric field reduces to 1:[25]

- **Time ordering.** The interpulse delays are much longer than the individual pulse durations, avoiding pulse overlap in time. This approximation reduces the total number of terms down to 2^n.
- **Rotating wave approximation.** When the system is in resonance with the specific transition, the rapidly oscillating terms average to zero on integration and can be neglected. Therefore only one of the rotating component of the electric field survives, reducing the number of terms to $1^n = 1$.
- **Semi-impulsive limit.** In addition, if the pulse duration is short compared to the timescale porcesses of the system but longer than the optical period, the pulse envelope can be approximated to a δ function.

Consequently, eq. 3.23 and eq. 3.28 simplify to their response functions.
Eq. 3.25 and eq. 3.29 can be written more explicitly by expanding the respective commutators and letting the dipole operators acting on the ket or bra side of the density matrix. Practically, the perturbation's role in driving population transfers and coherence evolutions becomes transparent, as each dipole operator clearly defines how the system "moves" through different density matrix elements. For the coherent detection case, the third-order response function involves three dipole interaction factors, which give rise to $2^3 = 8$ distinct terms, each one defining a different Liouville pathway. For the incoherent detection case, the fourth-order response function involves an extra dipole interaction factors, which gives rise to $2^4 = 16$ distinct Liouville pathways. More generally, the n^{th}-order response function admits a far more concise grouping when expressed as:

$$R^{(n)}(\tau_1, \ldots, \tau_n) = \left(-\frac{i}{\hbar}\right)^n \sum_{\alpha=1}^{n} \left[R_\alpha(\tau_1, \ldots, \tau_n) + R^*_\alpha(\tau_1, \ldots, \tau_n)\right] \tag{3.31}$$

where the $*$ symobl defines the complex conjugate component. It is possible to write each contribution explictly for the third-order:

$$\begin{aligned} R_1 &= \mathrm{Tr}\left[\mu\rho_{eq}\mu_1\mu_2\mu_3\right] & R_1^* &= \mathrm{Tr}\left[\mu\mu_3\mu_2\mu_1\rho_{eq}\right] \\ R_2 &= \mathrm{Tr}\left[\mu\mu_1\rho_{eq}\mu_2\mu_3\right] & R_2^* &= \mathrm{Tr}\left[\mu\mu_3\mu_2\rho_{eq}\mu_1\right] \\ R_3 &= \mathrm{Tr}\left[\mu\mu_2\rho_{eq}\mu_1\mu_3\right] & R_3^* &= \mathrm{Tr}\left[\mu\mu_3\mu_1\rho_{eq}\mu_2\right] \\ R_4 &= \mathrm{Tr}\left[\mu\mu_3\rho_{eq}\mu_1\mu_2\right] & R_4^* &= \mathrm{Tr}\left[\mu\mu_2\mu_1\rho_{eq}\mu_3\right] \end{aligned}$$

and for the for fourth-order:

$$\begin{aligned}
R_1 &= \mathrm{Tr}\left[S\rho_{eq}\mu_1\mu_2\mu_3\mu_4\right] & R_1^* &= \mathrm{Tr}\left[S\mu_4\mu_3\mu_2\mu_1\rho_{eq}\right] \\
R_2 &= \mathrm{Tr}\left[S\mu_1\rho_{eq}\mu_2\mu_3\mu_4\right] & R_2^* &= \mathrm{Tr}\left[S\mu_4\mu_3\mu_2\rho_{eq}\mu_1\right] \\
R_3 &= \mathrm{Tr}\left[S\mu_2\rho_{eq}\mu_1\mu_3\mu_4\right] & R_3^* &= \mathrm{Tr}\left[S\mu_4\mu_3\mu_1\rho_{eq}\mu_2\right] \\
R_4 &= \mathrm{Tr}\left[S\mu_3\rho_{eq}\mu_1\mu_2\mu_4\right] & R_4^* &= \mathrm{Tr}\left[S\mu_4\mu_2\mu_1\rho_{eq}\mu_3\right] \\
R_5 &= \mathrm{Tr}\left[S\mu_4\rho_{eq}\mu_1\mu_2\mu_3\right] & R_5^* &= \mathrm{Tr}\left[S\mu_3\mu_2\mu_1\rho_{eq}\mu_4\right] \\
R_6 &= \mathrm{Tr}\left[S\mu_2\mu_1\rho_{eq}\mu_3\mu_4\right] & R_6^* &= \mathrm{Tr}\left[S\mu_4\mu_3\rho_{eq}\mu_1\mu_2\right] \\
R_7 &= \mathrm{Tr}\left[S\mu_3\mu_1\rho_{eq}\mu_2\mu_4\right] & R_7^* &= \mathrm{Tr}\left[S\mu_4\mu_2\rho_{eq}\mu_1\mu_3\right] \\
R_8 &= \mathrm{Tr}\left[S\mu_4\mu_1\rho_{eq}\mu_2\mu_3\right] & R_8^* &= \mathrm{Tr}\left[S\mu_3\mu_2\rho_{eq}\mu_1\mu_4\right]
\end{aligned}$$

At a first impact, the physical significance of these expressions can be elusive. Therefore, it is convenient to introduce the Feynman diagrams, a pictorial and intuitive way to visualize the Liouville pathways.[32,36,37] The following rules are essential to correctly interpret and understand the diagrams:

- **Axes and sides.** Vertical lines track the time evolution of the density matrix: the left line is the *ket*, the right line is the *bra*. Time flows upward.

- **Interactions.** Each interaction with an electric field is drawn as an arrow hitting one of the lines. For coherently detected signals (e.g., third-order spectroscopy), the emitted field arising after the final interaction, is typically drawn as a wavy arrow leaving the density matrix. For incoherently detected signals, since the system ends in a population state after the last field interaction, the incoherent signal is shown as a pair of arrows exiting the diagram simultaneously, one from the *ket* side and one from the *bra* side.

- **Sign convention** A field $E(\vec{r}, t) \propto e^{+i(\vec{k_j}\vec{r}-\omega t+\varphi)}$ is drawn with a right-pointing arrow; a field $E^*(\vec{r}, t) \propto e^{-i(\vec{k_j}\vec{r}-\omega t+\varphi)}$ with a left-pointing arrow. Arrows pointing toward the system denote absorption; arrows pointing away denote emission or de-excitation. The sign of the resulting signal associated to a Feynman diagram is $(-1)^{n_{bra}}$, where n_{bra} defines the number of interactions on the *bra* side.

- **Initial and final states.** Before the first interaction the system is in equilibrium (typically the ground state). After the last interaction it is in a population state (ground or excited).

It is possible to draw the Feynman diagrams for the third- and fourth-order response function from eq. 3.30, as visualized in fig.. 3.4. The Feynman diagrams sketched in Fig. 3.4

offer a visualization of the system's quantum evolution under a sequence of light-matter interactions, as described by a perturbative expansion of the density matrix. They represent all the possible way in which the electric field can interact with the density matrix, for the respective order. However, for n-levels system, with $n > 2$, the total amount of possible Feynman diagrams will increase greatly with the number of levels. In the figure, Feynman diagrams labeled with letter *a* and *b* take in account evolution of the density matrix to a first and second excited state, respectively. The reason is that for the same Feynman diagram, multiple density matrix evolution become possible due to the increased amount of excited states. The order of the response function determines the nature of the final quantum state, which in turn dictates the physical observable and the experimental detection scheme. The third-order nonlinear response, characterized by response functions $R^{(3)}$, arises from three sequential interactions with an applied electric field. As depicted in the diagrams, the system evolves from an initial equilibrium population (a diagonal density matrix element, ρ_{gg}) through various intermediate states after each field interaction. The critical outcome of the third interaction brings the system in a coherence state, defined by an off-diagonal element of the density matrix. This polarization acts as a source term in Maxwell's equations, radiating a new signal field due to constructive interference of the fields radiated by individual molecules. On the other hand, the fourth-order response, which involves four light-matter interactions, projects the system from a coherence back into a population state after the last field interaction, which is represented by a diagonal density matrix element such as ρ_{ee}. A population state does not possess an oscillating dipole moment and therefore cannot radiate a coherent field. The signal, in this case, is the measurement of the population itself, such as fluorescence or photocurrent from the excited population state. It has to be noticed that if, after the fourth interaction, the system ends in the ground-state population ρ_{gg}, the incoherent signal cannot be generated. Assuming identical pulses for all the Feynman diagrams of a given order, the light–matter interaction is identical in sequence and strength: the system undergoes one field interaction per pulse, each with the same pulse energy. Consequently, the distinguishing feature among pathways is set by the phase-matching condition imposed by the argument of the complex exponential of the electric field. Generally, for third-order techniques such as C-2DES, only Feynman diagrams with coherently emitted field from ket side are considered.

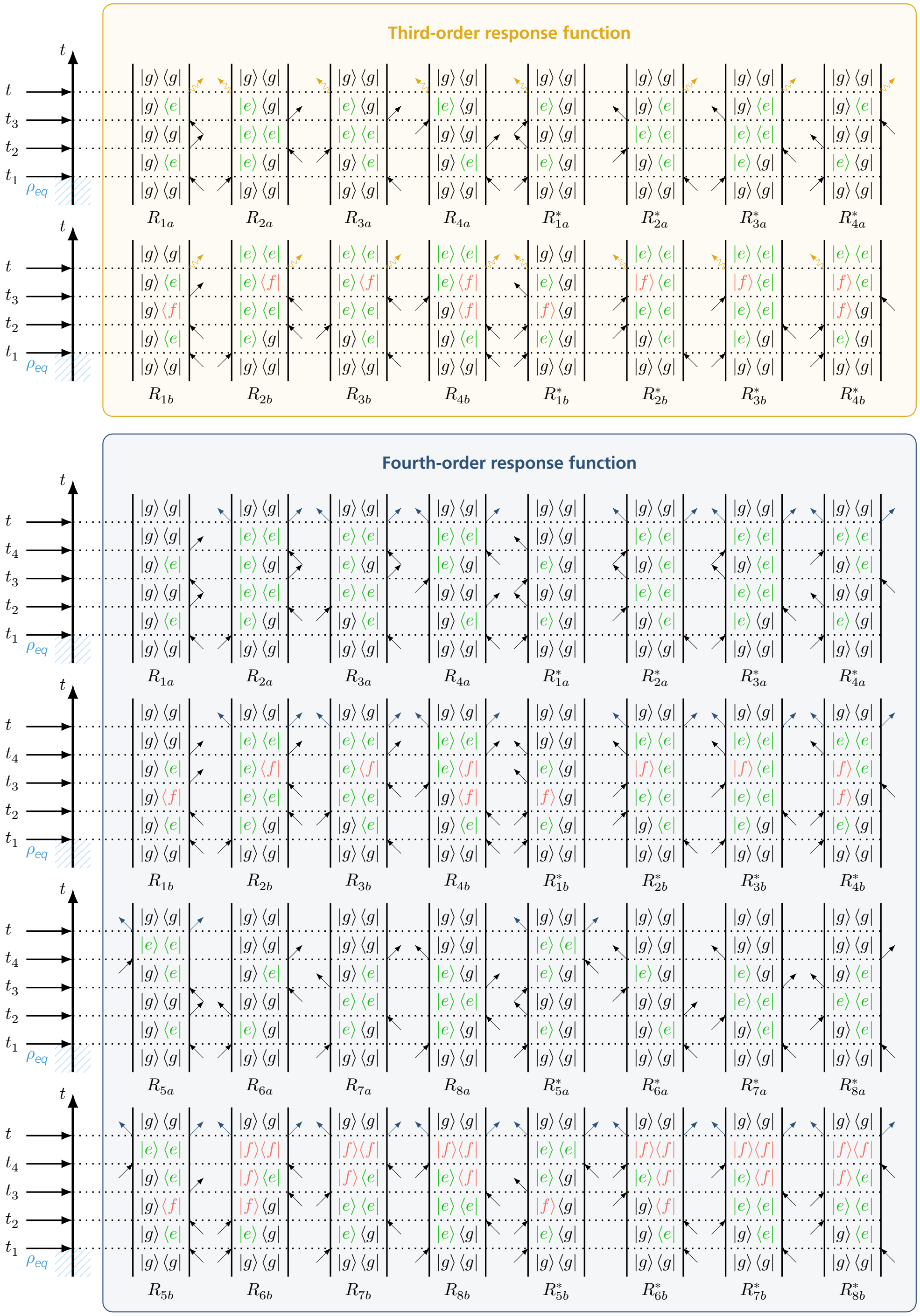

Figure 3.4: Feynman diagrams of third- and fourth-order response function. This figure represents all the possible Feynman diagrams for a third-order (yellow box) and fourth-order (blue box) response function in a three-levels system, respectively.

3.6 Phase-matching

The Feynman diagrams describe how light sculpts the state of a material, with the system ending into a state which determines the nature of the spectroscopic signal we can detect. In both the third- and fourth-order nonlinear optical signal, the first two interactions often set a similar scene during the time interval t_2, preparing the system in either a population or, for a multilevel system, a quantum coherence. But the story dramatically diverges after the final interaction.

Coherent detection

For the third-order response function, the last interaction leaves the system in a coherent state, with it's macroscopic polarization that acts as a source, radiating a new, coherent signal field. But where is this signal emitted? It doesn't just radiate with a random orientation. For any third-order Liouville pathway, represented with the respective Feynman diagram in fig. 3.4, the contribution to the final coherent state can be described by rewriting eq.3.23 as:

$$\begin{aligned} P^{(3)}(t) = \sum_{\alpha,\beta,\gamma} \Bigg[\int_0^\infty d\tau_3 \int_0^\infty d\tau_2 \int_0^\infty d\tau_1 E_3 E_2 E_1 \\ \cdot R^{(3)}(\tau_1, \tau_2, \tau_3, \alpha, \beta, \gamma) e^{i(\alpha\vec{k}_1 + \beta\vec{k}_2 + \gamma\vec{k}_3)} \Bigg] \end{aligned} \tag{3.32}$$

where the vector nature of the electric field is shown explicitly, the temporal dependence of the electric fields are omitted for convenience, and the α, β, and γ parameters are introduced. These new parameters define how each individual electric field interacts with the system or, more precisely, how they act on the density matrix. All admissible triples (α, β, γ) follow from a few simple constraints.[38] First of all, for a third-order response generated by three distinct fields, higher-orders can be ignored. The sum of the absolute value of the parameters must be minor or equal to three. Moreover, since that after the last interaction the system is found in a coherent state, this means that the number of interactions on the *ket* and on the *bra* side of the density matrix is odd.

$$\begin{cases} |\alpha| + |\beta| + |\gamma| \leq 3 \\ \alpha + \beta + \gamma = \pm 1 \end{cases} \quad \text{with} \quad \alpha, \beta, \gamma \neq 0 \tag{3.33}$$

These solutions comprise three distinct phase-matching directions and their sign-reversed counterparts. Since these counterparts are merely mirror images offering no independent nor additional information, we can restrict the analysis to the three unique directions

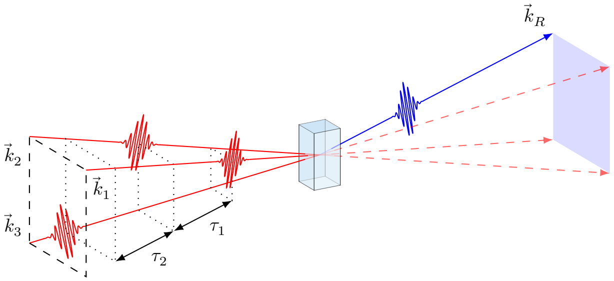

Figure 3.5: Phase matching condition in C-2DES for repahsing signal. Three laser pulses interact with the sample, generating a nonlinear signal in the phase matching direction. The controlled delays τ_1 (coherence), τ_2 (population/waiting) are scanned to build a sequence of 2D maps.

without any loss. These three directions correspond to the conventional signal groupings based on their phase-matching geometries: Rephasing (R), Non-Rephasing (NR), and Double Quantum (2Q):

$$\begin{aligned} \vec{k}_R &= -\vec{k}_1 + \vec{k}_2 + \vec{k}_3 \\ \vec{k}_{NR} &= +\vec{k}_1 - \vec{k}_2 + \vec{k}_3 \\ \vec{k}_{2Q} &= +\vec{k}_1 + \vec{k}_2 - \vec{k}_3 \end{aligned} \tag{3.34}$$

Detecting along $\vec{k}_{\mathrm{R}}$, $\vec{k}_{\mathrm{NR}}$, or $\vec{k}_{\mathrm{2Q}}$ isolates the corresponding phase-matched signals, each forming coherent sums over multiple diagrams. Accordingly, the diagrams in fig. 3.4 are grouped by phase-matching direction: R: R^*_{2b}, R_{3a}, R_{4a}; NR: R^*_{1a}, R_{2a}, R^*_{3b}; 2Q: R^*_{1b}, R^*_{4b}.

Incoherent detection

For the fourth-order response function, the last interaction pushes the system beyond coherence into a population state. A population cannot emit a coherent field. Since directional phase-matching through wavevectors is not possible, the operation is transferred to the phases of the electric fields themselves.[39] Similarly to the case for coherent phase-matching, eq. 3.28 can be rewritten as:

$$\begin{aligned} S^{(4)}(t) = \sum_{\alpha,\beta,\gamma,\delta} \Bigg[\int_0^\infty d\tau_3 \int_0^\infty d\tau_2 \int_0^\infty d\tau_1 E_4 E_3 E_2 E_1 \\ \cdot R^{(4)}(\tau_1, \tau_2, \tau_3, t, \alpha, \beta, \gamma, \delta) e^{i(\alpha\varphi_1 + \beta\varphi_2 + \gamma\varphi_3 + \delta\varphi_4)} \Bigg] \end{aligned} \tag{3.35}$$

where the phase of each electric field is shown explicitly, the temporal dependence of the electric fields are omitted for convenience, and the α, β, γ, and δ parameters are introduced. Also in this case, all admissible quadruplets $(\alpha, \beta, \gamma, \delta)$ follow from a few simple

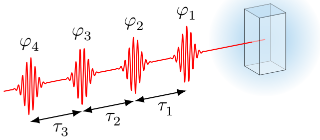

Figure 3.6: Pulse sequence for incoherent detected 2D spectroscopy. Four laser pulses interact with the sample, generating a nonlinear signal that can be recorded as a population related observable, such as fluorescence or photocurrent. The signal is retrieved based on the phase relation between the laser pulses. The controlled delays τ_1 and τ_3 (coherence), τ_2 (population) are scanned to build a sequence of 2D maps.

constraints. First of all, for a fourth-order response generated by four distinct fields, higher-orders contributions are ignored. The sum of the absolute value of the parameters must be minor or equal to four. Moreover, since that after the last interaction the system is found in a population state, this means that the number of interactions on the *ket* and on the *bra* side of the density matrix must be even.

$$\begin{cases} |\alpha| + |\beta| + |\gamma| + |\delta| \leq 4 \\ \alpha \ + \ \beta \ + \ \gamma \ + \ \delta \ = 0 \end{cases} \quad \text{with} \quad \alpha, \beta, \gamma, \delta \neq 0 \tag{3.36}$$

Similarly to coherent phase-matching, the solutions comprise three distinct phase-matching values and their sign-reversed counterparts. These three phase combinations correspond to the same conventional signal groupings in the coherent phase-matching geometries:

$$\begin{aligned} \varphi_{\mathrm{R}} &= -\varphi_1 + \varphi_2 + \varphi_3 - \varphi_4 \\ \varphi_{\mathrm{NR}} &= +\varphi_1 - \varphi_2 + \varphi_3 - \varphi_4 \\ \varphi_{2\mathrm{Q}} &= +\varphi_1 + \varphi_2 - \varphi_3 - \varphi_4 \end{aligned} \tag{3.37}$$

analogously to directional phase-matching, the corresponding phase-matched signals are detected with specific phase φ_{R}, φ_{NR}, or $\varphi_{2\mathrm{Q}}$, each forming coherent sums over multiple diagrams.[40] Accordingly, the diagrams in fig. 3.4 are grouped by phase-matching over phase: R: R^*_{2b}, R_{3a}, R_{4a} and R^*_{8b}; NR: R_{2a}, R^*_{3b}, R^*_{5a} and R_{7b}; 2Q: R^*_{4b}, R^*_{5b} and R_{6b}. However, contrary to the coherent phase-matching which has the advantage of spatially separate the desired and undesired signals, in the incoherent detection of excited state population signal is a sum of all the possible directional component of the polarization. To detect specific Liouville pathways, a phase-cycling[39,41,42] or phase-modulation[43,44] scheme is required.

Phase cycling

Phase cycling is an elegant technique, borrowed from the field of Nuclear Magnetic Resonance (NMR),[45–48] that isolates a specific nonlinear signal by systematically manipulating the phase of each laser pulse in the excitation sequence. The core principle is that the phase of the final signal is a linear combination of the phases of the laser pulses that generate it, analogous to how wavevectors combine in phase-matching for coherent detection. During a phase cycling scheme, the unwanted signals destructively interfere and cancel out, while the desired signal constructively adds up.[49,50] By recalling the equality in 3.36, it is clear that α, β, γ and δ are not independent of one another. Therefore, it is possible to rewrite eq. 3.35 by referencing the phase of each pulse interaction to the phase of the first pulse:

$$\begin{aligned} S^{(4)}(t) = \sum_{\beta,\gamma,\delta} \Bigg[& \int_0^{\infty} d\tau_4 \int_0^{\infty} d\tau_3 \int_0^{\infty} d\tau_2 \int_0^{\infty} d\tau_1 E_4 E_3 E_2 E_1 \\ & \cdot R^{(4)}(\tau_1, \tau_2, \tau_3, \tau_4) e^{i(\beta\varphi_{21}+\gamma\varphi_{31}+\delta\varphi_{41})} \Bigg] \end{aligned} \tag{3.38}$$

where $\varphi_{k1} = \varphi_k - \varphi_1$, for each field interaction k. To isolate a specific nonlinear response pathway, characterized by a unique set of coefficients (β, γ and δ) corresponding to a phase-matching condition in eqs. 3.37, one must sample the finite phase space of each φ_{k1}. This is achieved by performing the multipulse experiment multiple times, systematically varying the interpulse phases in discrete steps. Mathematically, this selection process is equivalent to a discrete Fourier transform.[29,51] The desired response function is recovered by summing the signals measured at each phase step, each weighted by a complex exponential factor:

$$\begin{aligned} R^{(4)}(\tau_1, \tau_2, \tau_3, \tau_4) = & \frac{1}{LMN} \sum_{l=0}^{L-1} \sum_{m=0}^{M-1} \sum_{n=0}^{N-1} S^{(4)}(t, l\Delta\varphi_{21}, m\Delta\varphi_{31}, n\Delta\varphi_{41}) \\ & \cdot e^{-i\beta l\Delta\varphi_{21}} e^{-i\gamma m\Delta\varphi_{31}} e^{-i\delta n\Delta\varphi_{41}} \end{aligned} \tag{3.39}$$

The phase increments, $\Delta\varphi_{k1}$, are defined as:

$$\begin{aligned} \Delta\varphi_{21} &= \frac{2\pi}{L} \\ \Delta\varphi_{31} &= \frac{2\pi}{M} \\ \Delta\varphi_{41} &= \frac{2\pi}{N} \end{aligned}$$

where $L, M,$ and N are the number of phase steps for pulses 2, 3, and 4, respectively. Typically, the minimum number of phase cycling steps required to distinguish R and NR contributions in a four-pulse experiment (and avoiding aliasing)[52,53] is $1 \times 3 \times 3 \times 3 = 27$. Practically, this is done by systematically stepping the absolute phase φ_k of one interacting field while all other phases are held constant, and then repeating this procedure for the subsequent pulses. For a fixed population time, this routine generates 27 distinct 2D maps. The final, desired 2D map for a specific signal is obtained by linearly combining these 27 measured maps.[31,54,55] The coefficient, or weighting factor, for each map in this sum is the complex exponential term from the Fourier transform shown above.[56] The sign or, more generally, the complex phase of this weighting factor, is determined by Euler's relation:

$$e^{i\varphi} = \cos(\varphi) + i\sin(\varphi) \tag{3.40}$$

This relationship dictates how each measured map is added or subtracted to constructively build the desired signal while simultaneously canceling all others. By choosing different sets of coefficients (β, γ and δ), distinct nonlinear signals can be retrieved from the very same set of 27 experimental scans.

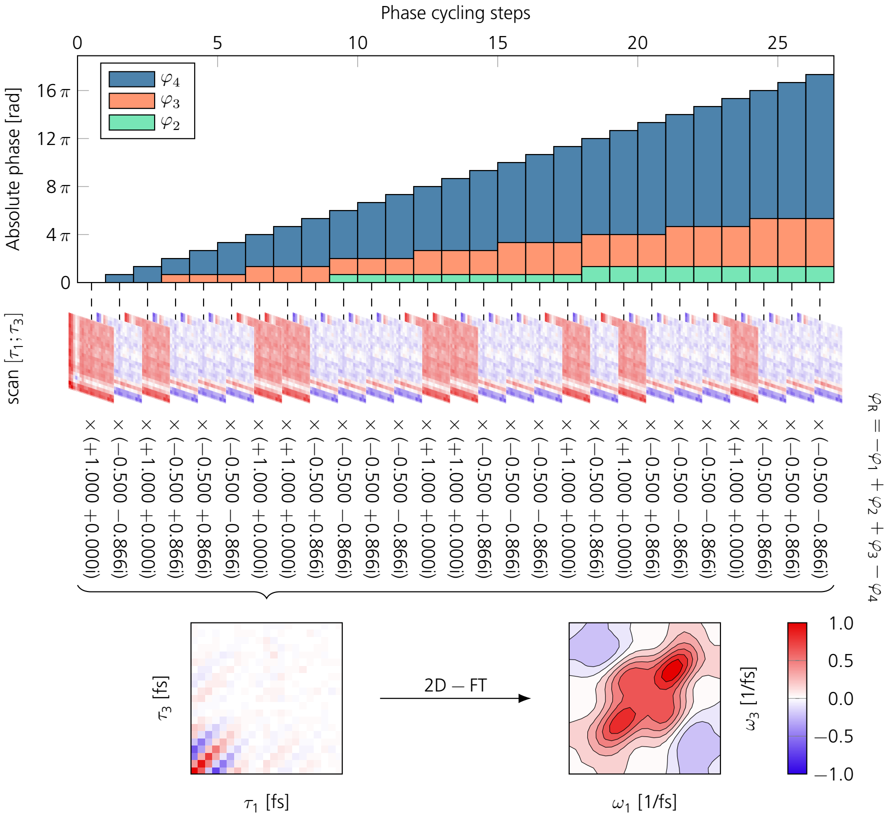

Figure 3.7: Phase cycling routine. For a fixed population time (τ_2), the absolute phases φ_1, φ_2, φ_3, and φ_4 of the four pulses are stepped over the phase-cycling index for each pixel of the time-domain 2D map. Scanning the full delay plane (τ_1, τ_3) yields $L \times M \times N$ 2D maps, one per phase-cycling step. Shown here is the reconstruction for a $1 \times 3 \times 3 \times 3 = 27$-step scheme. The rephasing time-domain 2D map is obtained by weighting the 27 maps according to the phase-matching condition $\varphi_\mathrm{R} = -\varphi_1 + \varphi_2 + \varphi_3 - \varphi_4$ and summing them. A subsequent 2D-FT produces the spectrum in the frequency domain (ω_1, ω_3).

Phase modulation

An alternative approach to phase cycling for isolating specific Liouville pathways is the phase modulation technique[43,44], also known as cogwheel phase cycling.[49,57] Phase modulation is a sophisticated technique for isolating signals that functions as a form of continuous phase cycling. Instead of varying pulse phases in discrete steps, this method shifts the carrier-envelope phase of each k^{th} pulse smoothly from one laser shot to the next by an increment of $\Omega_k T$, where Ω_k represents the modulation frequency for the k^{th} pulse and T is the time between shots, which is determined by the laser's repetition rate, $\Omega_{\text{rep}} = 1/T$.[58–60] The phase of the k^{th} pulse for the m^{th} shot, acquired at experimental time mT (where $T = \Omega_{\text{rep}}^{-1}$ is the laser repetition period), is defined as:

$$\varphi_k(mT) = \Omega_k mT + \varphi_{k,0} \tag{3.41}$$

Here, Ω_k is the modulation frequency applied to pulse k, and $\varphi_{k,0}$ is its initial phase at $m = 0$. By substituting this expression into the fourth-order signal equation (eq. 3.35), the phase-dependent term for a specific Liouville pathway becomes:

$$e^{i\left[\sum_{k=1}^{4} c_k \varphi_k(mT)\right]} = e^{\left[i\left(\sum_{k=1}^{4} c_k \Omega_k\right) mT\right]} \cdot e^{i\left[\sum_{k=1}^{4} c_k \varphi_{k,0}\right]} \tag{3.42}$$

where the coefficients (c_1, c_2, c_3, c_4) correspond to the phase-matching quadruplet $(\alpha, \beta, \gamma, \delta)$ for that pathway. The first term on the right-hand side of eq. 3.42 shows that the signal contribution from each pathway oscillates at a unique detection frequency, Ω_S, as a function of the experimental time mT. This detection frequency is a linear combination of the applied modulation frequencies, weighted by the phase-matching coefficients:

$$\Omega_S \equiv \sum_{k=1}^{4} c_k \Omega_k = \alpha\Omega_1 + \beta\Omega_2 + \gamma\Omega_3 + \delta\Omega_4 \tag{3.43}$$

Since each set of coefficients $(\alpha, \beta, \gamma, \delta)$ maps to a distinct Ω_S, different Liouville pathways are encoded onto different frequencies. The total measured signal, $S^{(4)}(t, mT)$, is a superposition of these oscillating components. Isolation of a desired pathway is achieved by performing a discrete Fourier transform on the sequence of signals acquired over many laser shots with respect to the time variable mT:

$$R^{(4)}(t, \Omega_S) = \sum_m S^{(4)}(t, mT) e^{-i\Omega_S mT} \tag{3.44}$$

This transform projects the time-domain data into the frequency domain, where the signal amplitude at a specific Ω_S corresponds to the isolated response of the targeted Liouville pathway. The detection frequencies for the R, NR, and 2Q coherence pathways are therefore determined by their respective phase-matching conditions from eqs. 3.37:

$$\begin{aligned} \Omega_R &= -\Omega_1 + \Omega_2 + \Omega_3 - \Omega_4 \\ \Omega_{NR} &= +\Omega_1 - \Omega_2 + \Omega_3 - \Omega_4 \\ \Omega_{2Q} &= +\Omega_1 + \Omega_2 - \Omega_3 - \Omega_4 \end{aligned} \tag{3.45}$$

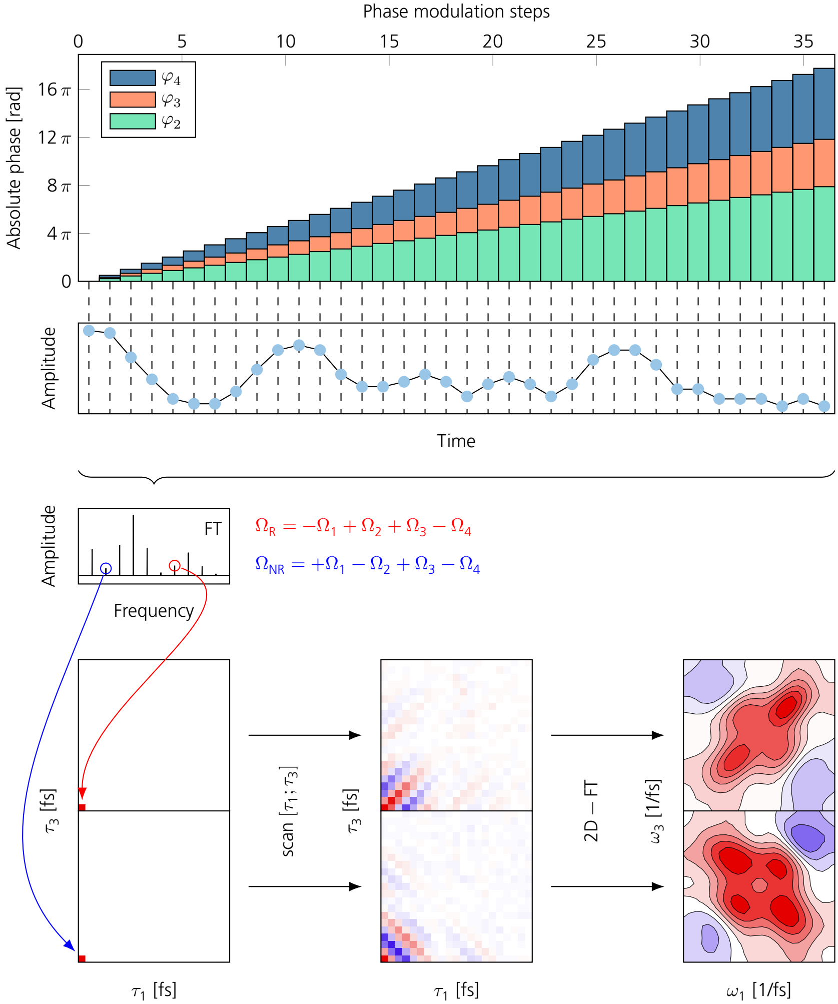

Figure 3.8: Phase modulation routine. For a fixed population time τ_2, the absolute phases $\varphi_1, \varphi_2, \varphi_3, \varphi_4$ of the four pulses are modulated with different modulation frequencies (Ω_1, Ω_2, Ω_3, and Ω_4) at each pixel (τ_1, τ_3) of the time–domain 2D map. For each pixel, the acquired signal is then FT, giving a spectrum in frequency domain with different peaks. By carefully choosing the phase matching condition, it is possible to retrieve the desired nonlinear signal. The R (NR) peak, circled in red (blue), can be found at the specific frequency $\Omega_R = -\Omega_1 + \Omega_2 + \Omega_3 - \Omega_4$ ($\Omega_{NR} = +\Omega_1 - \Omega_2 + \Omega_3 - \Omega_4$). The amplitude of the signal correspond to the amplitude of the pixel in the time-domain 2D map. Repeating the procedure for each pixel in the time-domain 2D map allows to construct the 2D map completely. A subsequent 2D-FT produces the spectrum in the frequency domain (ω_1, ω_3).

By selecting appropriate modulation frequencies Ω_k, these signals can be separated into distinct frequency channels, allowing for their simultaneous detection. Practically, a two-dimensional spectrum for a fixed population time, τ_2, is constructed by acquiring the signal point-by-point across the grid of coherence time delays, (τ_1, τ_3). At each specific (τ_1, τ_3) coordinate, the experimental signal is recorded over a sequence of many consecutive laser shots. During this acquisition, the CEP of each interacting pulse is modulated at a distinct, pre-defined frequency (Ω_k for the k^{th} pulse). This process encodes the system's response onto an oscillating signal, where the intensity varies as a function of the experimental acquisition time. To decode this information, the recorded signal is subjected to a Fourier transform. This mathematical procedure converts the time-domain signal into the frequency domain, where all contributing optical signals are cleanly separated. Each distinct physical process, such as the linear and nonlinear responses, appears as a peak at a specific detection frequency, Ω_S. This detection frequency is a unique linear combination of the individual modulation frequencies applied to the pulses. By isolating the signal component at the precise detection frequency corresponding to the desired Liouville pathway, such as the ones defined by eqs. 3.45 the pure response for that single pixel is extracted. This entire procedure is then repeated for every point in the (τ_1, τ_3) grid to assemble the complete 2D spectrum.

3.7 2D spectra

After a nonlinear multidimensional spectroscopic experiment, the measurement yields a 3D data set that can be visualized as a stack of time-domain 2D maps $S(\tau_1, \tau_3; \tau_2)$, one for each population time τ_2. To obtain the spectroscopic information in the frequency domain, a two-dimensional Fourier transform (2D-FT) is applied with respect to the coherence times τ_1 and τ_3 at each fixed τ_2, producing $S(\omega_1, \tau_2, \omega_3)$. These 2D spectra establish a correlation between the excitation frequencies (ω_1, shown on the horizontal axis) and the emission frequencies (ω_3, on the vertical axis).

The analysis of a 2D spectrum yields a wealth of information:

- **Diagonal Peaks:** Signals appearing along the diagonal line ($\omega_1 = \omega_3$) correspond to transitions where the system is excited and subsequently emits at the same frequency. The locations of these peaks identify the energies of the excitonic states, which correspond to a population state in the density matrix.
- **Cross-Peaks:** Off-diagonal signals ($\omega_1 \neq \omega_3$) serve as direct proof of coupling between different electronic states. This coupling can be due to energy transfer, chemical exchange, or coherent interactions. The emergence and evolution of these cross-peaks as a function of τ_2 allow for the mapping of these dynamic processes.

- **Lineshape:** The shape of the peaks reveals details about the system's interactions with its surroundings. The width of a peak along the diagonal is related to inhomogeneous broadening (for instance, from a size distribution in quantum dots), while the width along the anti-diagonal is related to homogeneous broadening (which includes lifetime and dephasing effects).
- **Dynamics:** The changes in peak amplitudes and positions as the population time τ_2 varies are used to track population relaxation and the transfer of energy. Oscillations in the amplitudes of the peaks as a function of τ_2, referred to as quantum beats, are a direct observation of evolving electronic or vibrational coherences. Analyzing these oscillations yields the frequencies of the coherences and their associated dephasing times.

The 2D spectrum is a complex quantity, containing both real and imaginary components. In most analyses, attention is directed to the real part, as it carries the dominant spectroscopic response. However, the real part represents a superposition of absorptive and dispersive contributions, which can complicate the assignment and interpretation of spectral features. To construct purely absorptive 2D spectra, one typically combines the rephasing and non-rephasing signals through summation. This procedure produces spectra with symmetric peak profiles that more directly reflect the underlying energy-level structure of the system, thereby providing a clearer basis for both qualitative interpretation and quantitative analysis. All spectral features observed in a two-dimensional map can be assigned to specific Liouville pathways. Consequently, each of the pathways illustrated in Fig. 3.4 corresponds to a distinct physical process. The principal contributing pathways are conventionally grouped into three categories:

- **Ground State Bleach (GSB):** The ground-state bleach pathway arises from the depletion of ground-state population by the pump, leading to a reduced probability of further absorption and thus a decrease in the measured absorbance. This will appear as a positive feature in a 2D map.
- **Stimulated Emission (SE):** The stimulated emission (SE) pathway reflects the process in which the pump prepares an excited-state population that can be driven to emit coherently, resulting in an enhanced emission signal. This will appear as a positive feature in a 2D map.
- **Excited-State Absorption (ESA):** The excited-state absorption (ESA) pathway occurs when the system, already promoted to the first excited state, is further excited by the probe into a higher-lying excited state $|f\rangle$, producing an effective increase in absorbance. This will appear as a negative feature in a 2D map.

In a third-order nonlinear spectroscopy experiment, the rephasing (R) 2D spectrum is composed of three fundamental contributions: ground-state bleaching (GSB), stimulated emission (SE), and excited-state absorption (ESA). These processes are associated with the Liouville pathways R_{4a}, R_{3a}, and R^{*}_{2b}, respectively. Conversely, in the nonrephasing (NR) 2D spectrum, the same physical processes correspond to the Liouville pathways R^{*}_{1a} (GSB), R_{2a} (SE), and R^{*}_{3b} (ESA). In the case of a fourth-order nonlinear spectroscopy experiment, the presence of an additional excitation pulse introduces four distinct features: GSB, SE, and two excited-state absorption channels, denoted as ESA_1 and ESA_2. For the R 2D maps, these contributions arise from the Liouville pathways R_{4a}, R_{3a}, R^{*}_{2b}, and R^{*}_{8b}, respectively. In contrast, for the NR 2D maps, the same features are represented by R^{*}_{5a} (GSB), R_{2a} (SE), R^{*}_{3b} (ESA_1), and R_{7b} (ESA_2). The double-ESA contributions are a direct consequence of the additional interaction in A-2DES, which goes beyond the third-order interaction scheme of conventional C-2DES. Importantly, the two ESA pathways enter with opposite sign. Because the temporal ordering of the first three pulse interactions is identical, the corresponding spectral features appear at the same location in the 2D map. As a result, their superposition can lead to partial or even complete cancellation, depending on the relative strength of the two pathways.[61] This effect has been named *incoherent mixing*.

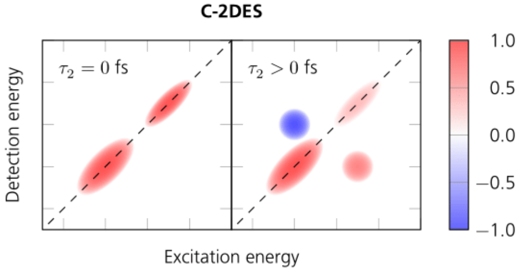

Figure 3.9: Sketch of 2D spectrum. In this figure, it is visualized an example of a 2D map obtained via C-2DES experiment for a hypothetical 3-levels system. At population time $\tau_2 = 0$ fs, the spectrum shows the principal excitonic resonances along the main diagonal, consistent with GSB and SE. As τ_2 increases, off-diagonal cross-peaks emerge, indicating coupling between states and the onset of energy-transfer/relaxation pathways; the diagonal feature of the relaxing state correspondingly diminishes. A negative excited-state absorption (ESA) contribution is highlighted in blue.

Incoherent mixing

Incoherent mixing is a significant experimental artifact that can obscure, distort, or even dominate the true nonlinear response in A-2DES, that could lead to severe misinterpretation of a system's photophysics. The origin of this phenomenon lies in the fundamental difference between A-2DES and C-2DES. While C-2DES directly measures a coherent electric field radiated by the sample, A-2DES detects an incoherent signal, such as fluorescence or photocurrent, which is assumed to be proportional to the excited-state population created by a sequence of laser pulses. The central challenge arises when this assumption of linearity breaks down. In many complex systems, such as multichromophoric assemblies, physical mechanisms like EEA or structural constraints like a single reaction center in a photosynthetic complex introduce a profound nonlinearity between the number of excitons created and the number of excitons detected. This breakdown gives rise to incoherent mixing, where the desired nonlinear signal is contaminated by contributions equivalent to the product of lower-order responses, which do not carry information about the coherent evolution and ultrafast dynamics that 2DES is designed to probe.

To comprehend incoherent mixing and how it can affects the nonlinear response in a 2D map, it is possible to investigate two different approach. In A-2DES, the signal is proportional to the fourth-order excited-state population. However, not all excited states produce population related signal, such as fluorescence or charge separation in photocurrent, with equal efficiency. In other words, the quantum yield of the doubly-excited state manifold can be substantially different from that of the singly-excited manifold. Becomes helpful to understand this picture to define the parameter Γ, which is formally defined as the relative observable (such as fluorescence or photocurrent) quantum yield of the doubly-excited states compared to the singly-excited states.[30,61] In A-2DES, it is reasonable to assume that all singly-excited states have a normalized quantum yield of 1, and all doubly-excited states have a relative quantum yield of Γ, where the parameter encapsulates the efficiency of the detection channel for different quantum pathways. By using the excitation pathways defined in precedence, this can be translated by the following relation:

$$\Gamma = \left| \frac{ESA_2}{ESA_1} \right| \tag{3.46}$$

where the ESA_1 contributes with the same sign as GSB and SE, whereas the ESA_2 contributes with the opposite sign. In an ideal A-2DES experiment with fluorescence detection, the population in a doubly-excited state might decay via a sequential two-photon cascade, emitting two photons. In this hypothetical limit, with two-photons emitted $\Gamma = 2$. However, in most real molecular systems, higher excited states are subject to a multitude of fast non-radiative relaxation pathways. This makes the doubly-excited states far less efficient emitters than the singly-excited states. Consequently, the realistic range for this parameter is $0 \leq \Gamma < 2$. Any value of $\Gamma < 2$ implies that this coherent emission pathway is in competition with incoherent (non-radiative) loss channels. The introduction of Γ leads to a critical modification of the signal equations for 2D FS compared to C-2DES. The terms contributing to the signal can be categorized as GSB, SE, and ESA. For instance, for C-2DES the rephasing signal has the well-known form:

$$S_R^{C-2DES} \propto GSB + SE - ESA \tag{3.47}$$

However, for A-2DES, the corresponding signal expression is fundamentally different due to the additional ESA pathway:

$$S_R^{A-2DES} \propto GSB + SE + [1-\Gamma]ESA \tag{3.48}$$

The crucial difference lies in the $[1 - \Gamma]ESA$ term: for $\Gamma = 2$ the signal reduces to the conventional C-2DES response; for $\Gamma = 1$ only the GSB and SE pathway survive and cross peaks emerge as result of perfect cancellation of ESA features. Therefore, typical signature of A-2DES are cross-peaks appearing since initial population time.

CHAPTER 4

Setup development

Spectroscopy is the point where a theoretical claim becomes a measurable statement. A model predicts how light interacting with a system should change; the instrument records those changes and turns them into numbers that can be compared with theory. The choice of spectroscopic approach fixes what counts as an answer and the optics define what it is actually possible to resolve. In this sense, spectroscopy acts as the translator between hypothesis and observation: when alignment and sample conditions are well controlled, the translation is faithful; when they are not, it tells us more about the setup than the system.

In this chapter, we turn from theory to practice, detailing the architecture of the A-2DES setup developed and implemented in this work. Based on results reported in **Paper I**, the emphasis is focused on the technical essentials, with a focus on proper data handling to obtain clean, reliable data.

4.1 Action-detected 2DES

The laser source (Pharos, Light Conversion) generates laser pulses that are sent into a home-build non-collinear optical parametric amplifier (NOPA) which allows to tune the spectral range of the incoming light source in the visible and near-infrared region with durations compressed to sub-20 fs. The NOPA output is then negatively chirped by using a prism compressor to compensate the medium-induced positive dispersion given by the TeO$_2$ crystal of the pulse shaper. The pre-chirped laser pulse is directed into a single acousto-optic programmable dispersive filter (AOPDF), specifically a Dazzler (Fastlite), which is the core component of the pulse sequence generation. The Dazzler takes the single input beam and, through programmed acousto-optic diffraction, sculpts it into the required sequence of four collinear pulses, labeled E$_1$, E$_2$, E$_3$, and E$_4$. This single device provides complete control over the relative phase of each pulse as well as the inter-pulse delays: the coherence times τ_1 (delay between E$_1$ and E$_2$) and τ_3 (delay between E$_3$ and E$_4$), and the population time τ_2 which is the delay between the first and second pulse pairs. The diffracted beams are then focused onto the sample and the experiment is recorded in the adopting the phase modulation or phase cycling scheme. Based on the type of action signal that has to be measured, a different detection system is implemented. To measure photocurrent, the electrical signal from the sample is recorded directly. This is done by connecting the sample to a National Instruments data acquisition system, specifically a NI cDAQ-9174 USB chassis equipped with an NI-9215 analog input module. For fluorescence detection, an extra step is involved. The emitted light is captured and collimated by an off-axis parabolic mirror featuring a 3-mm through-hole that passes the excitation beam. A lens focuses the fluorescence into a pinhole to reduce scattering, after which a long-pass filter rejects residual excitation. The transmitted fluorescence is re-collimated and imaged onto a high-

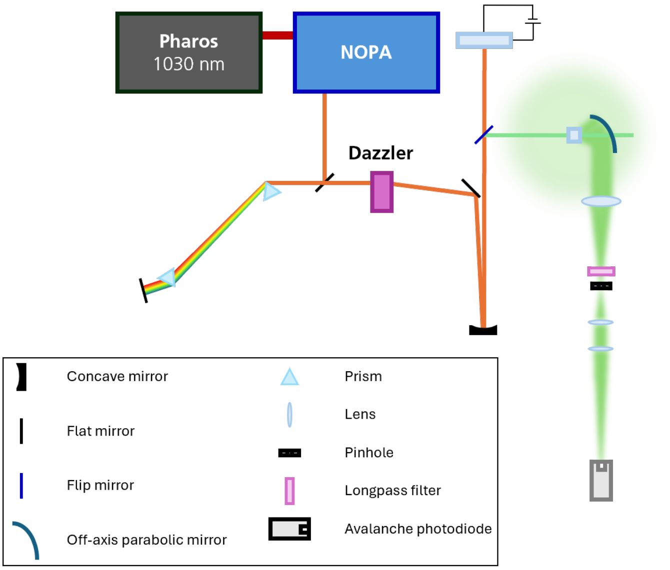

Figure 4.1: .**Setup A-2DES.** Scheme of the optical setup developed. After NOPA, the pulse is pre-chirped through a prism compressor and sent into the Dazzler pulse shaper. The 4 collinear replicas generated are then focused using a spherical mirror directly into the sample. For photocurrent measurement, the signal is collected through a cDAQ system (National Instrument). For fluorescence experiment, the emitted signal is collected by a off-axis parabolic mirror and focused in a APD.

sensitivity APD (Hamamatsu C12703-01). The APD converts this light into an electrical signal, which is then fed into the same National Instruments system for recording. The whole experiment is operate by a custom-built LabVIEW interface that controls all parameters and precisely triggers signal acquisition through a NI-9402 digital I/O module. The experiment's true complexity lies in its advanced components and sophisticated methods, stemming primarily from the technical sophistication of the Dazzler itself. Furthermore, the spectroscopic technique is demanding, requiring precise pulse shaping and careful optimization to accurately retrieve phase modulation data, which leads into a more detailed examination of the Dazzler.

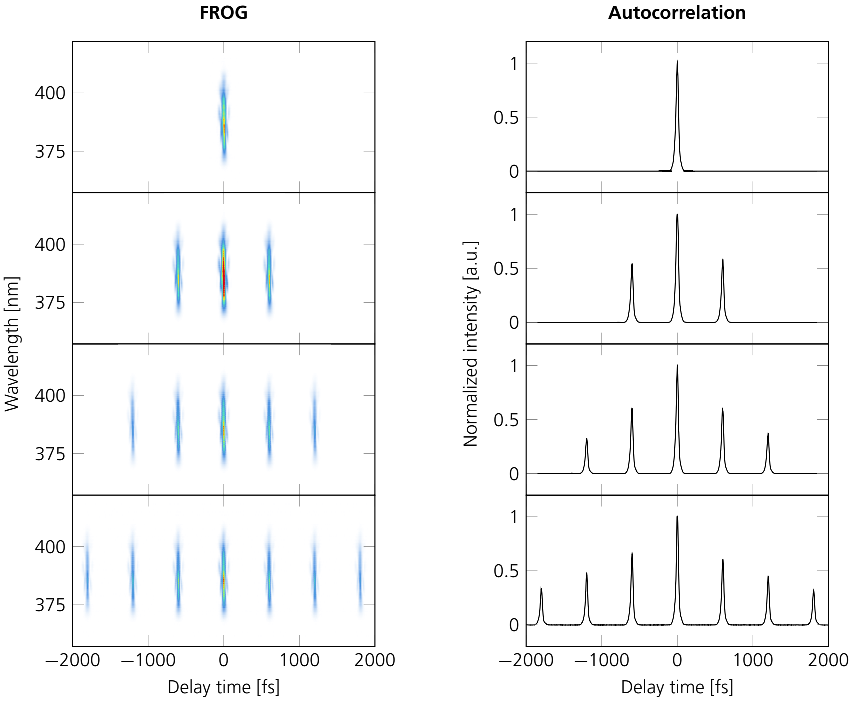

Figure 4.2: SHG-FROG characterization of ultrashort pulses. FROG spectrogram of the second-harmonic signal versus delay time and wavelength, shown with normalized intensity with the respective normalized autocorrelation. The first through fourth rows present SHG-FROG traces and autocorrelation plots corresponding to a single pulse, two pulses, three pulses, and four pulses, respectively.

4.1.1 Pulse characterization

Frequency-Resolved Optical Gating (FROG) was used to retrieve the temporal intensity and phase of the ultrashort pulses employed in our experiments.[16] In a standard second-harmonic (SHG) FROG configuration, the pulse under test is split into two replicas that are noncollinearly overlapped in a thin nonlinear crystal (BBO). By scanning their relative delay and recording the second-harmonic spectrum at each delay, a two-dimensional spectrogram (the FROG trace) is obtained, yielding information over pulse duration, spectral phase (chirp), time–bandwidth product, and the presence of any pre- or post-pulses. For the present work, SHG-FROG was performed to characterize from one up to four shaped pulses generated by the pulse shaper. Measuring after all shaping and delivery optics ensured that the characterization reflected the actual beam incident on the sample. FROG traces recorded in the setup are reported in fig. 4.2.

4.2 Dazzler pulse shaper: phase modulation and technicalities

Dazzler pulse shaper is the essential tool in this setup, allowing not only to compensate first four orders of dispersion, giving full control over the phase of the pulse, but also only being capable to produce replica of the pulses and tuning the time delay between them with great precision.

4.2.1 Phase modulation routine

Phase modulation constitutes a powerful strategy for disentangling linear and nonlinear contributions in coherent multidimensional spectroscopy. In this approach, each of the four collinear excitation pulses produced by the AOPDF pulse shaper is assigned a distinct modulation frequency. The central idea is that by encoding the phase of each pulse with a unique, predictable evolution, the desired nonlinear signals can later be selectively retrieved in the Fourier domain. This provides a robust alternative to conventional phase matching, which is not available in action-detected schemes. Although in principle any four modulation frequencies could be chosen, practical limitations constrain the accessible combinations. The Dazzler system used in this thesis work is limited by its FIFO memory, which permits a maximum of 41 different waveform patterns per streaming session. Furthermore, the FT analysis places an additional requirement: the phase must evolve continuously during signal acquisition. Any abrupt discontinuities in the programmed waveform would manifest as artifacts in the FT spectrum, leading to distorted line shapes and broadened peaks. To address these constraints, the experimental scheme adopted in the different works presented in this thesis work employs a cyclic sequence of N waveforms, defined as the *pattern size*. Each waveform diffracts the incoming femtosecond pulse into four replicas with precisely controlled time delays and relative phases. Therefore, after each modulation step the i-th pulse acquires a phase increment:

$$\Delta\Phi_i = n_i \cdot \frac{2\pi}{N}, \tag{4.1}$$

Table 4.1: Phase modulation routine performed with a laser repetition rate of 4 kHz, with $N = 36$ with divisors $(n_1, n_2, n_3, n_4) = (0, 4, 6, 9)$. The first block delineates the modulation frequencies imparted to the phase of individual laser pulses. The second and third blocks represent the linear and nonlinear contributions, respectively, specifying the frequencies at which the corresponding signals can be extracted. Table adapted from **Paper I**.

Ω_i	$\mathrm{n_i}$	$\Delta\Phi_\mathrm{i}$	Frequency [Hz]
Ω_1	0	0π	
Ω_2	4	$(2/9)\pi$	
Ω_3	6	$(1/3)\pi$	
Ω_4	9	$(1/2)\pi$	
Ω_{21}	$4-0$		444.44
Ω_{31}	$6-0$		666.66
Ω_{41}	$9-0$		999.99
Ω_{32}	$6-4$		222.22
Ω_{42}	$9-4$		555.55
Ω_{43}	$9-6$		333.33
Ω_R	$-0+4+6-9$		111.11
Ω_NR	$-0+4-6+9$		777.77
Ω_2Q	$-0-4+6+9$		1222.22

where $i = 1, 2, 3, 4$ and n_i is an integer divisor of the pattern size N. In this way, the phase of each pulse evolves in a cogwheel-like manner, advancing by a fixed step on each repetition. The modulation frequency associated with each pulse is determined by:

$$\Omega_i = \frac{\mathrm{RepRate\ [Hz]}}{N} \cdot n_i, \tag{4.2}$$

so that the choice of pattern size N and divisors n_i fixes the spectral location of both linear and nonlinear features in the FT spectrum. By carefully selecting these values, one can ensure that the Fourier components corresponding to rephasing (Ω_R), nonrephasing (Ω_{NR}), and linear contributions remain well separated. A pattern size of $N = 36$ with divisors $(n_1, n_2, n_3, n_4) = (0, 4, 6, 9)$ was found to be particularly advantageous, providing clear separation of all contributions. An alternative configuration, $N = 40$ with $(n_1, n_2, n_3, n_4) = (0, 4, 5, 8)$, would in principle also suffice; however, at a laser repetition rate of 4 kHz, the resulting signal frequencies fall at multiples of 100 Hz, dangerously close to harmonics of the 50 Hz laboratory mains. Such overlap would make the experiment highly susceptible to electrical pickup, thereby contaminating the nonlinear spectra with noise. Once the action-detected signal is obtained through FT, linear and nonlinear components can be unambiguously distinguished. First, they are separated by their assigned modulation frequencies. Second, they can be classified by their power dependence. Linear features such as Ω_{21} and Ω_{43} scale linearly with excitation power, whereas nonlinear features (Ω_R and Ω_NR) display higher-order scaling. It is important to realize that the precision of the FT also depends critically on the number of *pattern repetitions*. Streaming the same waveform sequence multiple times serves as an averaging procedure, narrowing the Fourier peaks and improving the signal-to-noise ratio. Insufficient repetitions, on the other hand, result in broader peaks, reduced spectral resolution, and diminished visibility of weak nonlinear signals.

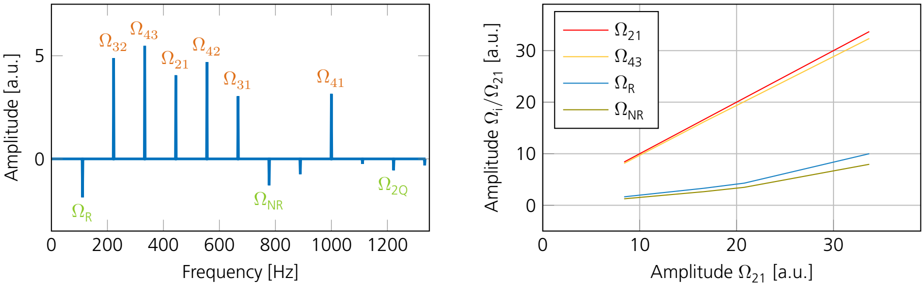

Figure 4.3: Peak assignment for phase modulation scheme and power dependencies of linear and nonlinear features. On the left side are reported the values from tab. 4.1 to the peaks obtained from an experiment using the phase modulation routine performed with a laser repetition rate of 4 kHz, with $N = 36$ with divisors $(n_1, n_2, n_3, n_4) = (0, 4, 6, 9)$. On the right, the dependence of the signal amplitude on laser power is shown for both linear and nonlinear contributions, obtained under the same phase modulation scheme. As expected, the linear components Ω_{21} and Ω_{43} exhibit a direct linear scaling with laser power, whereas the nonlinear features Ω_R and Ω_{NR} display the characteristic higher-order, non-linear power dependencies. Figure adapted from **Paper I**.

4.2.2 Mitigating pulse-shaper induced distortions

Apart of the great advantages given by the Dazzler, some limitations arise due to the confined system and the complicated set of task required.

Distortions related to streaming power. Increasing the Dazzler's streaming power drives the acousto-optic shaper and its radio-frequency (RF) generator amplifier toward a nonlinear regime. In the rephasing time-domain maps this appears as a characteristic, elongated background aligned with the main diagonal, reflecting a power-dependent coupling between the excitation and detection axes. After FT the same distortion folds into frequency space, resulting in a strong elongated feature on the main diagonal of the frequency-domain 2D spectrum, a signature that no longer reflect the true response but a mixture with this RF-induced artifact. In the A-2DES setup developed the onset become clearly visible at $\sim 4\%$ of the shaper's maximum streaming power. This threshold is not universal and will shift with the strength of the recorded nonlinear signal and detection gain.

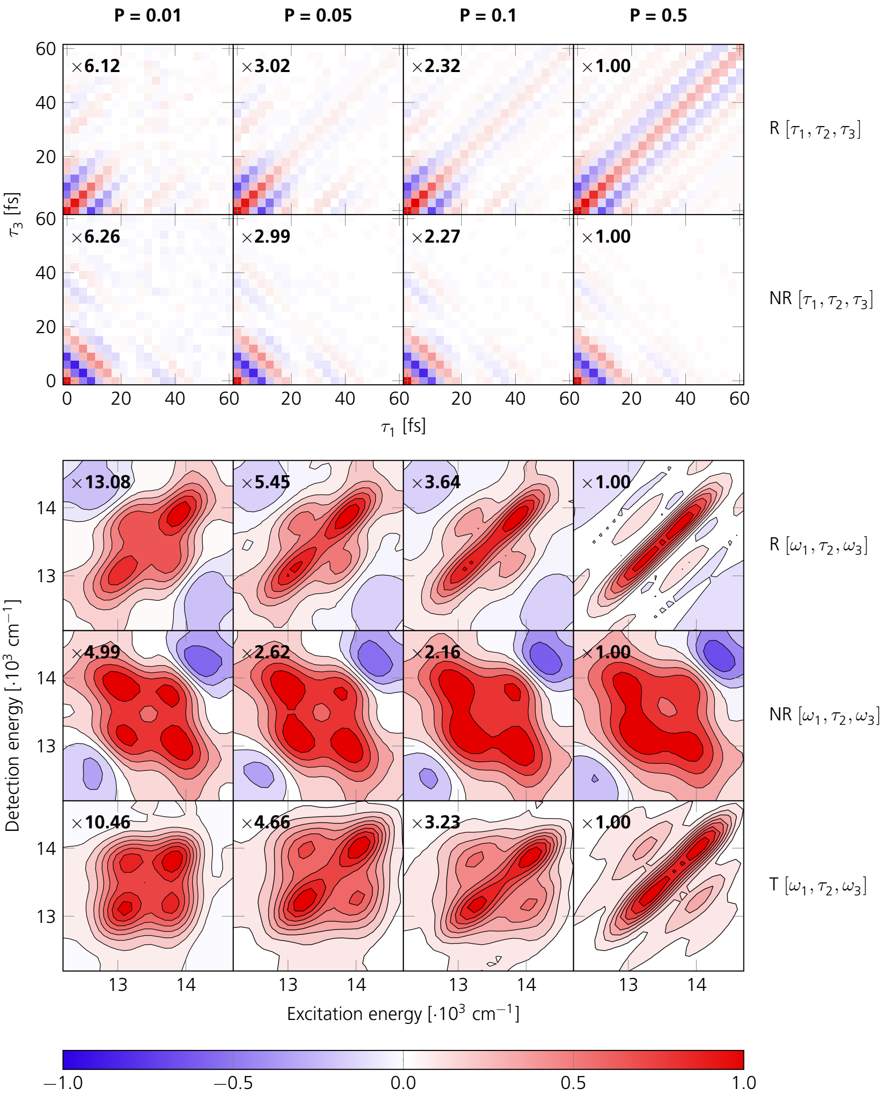

Figure 4.4: Dazzler power-induced distortion. The figure represent A-2DES data recorded on perovskite solar cells at population time $\tau_2 = 100$ fs. Each column refers to an experiment operating under different streaming power of the Dazzler. The upper panel visualizes R and NR maps in time-domain. The lower panel displays R, NR and absorptive (T) maps in the frequency-domain. Each map is normalized to the corresponding map at P $= 0.5$ in the same row, displaying the scaling factor. The 2D maps are visualized using 8 equally spaced contour lines. Figure adapted from **Paper I**.

Distortions related to pulse cross-talking In A-2DES, the use of a single AOPDF pulse shaper to generate all four excitation pulses with precisely controlled phases and time delays provides several important advantages. The most notable are the extreme compactness of the setup and the inherent phase stability, as the entire pulse sequence is defined within a single optical device rather than distributed across multiple interferometers. This architecture minimizes mechanical drift, simplifies alignment, and enhances long-term reproducibility of the measurements. Despite these advantages, the performance of the AOPDF is subject to intrinsic limitations that constrain the accessible parameter space of the experiment. In particular, when the coherence times τ_1 and τ_3 exceed approximately 100 fs, additional features emerge in the recorded signals, as visible in fig. 4.5. These artifacts arise most-likely from nonlinear effects within the acousto–optic crystal of the pulse shaper, that are projected directly into the 2D frequency maps. The presence of such features significantly distorts the spectra, masking system dynamics and complicating quantitative interpretation. A practical and effective strategy to suppress these unwanted contributions is to perform reference measurements under scattering conditions, in which the sample is replaced by a nonresonant scatterer. The 2D map obtained in this configuration reflects only the background nonlinearities of the pulse shaper itself. By subtracting this scattering-derived map from the experimental 2D spectra of the actual sample, one can efficiently eliminate the parasitic contributions, thereby restoring the fidelity of the measurement.

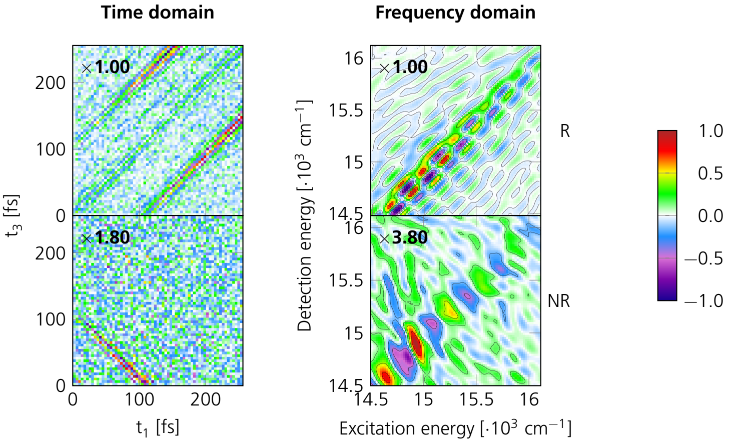

Figure 4.5: Dazzler cross-talking nonlinearities. The figure reveals anomalous features in the scattering measurement. These signatures are most plausibly attributable to nonlinearities in the Dazzler during four-pulse generation, reflecting limitations of the current system. The nonlinearities recorded in time-domain (left) arise as false signals in the frequency-domain (right). Figure reproduced from **Paper V**.

4.3 From raw data to 2D maps in frequency-domain

The extraction of a meaningful 2D spectrum from the raw, modulated time-domain signal acquired in an A-2DES experiment is a multi-step process that relies heavily on the correct application of the FT that allows to retrieve the 2D map in time domain. The ideal workflow involves acquiring the 2D time-domain data matrix, $S(\tau_1, \tau_2, \tau_3)$, for a fixed population time τ_2, and then applying a 2D-FT to convert this into the complex frequency-domain spectrum, $S(\omega_1, \tau_2, \omega_3)$. To obtain the purely absorptive 2D spectrum, which corresponds to the real part of $S(\omega_1, \tau_2, \omega_3)$, the data must be correctly phased. This, in turn, requires precise knowledge of the zero-time-delay point for both the τ_1 and τ_3 scans. However, the application of this ideal mathematical procedure to real, imperfect experimental data can give rise to several significant artifacts. The identification of these artifacts and the development of robust post-processing strategies to correct for them are a central methodological contribution of this dissertation, based on the rigorous analysis presented in **Paper I**. An experiment produces a finite and discretely sampled data set, not the infinite, continuous function assumed by pure Fourier theory. This fundamental mismatch between theory and reality is the origin of some of the distorting features that can arise in the final 2D map, as described below.

Trigger synchronization and removal of non-informative segments

Raw time-domain photocurrent streams contained spurious features at the beginning and end of each acquisition due to limitations in pulse-shaper streaming. Since the laser repetition rate adopted in the experimental procedure exceed the shaper's maximum continuous streaming rate (1 kHz), the RF generator occasionally ignored early triggers while a new waveform pattern finished loading, producing a reproducible irregular segment at the start of each record; additional "tail" points accumulated while the shaper was idle at the end of the pattern. Hardware-synchronization of the data-acquisition electronics to the shaper reduce these effects. Exclusion of the initial loading segment together with terminal tail points before analysis, retains only the true signal portion of each repeated pattern. This procedure enables high-repetition-rate operation without propagating loading artifacts into the spectra.

Precise trimming to enforce integer modulation cycles prior to FT

Performing FT of the phase-modulated time series assumes periodic boundary conditions; therefore, the retained record must contain an integer number of complete modulation cycles to preserve phase continuity at the boundaries. Simulations and experimental data demonstrate that adding or removing even a few points from the optimal count induces phase discontinuities that manifest as spectral leakage, peak broadening, asymmetric line shapes, and spurious frequency components across rephasing, non-rephasing, and absorptive maps. Accordingly, applying precise data trimming to include exactly complete phase-modulation cycles for every pixel prior to FT, restores symmetric, well-localized spectral features.

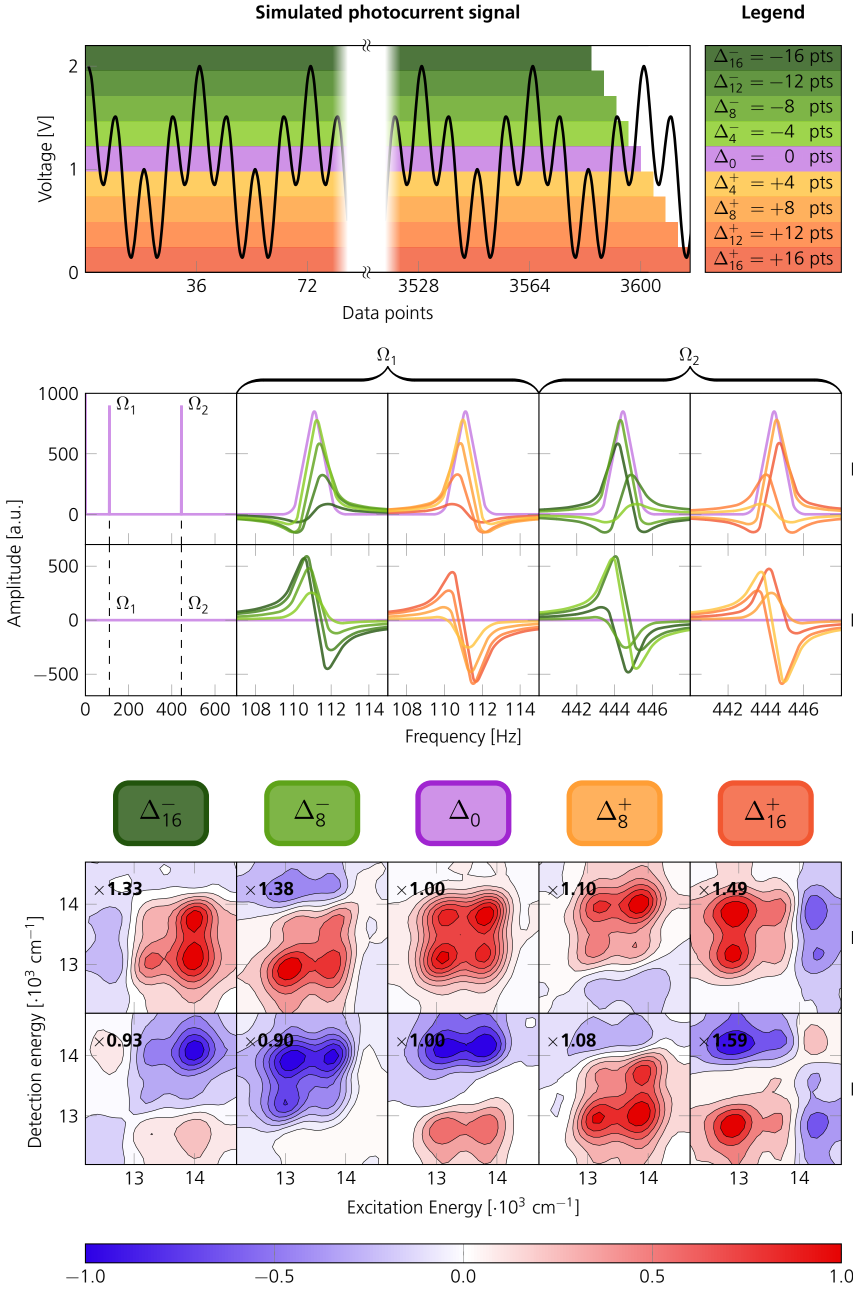

Figure 4.6: Phase distortion due to incorrect data trimming. In the upper panel it is reported a simulated photocurrent signal. Each colour bar covers the amount of data points that are considered for FT: the purple bar refers to the optimal number of points to be considered (Δ_0); the green bars refer to under-sampled data points (Δ_X^-) and the orange bars refer to over-sampled data points (Δ_X^+). The quantity X refers to the number of points that differ from the optimal case. In the middle panel, the FT signal showing the real (Re) and imaginary (Im) components at the two simulated frequencies (f1 and f2) for the different trimming options.. The colour scheme corresponds to the legend. In the bottom panel, the real and imaginary 2D maps measured on solar cell device with subsequent trimming of the dataset at specific values given by $\Delta_X^{\pm}$ with $X = 0, 8, 16$. The resulting picture illustrates the effect of data trimming on the spectral features. The 2D maps are visualized using eight equally spaced contour lines and each row is normalized in respect to Δ_0. Figure adapted from **Paper I**.

Pattern repetition as coherent averaging in the frequency domain

Periodic streaming of the same phase-modulation pattern sharpens the Fourier frequency components that isolate nonlinear pathways and improves signal-to-noise. With a pattern size $N = 36$ at 4 kHz, the linear and nonlinear components appear at integer multiples of $\Omega_i = 4000/36 = 111.11$ Hz; increasing the number of repetitions N_{rep} narrows this component and stabilizes its amplitude, whereas too few repetitions leave broader peaks and lower signal-to-noise. In practice, N, the integer divisors n_i, and N_{rep} were selected jointly to ensure precise recovery of pathway-resolved components.

Correction for population buildup and phase errors

When a population-based signal such as photocurrent is released for a time which is longer compared distance between two consecutive train of pulses, then residual population accumulates between repeated patterns, causing a baseline drift in the photocurrent which is reflected in a phase displacement that distort the 2D spectra. Introducing a resistor allows to actively discharge the accumulated signal before the next population driven signal is collected, avoiding signal accumulation. When discharge could not be used, post-processing procedure is required, where the spectral structure is corrected by multiplying the time-domain rephasing and non-rephasing signals by phase factors $e^{-(i\pi\phi_{\mathrm{R}})}$ and $e^{(i\pi\phi_{\mathrm{NR}})}$, respectively. The magnitude of the distortion scaled with the discharge time constant, emphasizing either enforcing rapid decay experimentally or applying a validated phase-correction routine.

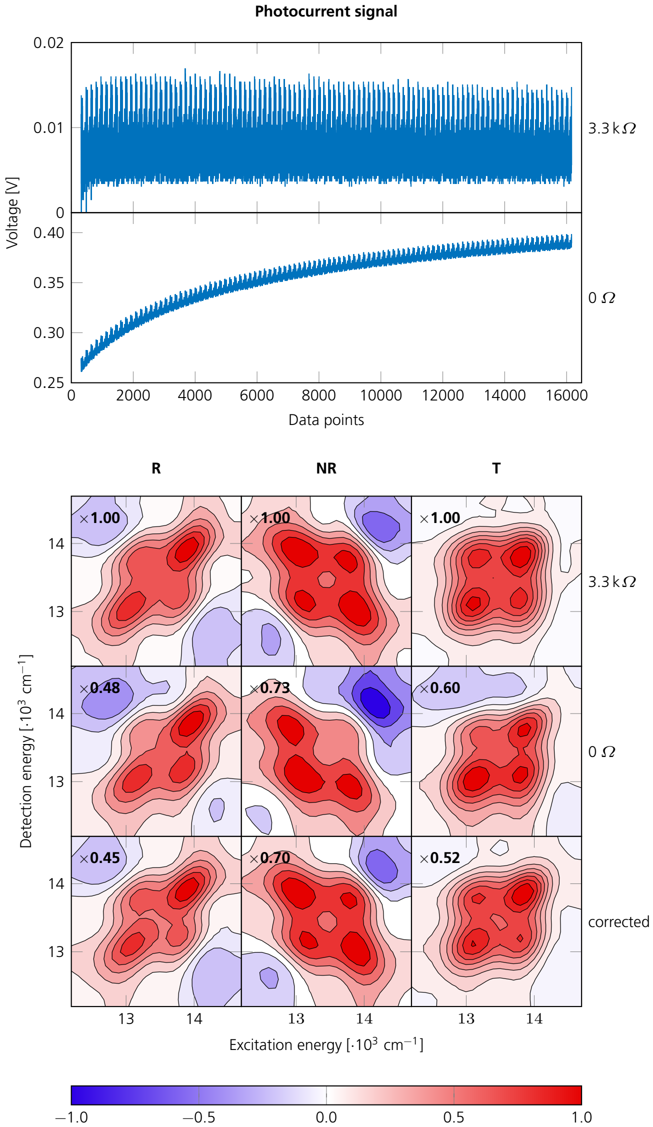

Figure 4.7: **Phase distortion due to signal accumulation.** In the upper panel are reported two measured photocurrent traces at two different circuit resistances: $3.3\,\mathrm{k}\Omega$(upper trace) and $0\ \Omega$ (lower trace). The absence of discharge results in signal accumulation over time. The Corresponding 2D maps in frequency domain, reported in the lower panel, display the consequent effect. The lack of discharge leads to significant phase distortion in the 2D spectra, which can be corrected through post-processing by applying phase factors $e^{-i\pi\phi_\mathrm{R}}$ and $e^{i\pi\phi_\mathrm{NR}}$. The 2D maps are visualized using 8 equally spaced contour lines and each column is normalized in respect to the corresponding map in the first row. Figure adapted from **Paper I**.

CHAPTER 5

Coherent detection: CdSe quantum dots

The rapid technological progress of recent decades has been driven by semiconductors, materials whose tunable electronic structure enables exceptional device performance. Yet, despite spectacular advances, semiconductors remain a vibrant research frontier, especially following the discovery of semiconductor quantum dots (QDs), first observed and characterized in the 1980s.[62–64] Today, QDs underpin a broad range of technologies, from bioimaging, labeling, and sensing,[65–67] to light-emitting diodes (LEDs),[68–70] solar cells,[71–73] and lasers.[74–76] The 2023 Nobel Prize in Chemistry, awarded to Moungi G. Bawendi, Louis E. Brus, and Alexei I. Ekimov for the discovery and synthesis of QDs, underscores the monumental impact of this field.[77]

This chapter outlines the essential physics of quantum dots and highlights key results from **Paper II** and **Paper III**, derived from experimental analysis of broadly size-distributed CdSe QDs.

5.1 Quantum dots: an overview

Quantum dots (QDs) are semiconductor nanocrystals typically measuring 1 to 10 nm in diameter.[78,79] They are often nearly spherical, and a single QD contains on the order of 10^2 to 10^4 atoms, depending on its size.[80] QDs are renowned for optoelectronic properties that vary systematically with size; their defining features are quantum confinement which is associated to their atom-like spectrum of discrete electronic levels. By contrast, bulk semiconductors exhibit energy bands: at 0 K, the valence band is filled and the conduction band is empty, with the two separated by the material's bandgap. Excitation across the gap due to photophysical and thermal processes, such as photon absorption or thermal excitation, promotes an electron to the conduction band and leaves a hole in the valence band. Owing to their Coulomb attraction, the electron and hole bind to form an exciton, a hydrogen-like quasi-particle in which the nucleus role is played by the hole.Recombination of the electron–hole pair releases energy on characteristic radiative or nonradiative timescales. The characteristic electron–hole separation is the excitonic Bohr radius a_{exc},

$$a_{exc} = \varepsilon \frac{m_e}{\mu} a_0 \tag{5.1}$$

where ε is the material dielectric constant, $\mu = \frac{m_e m_h}{m_e + m_h}$ is the electron–hole reduced mass, m_e is the electron rest mass, and a_0 is the Bohr radius of hydrogen, with fixed value of 0.0529 nm. Excitons are broadly classified into two limiting types: Wannier–Mott and Frenkel.[81,82] Wannier–Mott excitons are characteristic of inorganic semiconductors with a large static dielectric constant and small effective masses. Strong dielectric screening ε_r weakens the electron–hole Coulomb attraction, yielding a large excitonic Bohr radius, so that the electron and hole are delocalized over many unit cells and may occupy different lattice sites. In contrast, Frenkel excitons occur in materials with small ε_r where poor screening produces a small excitonic Bohr radius and the electron–hole pair remains tightly bound and localized on the same site. CdSe quantum dots fall between these extremes: in bulk CdSe the exciton is Wannier–Mott–like, but as the crystal size approaches or falls below the excitonic Bohr radius, quantum confinement restricts carrier motion, increases binding, and drives behavior intermediate between the ideal Wannier–Mott and Frenkel limits. To frame the physics of semiconductor nanocrystals, it is useful to define confinement regimes in terms of characteristic length scales. In addition to the exciton Bohr radius, one can define single–carrier Bohr radii for the electron (a_e) and hole (a_h) by using the corresponding effective masses in eq. 5.1 (replacing μ with m_e or m_h, respectively). Comparing the nanocrystal radius a with these three radii yields three limiting regimes.[63,83]

$a_e, a_h < a < a_{exc}$: In large nanocrystals, only the center of mass of the exciton is confined spatially. This is the *weak confinement regime*.

$a_h < a < a_e, a_{exc}$: In smaller nanocrystals, a assume a value in between a_h and a_e. In this situation, only one particle (electron) is strongly confined, but the other (hole) is not. This is the *intermediate confinement regime*.

$a < a_e, a_h, a_{exc}$: In very small nanocrystals, such as QD, both the particles (electron and hole) are strongly confined. This is the *strong confinement regime*.

A quantitative understanding of the size dependence of QD and their electronic properties begins with the single-particle description in bulk semiconductors. In a periodic crystal, electronic states satisfy the time-independent Schrödinger equation:[84]

$$\left(-\frac{\hbar^2}{2m}\nabla^2 + U(r)\right)\psi(r) = E\psi(r), \tag{5.2}$$

m is the mass of the single particle and $U(r) = U(r+R)$ is the lattice-periodic potential. The corresponding energies are commonly represented by a band structure, whose full computation is nontrivial. Within the *effective-mass approximation* (EMA), however, the bands near their edge are well approximated as parabolas. For direct-gap semiconductors, such as for CdSe, the valence-band maximum lies directly on top of the conduction-band minimum and the energy levels can therefore be approximated under the EMA approximation by:[63,84]

$$E_e(k) = E_{gap} + \frac{\hbar^2|k|^2}{2m_e^{eff}} \tag{5.3}$$

$$E_h(k) = -\frac{\hbar^2|k|^2}{2m_h^{eff}} \tag{5.4}$$

where k is the particle wavevector, $m_{e,h}^{eff}$ the electron and hole effective masses and E_{gap} the bulk bandgap. $E_e(k)$ and $E_h(k)$ forms the so called *conduction* and *valence* bands, respectively. When the dimensions of a nanocrystal are much larger than the lattice constant but smaller than the exciton Bohr radius, the *envelope function approximation* (EFA) can be employed. In this framework, the wavefunction is expressed as a superposition of Bloch states weighted by slowly varying envelope functions that satisfy the boundary conditions imposed by the finite geometry of the QD:[84]

$$\psi(r) = u_{n_0}(r)f(r), \tag{5.5}$$

where $u_{n_0}(r)$ is the periodic Bloch function at the band edge and $f(r)$ is the envelope function. The problem of describing carriers in a nanocrystal thus reduces to solving for $f(r)$ under the appropriate confinement potential. A common model to capture the essential physics of confinement is the *particle-in-a-sphere* (PIS) model. Here, the nanocrystal is approximated as a spherical potential well of radius a, infinite outside the boundary and zero inside. The envelope functions are then given by spherical Bessel functions and spherical harmonics, producing discrete, atom-like energy levels characterized by quantum numbers (n, l, m):[85]

$$E_{n\ell}^{e,h} \propto \frac{\hbar^2\alpha_{n\ell}^2}{2\,m_{e,h}^{eff}a^2}, \tag{5.6}$$

where $\alpha_{n,l}$ are the zeros of the spherical Bessel functions. Each electron or hole level is thus described as an orbital confined within the nanocrystal, and the energy spacing increases as the diameter a of the nanocrystal decreases. Therefore, when the crystal is reduced to nanometric dimensions, the picture change drastically. In bulk semiconductors, the periodic lattice allows vast numbers of atomic orbitals to hybridize, producing quasi-continuous energy bands. When the crystal is reduced to nanometer dimensions, the assumption of an effectively infinite lattice no longer holds: only a limited number of unit cells participate and electron motion is bounded by the particle's surfaces. Under these finite-size conditions, the amount of atoms contributing to the band structure reduce, and the formerly smooth bands resolve into discrete, atom-like energy levels, the defining signature of quantum confinements in quantum dots.

In the strong confinement regime, when the nanocrystal radius is much smaller than the exciton Bohr radius, the kinetic confinement energy (scaling as a^{-2}) dominates over the Coulomb attraction between electron and hole (scaling as a^{-1}). The Coulomb interaction can therefore be treated as a perturbation to the independent electron and hole energies. Under this approximation, the lowest excitonic energy can be expressed as[63,85]

$$E_{exc}(a) \sim E_{gap} + \frac{\pi^2 \hbar^2}{2\mu a^2} - \frac{1.8e^2}{\varepsilon a}, \tag{5.7}$$

where μ is the reduced mass of the electron–hole pair. This result demonstrates the essence of the quantum size effect: as a decreases, the bandgap widens, shifting the optical transitions towards higher energies. Therefore, the lowest allowed optical transition shifts to higher energy; correspondingly, the absorption peak moves from red to blue. This blue shift is the direct consequence of quantum confinement. The same transition from bulk to nanoscale is mirrored in the *density of states* (DOS), $\rho(E)$, which counts the number of available electronic states per unit energy. In a system of dimensionality d, the DOS scales as:

$$\rho(E) \propto E^{(d-2)/2} \tag{5.8}$$

Thus, with increasing confinement (effectively reducing dimensionality), the DOS evolves from the smooth three-dimensional form $\rho_{3\mathrm{D}}(E) \propto E^{1/2}$ in bulk, to a step-like, energy-independent $\rho_{2\mathrm{D}}(E)$ in quantum wells, to one-dimensional $\rho_{1\mathrm{D}}(E) \propto E^{-1/2}$ in quantum wires. In zero-dimensional quantum dots, the continuous distribution collapses into a ladder of discrete levels, idealized as a sum of delta functions $\sum_n \delta(E - E_n)$. This discretization of $\rho(E)$, together with the widening gap, underlies the pronounced, size-tunable optical response of quantum dots.[86] In both **Paper II** and **Paper III**, the bandgap widening due to quantum confinement is esplored for sample of CdSe QDs, which reveals intricate photophysics.

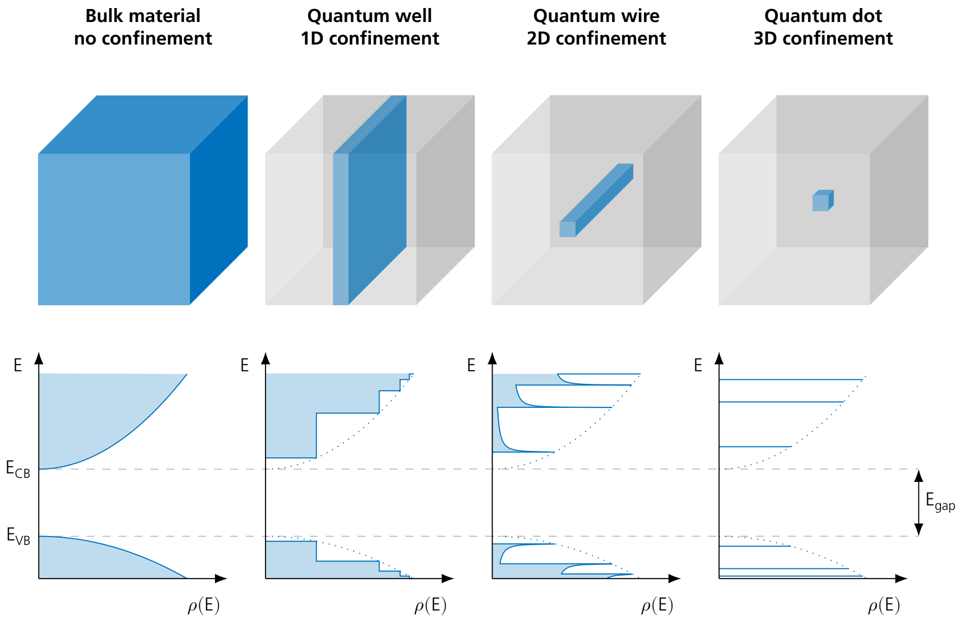

Figure 5.1: Quantum confinement: from bulk to QDs. The figure schematically illustrates how the electronic density of states, $\rho(E)$, evolves as a bulk material is spatially confined to reduced dimensionalities. Under quantum confinement the continuous bands resolve into discrete energy levels, accompanied by a widening of the effective band gap.

5.2 Direct visualization of confinement and many-body correlation effects in 2D spectroscopy of quantum dots

C-2DES was employed to disentangle the severe spectral congestion produced by a deliberately polydisperse ensemble of thiol-capped CdSe quantum dots (nominal diameters ranging from 4 to 8 nm) at 77 K and, within a single measurement, to read out both quantum-confinement trends and many-body correlations (**Paper II**). The primary innovation is the ability to resolve and interpret size-dependent phenomena from a single polydisperse sample, thus providing a direct visualization of quantum confinement. The analysis focuses on a 2D spectrum captured at a population time of $\tau_2 = 270$ fs, a strategic choice that avoids signal distortions from pulse overlap at earlier times and changes from relaxation processes at later times. The spectrum covers three primary excitonic transitions, typical from QDs samples, labeled for brevity as X_1 ($1S_{3/2} - 1S_e$), X_2 ($2S_{3/2} - 1S_e$), and X_3 ($1P_{3/2} - 1P_e$). In the map, the inhomogeneous broadening caused by the QD size distribution manifests as a distinct elongation of the main signal along the diagonal. Crucially, the presence of off-diagonal cross-peaks, which correlate these different excitonic transitions, and their corresponding elongation, directly visualizes how the energy gaps between electronic states change in relation to one another as the QD size varies. To precisely quantify this effect, a ”cross-search” analytical approach has been developed, which consist in finding

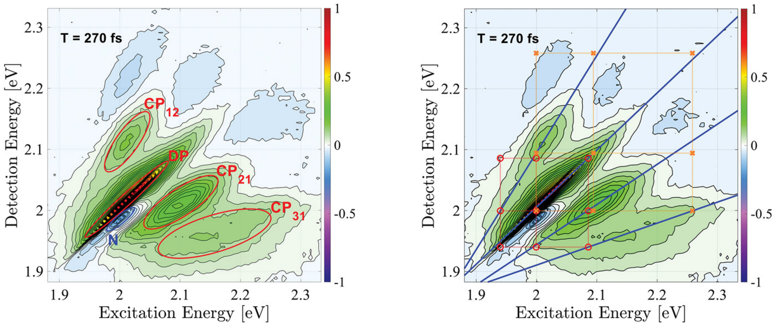

Figure 5.2: Quantum confinment effect in 2D spectrum of CdSe QDs. On the left side, the figure report 2D spectrum at population time ($\tau_2 = \mathrm{T} = 270$ fs), highlighting and labeling the different peaks. On the right side, the figure report blue lines which represent the linear fittings of the main diagonal and cross-peaks. The red (orange) square represents a larger (smaller) CdSe QD, where each circle (cross) along the main diagonal represents X_1, X_2, and X_3 transitions, respectively. The off-diagonal circles (crosses) show the corresponding cross peaks. Figures reproduced from **Paper II**.

the maximum signal intensity for each row and column across the spectral features and then performing a linear fit to these points to determine the exact angle of elongation relative to the main diagonal. The slight tilt of the fitted diagonal band (only a few degrees) arises from the influence of the negative ESA band N. Since the ESA feature partially overlaps the CP_{21} cross-peak, the peak appears marginally less tilted with respect to the main diagonal than CP_{12}. When data points in the vicinity of the ESA feature are excluded, the fit becomes essentially symmetric, in line with theoretical expectations for QD 2D spectra.[87,88] To clarify how the broad size distribution of the QD ensemble gives rise to the observed 2D lineshapes, let's consider two representative particle sizes and their resulting energy levels and spectral signatures. For a relatively large QD, the X_1, X_2, and X_3 transition energies are approximately 1.94, 2.00, and 2.08 eV, respectively; marking the corresponding diagonal and cross-diagonal features with red circles and linking them by red dotted lines yields a square. As a second example, let's choose a smaller QD such that the X_1 transition is at 2.00 eV, coinciding with transition X_2 of the larger QD, and assign its diagonal and cross-diagonal features with orange crosses and dotted lines. Interpolating between the two cases makes transparent how elongated 2D features emerge from the continuous distribution of sizes. Notably, the nondiagonal features CP_{12} and CP_{21} draw contributions from both the $X_1 - X_2$ cross-peak of smaller QDs and the $X_2 - X_3$ cross-peak of larger QDs, leading ideally to a perfectly symmetric pattern. The modest asymmetry observed experimentally has two sources: above the diagonal and at higher energies, the negative ESA signal attenuates positive features, partially in some regions and completely in others, while population relaxation from higher- to lower-energy states enhances the positive features below the diagonal, an effect that becomes more pronounced at longer population times. The spectra recorded allowed to probe many-body correlation effects by examining the biexciton, a state where a single QD contains two electron-hole pairs. The interaction between these four particles (two electrons and two holes) results in a biexciton binding

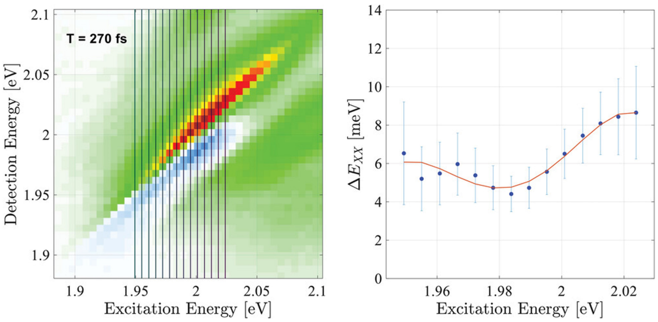

Figure 5.3: Quantum confinment effect in 2D spectrum of CdSe QDs. On the right side, the figure reports the different vertical cut considered for comparison over size-dependent ΔE_{XX}. On the right side is reported the value and the respective errorbars for each ΔE_{XX} associated to the different vertical cuts (different QD size). Figures reproduced from **Paper II**.

energy ΔE_{XX}. To extract the size-dependent binding energy with high precision, vertical slices of the 2D spectrum at different excitation energies were considered, where each slice acts as a transient absorption spectrum for a specific subset of QD sizes. For each vertical slice of the 2D spectrum, ΔE_{XX} was defined as the separation between the maxima of the Lorentzian fits to the GSB and the ESA along the detection axis.

These slices were then fitted with a combination of two Lorentzian functions, to model the positive GSB and the negative ESA features, with additional Gaussian functions to account for overlapping cross-peak signals, allowing for an accurate determination of the energy difference between the exciton and biexciton transitions:

$$f(x) = \sum_{n=1}^{2} \frac{a_n}{\pi} \left(\frac{c_n}{(x - b_n)^2 + c_n^2} \right) + \sum_{i=3}^{5} a_i e^{-\left(\frac{(x-b_i)^2}{c_i^2} \right)} + d \tag{5.9}$$

While the absolute values obtained at different population times vary modestly (ΔE_{XX} for a given X_1 differs by roughly 2 meV) these shifts are readily ascribed to relaxation dynamics and vibrational coherences that subtly reshape the spectra. Importantly, the overall trend is robust: at all population times ΔE_{XX} exhibits a clear minimum at an X_1 transition energy slightly above 1.98 eV. Moving to higher excitation energies (smaller QDs) produces an unequivocal increase of $\sim$ 6 meV over an $\sim$ 40 meV span, essentially independent of population time. Toward lower excitation energies from 1.98 eV (larger QDs), the rise is gentler but still exceeds the analysis uncertainty, amounting to $\sim$ 2 meV over $\sim$ 20 meV. These results align with and refine the established picture of exciton–exciton interactions in CdSe. In the bulk, excitons are weakly attractive with a biexciton binding of $\sim$ 4 meV,[89] and attractive coupling has also been observed in CdSe quantum dots.[90] Because coupling involves two electrons and two holes, it is an intrinsically four-body problem governed by wavefunction overlaps. In type-II core-shell structures, spatial separation of electrons and holes drives electron-electron and hole-hole Coulomb repulsion and can yield net repulsive coupling.[91,92] In the experiment ensemble investigated in this work, it is observed an attractive ΔE_{XX} with a pronounced non-monotonic size dependence: the binding strengthens for both smaller and larger dots, reaching a minimum at a diameter of $\sim$ 6 nm. The increase upon reducing size from $\sim$ 6 to $\sim$ 4 nm mirrors earlier reports[90] and is broadly consistent with the expectation that stronger confinement amplifies interactions. At the large-size end ($>$ 6 nm), the upturn in ΔE_{XX} is unambiguous. The minimum in our ΔE_{XX} coincides with a diameter near the exciton Bohr radius.[93,94] As size increases beyond this point, exciton overlap diminishes toward bulk-like conditions; the consequent reduction in electron-electron and hole-hole repulsion, alongside concomitant changes in other interaction terms, plausibly accounts for the observed increase in the total biexciton binding energy for QDs larger than the Bohr radius.

5.3 Excited states and their dynamics in CdSe quantum dots studied by two-color 2D spectroscopy

By combining extended spectral coverage with high temporal resolution, the study reported in **Paper III** uncovers crucial aspects of carrier relaxation and phonon coupling in QDs.

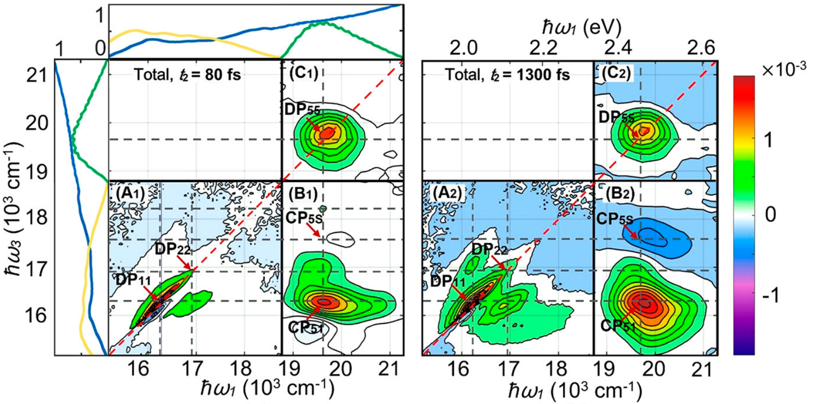

(a) (b)

Figure 5.4: **2D maps for broad size distribution of CdSe QDs measured with two-color 2DES.** Real part of the total 2D spectroscopy signal at two population times ($\tau_2 = t_2 = 80$ and 1300 fs), assembled from three separate single-color (A and C) and two-color (B) measurements. The black horizontal dashed lines mark the positions of the states $|e_1\rangle$, $|e_2\rangle$, $|e_3\rangle$, $|e_4\rangle$ and $|e_5\rangle$ at 16200, 16900, 17800, 18300, and 19700 cm^{-1}, respectively. The three vertical lines mark the states which lead to the clear cross peaks. The labeled diagonal peaks (DP) and cross peaks (CP) are discussed further in the text. The leftmost and topmost panels show the laser spectra (yellow and green curves) and the absorbance of CdSe QDs at 77 K (blue curves). Figure reproduced from **Paper III**.

Two-color 2DES experiments has been performed on thiol-capped CdSe QDs at cryogenic temperature (77 K).[95,96] The use of pump pulses resonant with higher-lying states (18800–21300 cm^{-1}) in combination with probe pulses probing lower-energy transitions

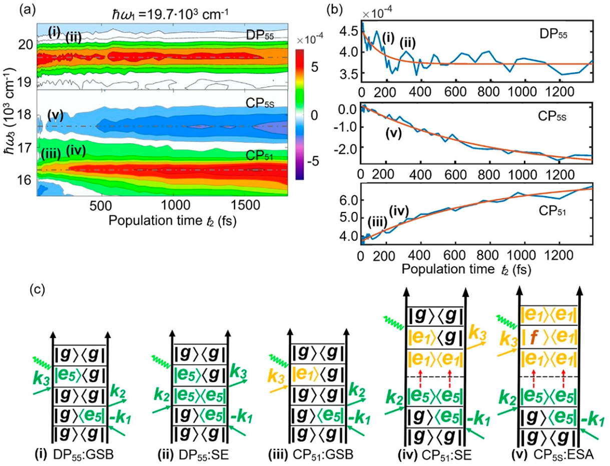

Figure 5.5: Kinetics of DP55, CP51 and CP5S features. Population-time dependence of the main spectral features. (a) The real part of the three main peaks of the rephasing 2D spectra as a function of the population time t_2. (The results without normalization can be found in the Supporting Information.) (b) Kinetics of the three main peaks DP_{55}, CP_{5S}, and CP_{51}. The exponential decay and rise times of the three curves are 100 ± 10, 700 ± 50, and 700 ± 50 fs, respectively. (c). Feynman diagrams (i) and (ii) are the GSB and SE pathways for the DP55 peak. Feynman diagram (iii) represents the GSB pathway for the CP_{51} peak. Feynman diagram (v) indicates the relaxation processes of CP5S. Figure reproduced from **Paper III**.

near the band edge (15200–18800 cm^{-1}) allowed to map an unusually broad spectral window that is inaccessible in conventional single-color 2DES.[97–99] This strategy revealed a complex network of diagonal and cross peaks, among which the diagonal features DP_{11}, DP_{22}, and DP_{55}, and the cross peaks CP_{51}, CP_{52}, and CP_{5S}, are particularly significant. A synoptic view of the total 2D spectra is reported in fig. 5.4, where the maps are assembled from single- and two-color measurements, with diagonal positions marking the excitonic resonances $|e_1\rangle$ through $|e_5\rangle$, assigned according to the standard nomenclature used for QDs.[100] The most crucial state in this analysis is $|e_5\rangle$, observed at $\sim$ 19700 cm^{-1}, which gives rise to the diagonal peak related to population excited state named DP_{55} and dominates the relaxation dynamics.

The temporal evolution of these spectral features during the first 1.4 ps of population time revealed distinct relaxation timescales. The decay of DP_{55}, which reflects the GSB and SE processes associated with $|e_5\rangle$, occurs with a characteristic time of $\sim$ 100 fs, indicating ultrafast depopulation of the initially excited state. In contrast, the rise of the cross peaks CP_{51} (which couples $|e_5\rangle$ to $|e_1\rangle$) and CP_{5S} (a feature initially associated to a trap state that can be recalled to an ESA band around 17500 cm^{-1}) follows a markedly slower timescale of $\sim$ 700 fs. This duality at first appeared contradictory: since the time scale for the decay of $|e_5\rangle$ state differs from the rising time of the final $|e_1\rangle$ state. The resolution lies in the mechanism of relaxation: because the energy gap between $|e_5\rangle$ and $|e_1\rangle$ ($\sim$ 3400 cm^{-1}) is much larger than the CdSe longitudinal optical phonon energy ($\sim$ 200 cm^{-1}), the relaxation requires a cascade-like relaxation process with more than 15 steps.[101] This multistep phonon-assisted relaxation reconciles the apparent discrepancy between the rapid depletion of the initial excited state and the comparatively slow rise of population at the band-edge states. Importantly, the rise of CP_{5S} with the same 700 fs timescale as CP_{51} strongly suggests that the ESA long attributed to long-lived trap states is, in fact, better understood as absorption of carriers that have already relaxed to the conduction-band edge.

CHAPTER 6

Photocurrent detection: ultrafast dynamics in perovskite solar cell

Sunlight is everywhere, but turning it into electricity can be a challenging and expensive process. Perovskites change that story. They can be seen as a friendly crystal recipe, simple ingredients that can be mixed like inks and spread into thin, shiny skins. Lay one of these films on a surface, add a few helper layers, and suddenly that patch can harvest light that can be turned into useful current. What makes perovskites special is how easy they are to retune. by changing the composition, the film changes how much and which part of the solar radiation it can absorb. They don't need heavy process: a thin absorbing layer can be made easily made by coating, or through gentle vapor steps. That simplicity opens doors: lightweight panels, flexible sheets, and even a clear layer that sits on top of silicon to squeeze more power from the same sunlight. There are still grown-up problems. These crystals can be touchy with heat and moisture, and they need good protectors and smarter recipes to stay steady outdoors. But the direction is clear: perovskite take the idea of solar power and make it feel closer. If the system will be ingegnerized to become stable at room temperature, affordable and clean electricity can be produced almost anywhere light falls. And this is where spectroscopy can play a crucial role by measuring what actually happens inside the material after it absorbs light. With that information, chemistry and processing can be adjusted, such as optimized compositions, so devices deliver higher current and voltage and keep those gains under real operating conditions. Solar cells are multilayered stacks, and many optical probes struggle to deliver meaningful signals through reflections, scatter, and parasitic backgrounds, driving down the signal-to-noise ratio. A technique that can deal with these challenges is A-2DES, an approach that reads the cell's own response as photocurrent, while phase-modulate (or -cycled) lock-in detection suppresses reflections, scattering, and parasitic backgrounds by isolating the fourth-order nonlinear signal enabling investigation of ultrafast dynamics in complex multilayered solar architectures under realistic operating conditions.

In this chapter, the first part presents a generic description of perovskite is given, from the material properties to the fully working solar cell device characteristic. The second part summarizes **Paper IV**: an in-depth A-2DES study of high-efficiency perovskite solar cells with varied organic A-cations, revealing how the spacer influences the device ultrafast dynamics.

6.1 Fundamentals of perovskite

The word *perovskite* began as a mineral name: in 1839 Gustav Rose identified calcium titanate, $CaTiO_3$, in the Ural Mountains and named it after the Russian mineralogist Lev Perovski.[102,103] Oxide perovskites (with X = O) underpin much of the past century solid-state physics and technology through ferroelectricity,[104,105] piezoelectricity,[106,107], magnetism,[108,109] and even unconventional superconductivity[110] in related structures. Over the following century, the term shifted from a single oxide mineral to a broad structural family defined by a three-dimensional framework of corner-sharing BX_6 octahedra with larger A-site cations nested in the cuboctahedral cavities, yielding the archetypal ABX_3 motif. The ABX_3 structure is defined by the precise geometric arrangement and distinct roles of its three constituent components: the A-cation, the B-cation, and the X-anion.[111] The fundamental building block of the entire framework is the BX_6 octahedron, which is formed by the smaller B-cation situated at the center of the unit cell, where it is coordinated with six X-anions located at the faces of the cubic cell.[112] A defining characteristic of the perovskite architecture is the way these BX_6 octahedra link together by sharing their corners, creating a continuous and stable three-dimensional network. Among the possible perovskite materials discovered so far, in the past few decades metal-halide perovskites emerged as valuable semiconductors for optoelectronics, rapidly progressing from early dye-sensitized[113] to thin-film solar cells[114–117], light-emitting diodes (LED),[118,119] and photodetectors[120,121]. The thin-film photovoltaics based on metal–halide perovskites, simply known as perovskite solar cells (PSCs), present a composition for which A is a monovalent cation, B is typically a bivalent metal, and X is the halide. The key optoelectronic properties relevant to PSCs are governed by the geometry and connectivity of this corner-sharing BX_6 octahedral framework: B−X−B bond angles and B−X bond lengths set the orbital overlap between metal s/p and halide p orbitals, thereby directly controlling the electronic structure and the magnitude of the band gap of the perovskite system. The most common X anions are

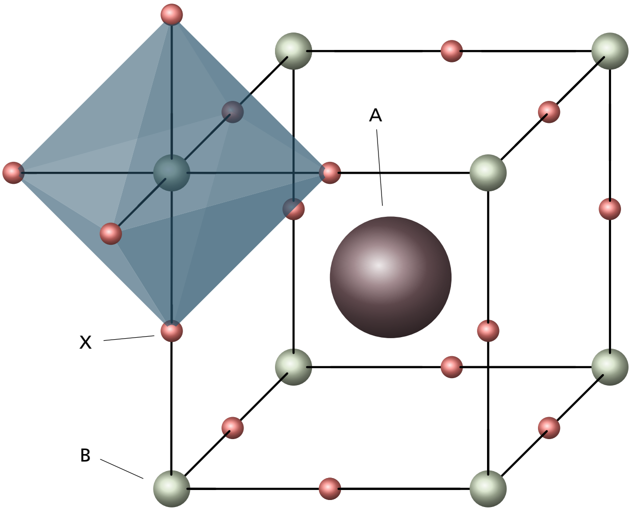

Figure 6.1: Perovskite ABX_3 crystal structure. This figure visualize the ABX 3 perovskite crystal structure showing the BX_6 octahedral and larger A cation occupied in cubo-octahedral site.

the halides Cl^-, Br^-, and I^-, with ionic radii of 181, 196, and 220 pm, respectively. The identity of the halide is a primary tool for tuning the material's properties; as the halide radius decreases, the B-X bond contracts, strengthening orbital overlap and systematically widening the band gap. The B-site cation, which is octahedrally coordinated by these six halide anions, must satisfy a geometric constraint known as the *octahedral factor*:

$$\mu = \frac{r_\mathrm{B}}{r_\mathrm{X}} \tag{6.1}$$

which ensures that the B cation can be stably sixfold coordinated. Deviations from the ideal cubic structure appear as cooperative tilts of the octahedra, which narrow the electronic bands, and typically widen E_{gap} while impacting carrier mobility and radiative efficiency. While several elements have been explored for the B-site, lead (Pb^{2+}) remains the most extensively studied and successful cation, setting the performance benchmarks for the entire field. Although toxicity concerns have motivated a search for alternatives, with tin (Sn^{2+}) being the most viable substitute due to its identical valence-shell configuration (s^2p^2), lead-based materials continue to exhibit superior overall performance.[103] Tin's smaller ionic radius (69 pm) compared to lead's (119 pm) alters the orbital overlap, yielding a narrower and often more theoretically ideal bandgap of 1.3-1.4 eV, yet its chemical instability remains a critical challenge. The success of lead is fundamentally tied to its suitable ionic radius, which ensures a stable octahedral framework with iodide, and its unique electronic configuration. The overlap between Pb 6s and halide np_z orbitals ($n = 3, 4, 5$ for Cl, Br and I, respectively) along the Pb—X bond generates σ-bonding and σ^*-antibonding pairs, while the orthogonal X np_x and np_y orbitals are largely nonbonding with respect to Pb 6*s*. Hybridization of Pb 6*p* with X *np* produces one σ-bonding combination ($6p_z np_z$) and two π-bonding combinations ($6p_x - np_x$ and $6p_y - np_y$), together with their corresponding σ^* and π^* antibonding counterparts; $s-p$ mixing tends to raise the σ^* manifold relative to π^*, rendering the latter comparatively more stabilized. Consequently, the *highest occupied molecular orbital* (HOMO) is dominated by the antibonding $\sigma^*(\text{Pb } 6s - \text{X } np)$ level, whereas the *lowest unoccupied molecular orbital* (LUMO) is primarily Pb 6*p* in character, comprising σ^* and π^* combinations with X *np*. Upon condensation into the three-dimensional perovskite, these molecular levels broaden into bands: the valence-band maximum inherits mainly X *np* weight from $\sigma^*(\text{Pb } 6s - \text{X } np)$, and the conduction-band minimum is chiefly Pb 6*p*.

While the BX_6 network directly dictates these electronic properties, the stability and fine-tuning of this three-dimensional framework are critically dependent on the size and nature of the A-site cation that occupies the interstitial cuboctahedral cavity.[122] This larger cation has a 12-fold coordination, as it is surrounded by twelve of the nearest X-site anions.[123] The ability of the perovskite structure to accommodate exceptionally large cations at this A-site is a unique feature not commonly found in other close-packed crystal structures. The stability and formation of a specific ABX_3 compound as a perovskite is governed by the relative sizes of its constituent ions, a relationship quantified by the *Goldschmidt tolerance factor*:[124]

$$t = \frac{r_A + r_X}{\sqrt{2}(r_B + r_X)} \tag{6.2}$$

This empirical parameter relates the ionic radii (r_A, r_B, and r_X) and predicts whether the ions can geometrically fit into the ideal cubic arrangement.[125] An ideal, highly symmetric cubic perovskite structure is achieved when t is exactly 1, while stable perovskite phases are typically formed for tolerance factors in the range of 0.8 to 1.0.[75] If the A-site cation is too large or too small relative to the framework, causing the tolerance factor to fall outside this range, the structure becomes unstable and will preferentially form other, non-perovskite crystal configurations. In few words, the A-site cation , serves as a geometrical spacer for the BX_6 octahedra in a 3D perovskite to prevent distortion. Therefore, depending on the size and symmetry of the A cation, the bond distance and angle between B and X can be changed to affect the the bandedge state.

The two most used A cation spacers are methylammonium (MA) and formamidinium (FA). MA^+ cation has ionic radius of 217 pm, yielding a tolerance factor of 0.91, forming a tetragonal perovskite with characteristic bandgap of 1.51 eV at room temperature, featuring a slight distortion from a cubic structure, and undergoing a phase transition to a cubic phase at elevated temperatures of 54–57 °C. A key feature of this spacer is its dynamic behavior, which reorient within the octahedral cage on a very short timescale, having a residence time of approximately 14 ps at room temperature.[126] This rapid reorientation is suggested to stabilize energetic charge carriers through the formation of a large polaron, a process which in turn enhances the lifetime of both hot carriers and band-edge carriers. However, this same dynamic disorder also highlights a significant weakness: the bond between the A-site cation and the PbX_6 octahedra is relatively weak.[127,128] As a consequence, the degradation of $MAPbX_3$, particularly when exposed to illumination or heat, is typically triggered by the volatilization of the cation itself. On the other hand, limitation due to MA-based PSCs relatively large bandgap and lower charge-carrier mobility are driving against realization of highly efficient devices. To overcome these drawbacks, a different organic A cation was proposed, the FA. The photoactive cubic phase of $FAPbX_3$ exhibits a more ideal, lower bandgap of 1.48 eV along with significantly longer charge-carrier lifetimes and diffusion lengths.[129] Furthermore, solid-state NMR measurements have shown that the FA^+ cation reorients much more rapidly (8.7 ± 0.5 ps) than the MA^+ cation (108 ± 18 ps), suggesting a superior capability for stabilizing charge carriers.[130,131] However, the main drawback for $FAPbX_3$ is the phase instability. At room temperature, it tends to crystallize into a photo-inactive, non-perovskite hexagonal phase with a wide bandgap of 2.43 eV.[132] This tendency is likely related to the large ionic radius of the FA^+ cation (253 pm) and a near-ideal tolerance factor of 0.99, which introduces intrinsic lattice strain.[122] The desirable cubic phase can be formed by annealing above 150 °C, but this phase is only metastable at room temperature, with an energy barrier of approximately 0.6 eV for the reverse phase transition.[133] This degradation back to the hexagonal phase is significantly accelerated by moisture, which can attack the crystal surface and create defects that lower the energy barrier for the transition.[134,135] One of the aim of this thesis is to understand in a deeper way how these different organic A cations influence the charge-carrier dynamics in perovskite solar cells, thereby informing strategies to mitigate carrier recombination and enhance long-term stability, some of the challenges in PSCs field.[136]

6.2 Perovskite solar cell structure

Over the past four decades, the global push to raise photovoltaic conversion efficiency has been a story of steady, multi-technology progress, captured succinctly by NREL's Best Research-Cell Efficiency chart.[137] Early crystalline-silicon records in the chart's first years gave way to today's high-20% single-junction Si cells, while single-junction GaAs advanced to roughly 29%. At the same time, multijunction III-V stacks under concentration have climbed toward the high-40% range (with points near 47.6%), illustrating the power of bandgap stacking and optical concentration. The last decade added a new arc: metal-halide perovskites leapt from single digits to about 27% in single-junction cells and, when paired with silicon in two-terminal tandems, pushed confirmed records past 36% by 2025. In particular, PSCs have reached outstanding efficiencies rather quickly thanks to materials and device engineering coupled with meticulous parameter tuning. PSCs are broadly classified as *n-i-p* or *p-i-n* according to the direction of charge collection at the illuminated substrate. In *n-i-p* devices, the electrons are collected on the same side of the incident light,

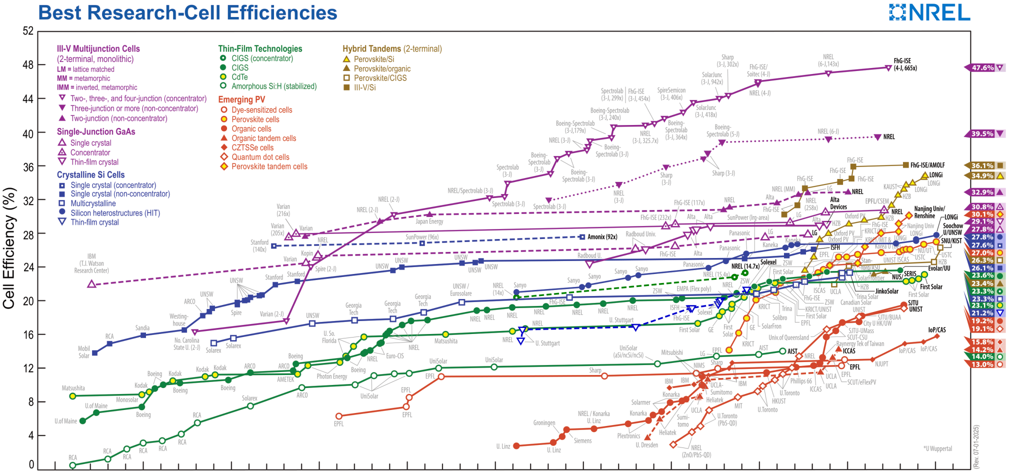

Figure 6.2: **Best research-cell efficiencies** The graph displays the highest confirmed conversion efficiencies for research cells for a range of photovoltaic technologies, plotted from 1976 to the present.[137]

whereas in *p-i-n* devices the holes are instead collected from the same side of incident light. In the regular *n-i-p* stack, the structure is assembled through a sequence of selective layers: a transparent substrate, an electron transport layer (ETL), the perovskite absorber, a hole transport layer (HTL), and electrodes on top.

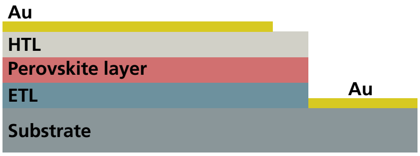

Figure 6.3: **Sketch of *n-i-p* perovskite-based solar cell device.** This figure visualize the typical layers subdivisions which compose the most researched perovskite-based solar cells. From bottom to top, the glass substrate is covered with the ETL layer, followed by the perovskite absorbing layer and then the HTL layer. On top, the whole structure is all capped by metal electrodes that complete the device capped by metal electrodes that complete the device.

More in details, the transparent glass substrate, typically covered with a thin layer of ITO or FTO, provides lateral conduction and optical access. Selective contacts enforce one–carrier extraction and block the other to suppress interface recombination. An optimal ETL material, such as SnO_2 exhibits good conduction band alignment with perovskites, high electron mobility, wide bandgap, high transmittance, and good stability. In a similar fashion, spiro-OMeTAD is one of the leading HTL material due to the good energy level alignment with perovskite materials, and easy solution processability. Energy–level alignment is tuned so that the conduction- and valence-band offsets between the different layers are small steps rather than cliffs, promoting fast, selective extraction while maintaining a large splitting between conduction and valence bands. The perovskite absorber is deposited by solution to finely control nucleation, grain size, and defect density. Additives, antisolvent timing, and adduct intermediates yield dense films lowering the trap densities, while post–treatments (alkylammonium halides, FAI, MACl) passivate surfaces and grain boundaries. The back electrode is often a conductive material such as Au, Ag.

6.3 Investigating organic A-cation influence on carrier dynamics of encapsulated perovskite solar cells using PC-2DES

Photocurrent-detected 2DES (PC-2DES, an implementation of A-2DES) has been used to examine three perovskite solar cell (PSC) architectures incorporating active layers with distinct organic A-site cation compositions. Specifically, varying ratios of formamidinium (FA) and methylammonium (MA) were employed to realize the following perovskite stoichiometries: (i) $FAPbI_3$ (FA), (ii) (FAPbI3)0.992($MAPbBr_3$)0.008 (FAMA, range of ratio mixture that has been shown some of the highest PSCs efficiency),[42,112,138,139] and (iii) $MAPbI_3$ (MA). The corresponding absorption spectra are shown in fig. 6.4. A pronounced blue shift is observed for the MA film relative to the FA and FAMA films, primarily reflecting the higher MA content: reducing the A-site ionic radius contracts the lattice and widens the bandgap. A subtler but clear blue shift in FAMA compared with FA arises from the combined effects of mixed A-site cations (FA/MA) and mixed X-site halides (I/Br). As discussed above, introducing MA increases the bandgap, while partial substitution of I by the smaller Br shortens B-X bonds, strengthens orbital interactions, and further widens the bandgap, collectively shifting absorption to the blue. The magnitude of this shift in FAMA remains modest, consistent with the very low $MAPbBr_3$ fraction in the mixed perovskite.

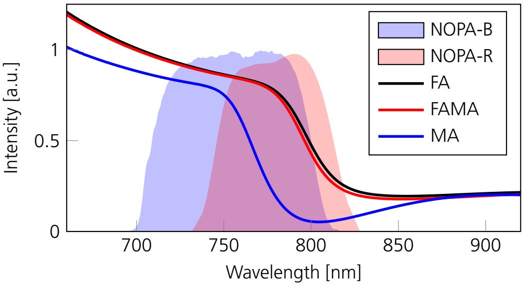

Figure 6.4: PSCs absorption spectra and excitation bandwidths. Absorption spectra of the three PSCs studied in this work: $FAPbI_3$ (FA), (FAPbI3)0.992(MAPbBr3)0.008 (FAMA), and $MAPbI_3$ (MA). Shaded regions indicate the noncollinear optical parametric amplifier (NOPA) spectra: NOPA-R (red), used for FA and FAMA, and NOPA-B (blue), used for MA. Figure adapted from **Paper IV**.

PC-2DES is used to investigate PSCs dynamics by directly recording the devices photocurrent, enabling measurements on fully encapsulated, operational PSCs under realistic working conditions. This approach captures the evolution of photoexcited states and connects ultrafast dynamics directly to the device performance. In fig. 6.5 are presented the 2D maps recorded for each sample at initial (after coherent artifact) and later population times. To improve the signal-to-noise ratio, each map represents the average of two independent measurements at different positions on the same device. At early population times, all samples exhibit similar spectral signatures, featuring responses symmetric about the main diagonal over the explored spectral window. GSB dominates at these initial delays. As the population time increases, carrier-relaxation processes emerge: within the first 2 ps, carriers cool from higher-lying conduction-band states toward the band edge, most clearly visible as evolving off-diagonal features at higher to lower detection energies.

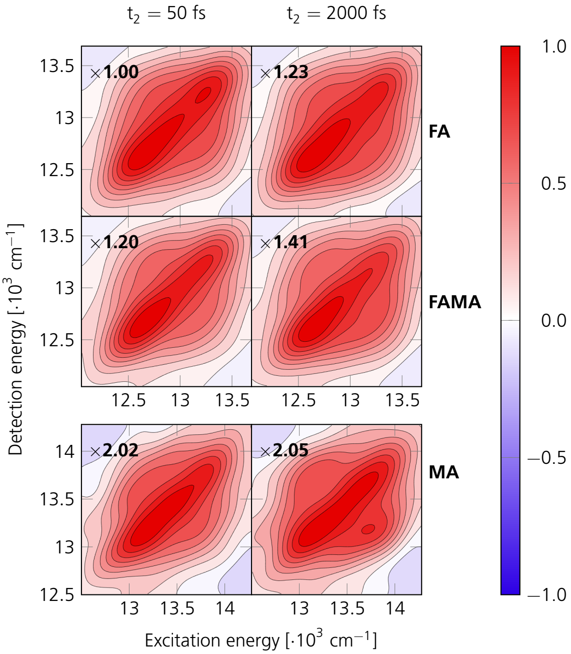

Figure 6.5: PC-2DES maps of solar cell devices with different perovskite layer composition. 2D maps at 50 fs and 2 ps are presented for each of the devices investigated. The first, second and third row correspond to FA, FAMA, and MA devices, respectively. To facilitate comparison, each 2D map is scaled relative to the FA map at 50 fs by the scaling factor indicated in the respective panels. Figure adapted from **Paper IV**.

As discussed throughout the thesis, A-2DES can exhibit spurious signals from incoherent mixing. Owing to the long detection window, carriers generated separately by the pump and by the probe-pulse sequence can interact via nonlinear processes (most notably Auger recombination for semiconductor materials) producing bleach-sign features that are symmetric about the main diagonal of the 2D spectrum. Many-body Auger recombination is often associated with structural imperfections (e.g., grain boundaries and imperfect interfaces); accordingly, in high-efficiency devices where nonradiative losses are minimized, incoherent-mixing signals are expected to be weak or absent. In fig. 6.6 are visualized the

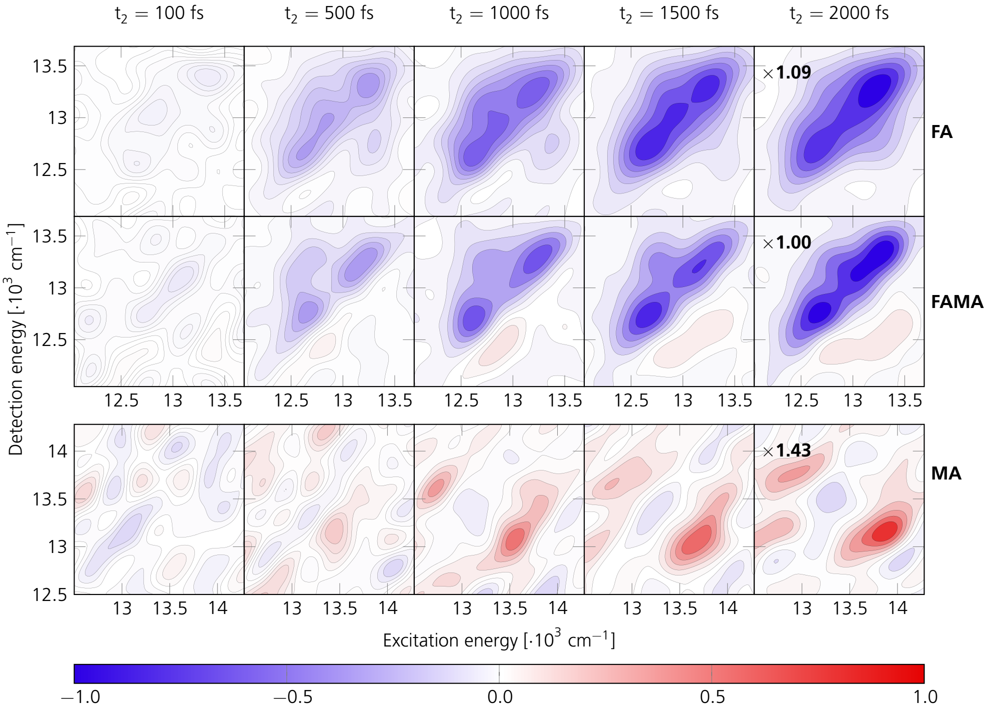

Figure 6.6: **Time evolution of incoherent-mixing–suppressed 2D maps.** Time-resolved 2D spectra for the three devices are shown, with the first, second, and third rows corresponding to FA, FAMA, and MA, respectively. At each population time t_2, the displayed map is the difference relative to the 50 fs map, which suppresses t_2-independent backgrounds (incoherent mixing) and highlights features that rise or decay over time. For direct comparison across devices, the 2 ps maps are scaled to the amplitude of the FAMA map. Figure adapted from **Paper IV**.

temporal evolution of the 2D maps for each sample. To highlight regions that evolve with population time, we adopt a differential procedure: the earliest map (50 fs, with negligible pulse-overlap artifacts) is subtracted from all subsequent maps. This subtraction suppresses static backgrounds, particularly incoherent-mixing component which is assumed to be constant over the timescale investigated, thereby enhancing the visibility of genuine population dynamics and relaxation processes and enabling a qualitative interpretation of the excited-state behavior. For $t_2 > 50$ fs, all 2D spectra develop clear, time-evolving structure across the three perovskite devices. A distinct, positive, elongated response grows below the main diagonal. This off-diagonal feature reports intraband cooling: photoexcited carriers relax from higher-lying conduction-band states within the excitation bandwidth toward the band edge. At 2 ps, all spectra have evolved: the previously diagonal-leaning elongation evolves into a more horizontal feature, which informs that the carrier distribution has approached a quasi-equilibrium near the CB minimum; this evolution is a hallmark of carrier thermalization and relaxation. In the FA sample, the positive cross-peak at lower detection energies is noticeably attenuated relative to the other compositions. We attribute this reduction to spectral congestion: overlapping lineshapes from multiple contributions diminish the apparent cross-peak amplitude. In fig. 6.6 are reported the temporal evolution

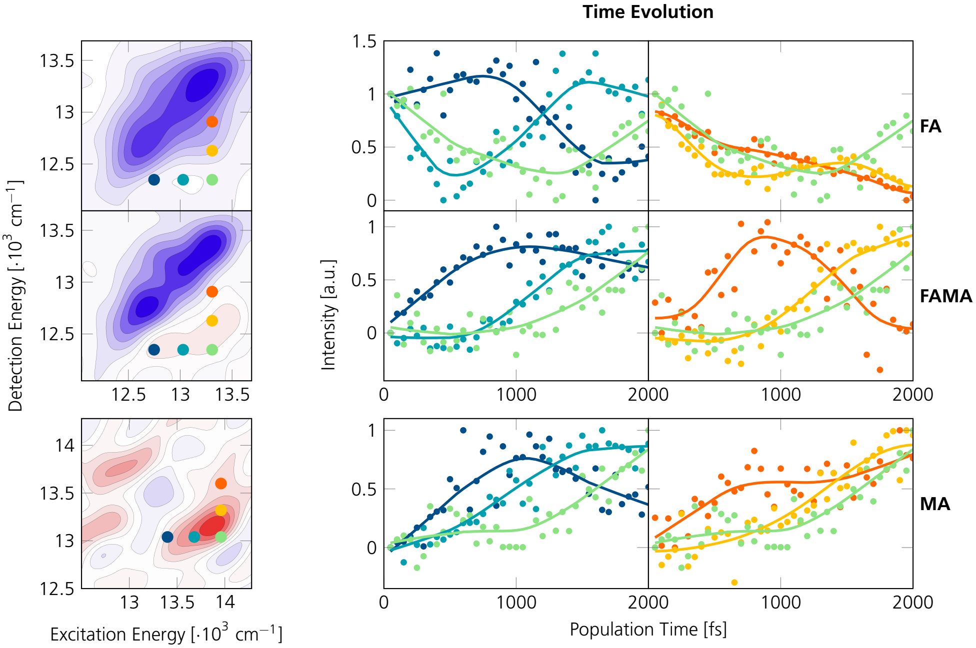

Figure 6.7: **Tracking carrier dynamics with PC-2DES across PSCs with different organic A-cation composition.** On the left, Two-dimensional frequency-domain maps at population time of 2 ps for the FA, FAMA, and MA devices. Colored markers indicate selected excitation–detection coordinates that probe specific regions of the conduction band. On the right side are reported the time evolution of the signal amplitude at each marked coordinate associated with each sample, respectively. Dots represent experimental data; solid curves are kinetic-model fits. All traces are normalized to facilitate direct comparison. Figure adapted from **Paper IV**.

of conduction band populations monitored at different excitation and detection energies for each device, thereby visualizing how the A-site cation influences charge dynamics. By sampling points near the band edge, it becomes evident that quasi-resonant excitation at photon energies close to the fundamental gap (blue marker) promotes electrons from the valence band directly into states near the conduction band minimum, which is populated essentially instantaneously, indicating rapid carrier injection.

In contrast, as the excitation photon energy is increased from quasi-resonant conditions (blue marker) toward higher-lying conduction-band states (light-green marker), carriers are injected initially into higher conduction-band levels. The population subsequently relaxes to the band-edge with a discernible delay that grows with excitation energy. This behavior reflects energy-dependent cooling: carriers promoted to higher energies must dissipate additional excess energy (predominantly via phonon emission) before reaching the band edge. Consequently, observe delay in growing off-diagonal feature correlates directly with the vertical energy offset between the initial excitation and the band-edge. Analogously, examining the time-resolved response along the detection energy axis at fixed excitation reveals a clear temporal progression of population inside the conduction band. Signals at higher detection energies (red marker) rise earlier, whereas those at lower detection energies (toward the light-green marker) emerge with increasing delay. This sequential onset evidences a cascade-like relaxation pathway in which photoexcited carriers occupy higher-energy CB states first and then relax stepwise toward the band-edge. The progressive delay at lower detection energies thus provides a direct visualization of intraband cooling. To translate the qualitative trends into a quantitative framework, we developed a kinetic model to interpret the measured dynamics, which has been applied to the MA PSCs dataset.

6.3.1 Theory and kinetic model

We consider a sequence of four phase-controlled, ultrashort optical pulses with adjustable delays (t_1, t_2, t_3). Phase modulation is employed to isolate signals arising from Liouville pathways in which each pulse interacts once with the system; one such pathway is illustrated in fig. 6.8. The time-integrated photocurrent can be expressed as:

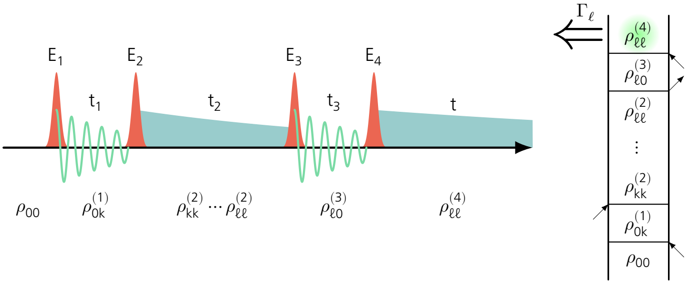

Figure 6.8: Conceptual illustration of photocurrent-detected coherent multidimensional spectroscopy. Four femtosecond pulses (E_i, i= $1, 2, 3, 4$) interact with the sample. Beginning from the equilibrium density matrix ρ_{00}, the pulse sequence drives the system through Liouville-space pathways; the pathway shown corresponds to stimulated emission pathway for rephasing, with the associated double-sided Feynman diagram reproduced on the right. After the fourth interaction, the system resides in a population state, and the measurable photocurrent is obtained by adding up all possible $\Gamma_\ell \rho_{\ell\ell}(t)$ and integrating over time, where Γ_ℓ denotes the extraction efficiency of population $\rho_{\ell\ell}$. FT along the coherence and detection delays, t_1 and t_3, yield the excitation and detection frequencies (ω_1 and ω_3) of the 2D spectrum. During the population time t_2, system–bath interactions drive relaxation; the resulting population time dependence of the 2D spectra provides detailed insight into carrier thermalization and recombination dynamics. Figure adapted from **Paper IV**.

$$I_{PC}(t_1, t_2, t_3) \propto \sum_l \Gamma_l \int \rho_{ll}^{(4)}(t_1, t_2, t_3, t)dt \tag{6.3}$$

where $\rho_l^{(4)}$ is the fourth-order population of level l, and Γ_l denotes the photocurrent extraction efficiency of that population. The value of Γ_l is particularly consequential for ESA pathways that end in doubly excited manifolds after the fourth pulse: in highly efficient devices, double excitation can yield approximately twice the photocurrent of a single excitation (in other words, $\Gamma \approx 2$ for doubly excited states and $\Gamma \approx 1$ for singly excited states). In contrast, efficient Auger recombination can reduce the effective Γ of doubly excited states toward unity, while trap states contribute negligibly with $\Gamma = 0$, which would result as positive ESA feature, opposite to its negative appearance.

A FT along the first coherence time t_1 provides the excitation frequency ω_1 within the pulse bandwidth, with resolution set by the scan length and by material dephasing. For sufficiently long scans, the material's dephasing determines the effective spectral selectivity. To model the continuum of perovskite absorption encompassed by the pulse, we discretize it into L equally spaced levels whose initial populations follow the pulse spectrum. Population dynamics during t_2 are described as phonon-assisted scattering governed by the spectral density $\sigma(\omega)$ of phonon modes coupled to the electronic transition. Considering one-phonon processes, the downhill (relaxation) transition rate from level m to n with gap $\omega_{mn} = E_m - E_n > 0$ is:

$$k_{m \to n} \propto [N(\omega_{mn}) + 1]\sigma(\omega_{mn}) \tag{6.4}$$

where $N(\omega)$ is the Bose–Einstein occupation. The corresponding uphill (re-absorption) rate is:

$$k_{n \to m} \propto N(\omega_{mn})\sigma(\omega_{mn}) \tag{6.5}$$

which satisfies detailed balance and drives relaxation toward thermal equilibrium. The discretized energy-level scheme and the literature-derived spectral density used in the simulations are summarized in fig. 6.9 [140–142]. A FT over the detection delay t_3 yields the detection frequency ω_3 of the 2D spectrum. During t_3, the system resides in a third-order coherence that evolves in the presence of photoexcitations and photocarriers created by the preceding pulses. This evolution is well described by the semiconductor Bloch equations (SBE). [143,144] Taking a ground–excited coherence ρ_{l0}, its equation of motion reads

$$\frac{d\rho_{l0}}{dt} = -(\gamma_0 + \sum_k \gamma'_k \rho_{kk})\rho_{l0} + i(\omega_{l0} + \sum_k \omega'_k \rho_{kk})\rho_{l0} + i\mu_{0l} E(t)(\rho_{ll} - \rho_{00}) \tag{6.6}$$

where γ_0 is the bath-induced dephasing rate, γ'_k captures additional dephasing induced by excited-state and carrier populations ρ_{kk}, ω_{l0} is the transition frequency, ω'_k accounts for population-induced frequency shifts, μ_{0l} is the transition dipole, and $E(t)$ is the laser electric field. Summarizing, The first term on the right-hand side describes dephasing (including population-dependent broadening), the second term encodes frequency renormalization (population-induced shifts), and the third term describes light–matter coupling.

In the simulations, diagonal populations ρ_{ll} are initialized from the laser spectrum and subsequently propagated by numerically integrating the master equations. Many-body effects captured by the SBE manifest as line broadening and spectral shifts. Phenomenologically, we include an additive, population-dependent term in the signal,

$$\Delta S_{ij}(t) = A_{ij} e^{-t/\tau_{\mathrm{relax}}}, \tag{6.7}$$

primarily attributed to exciton dissociation into free carriers, which reflects the line broadening and spectral shifts induced by many-effects in SBE model. Electronic relaxation is

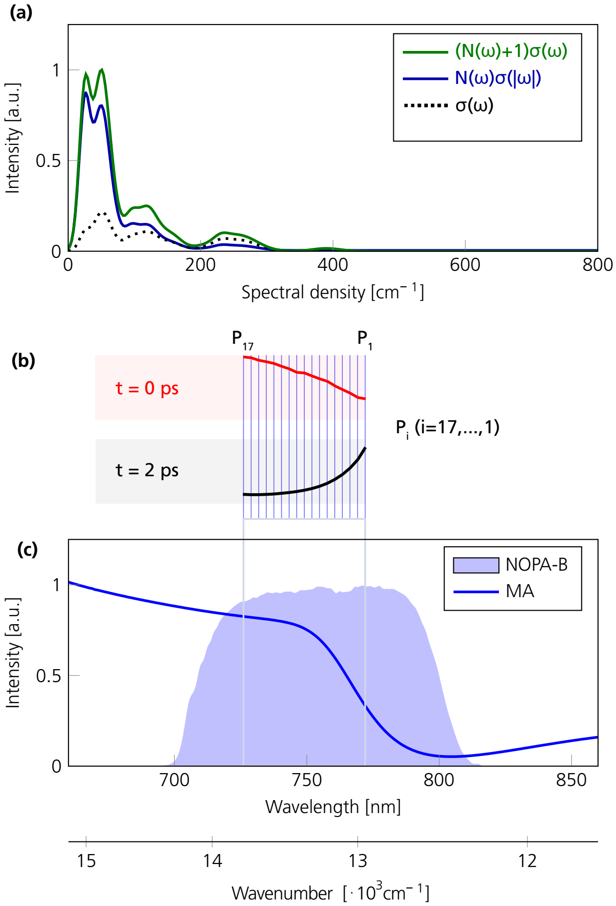

Figure 6.9: Spectral modeling and level scheme for MAPbI$_3$. (a) Simulated Raman spectra of MAPbI$_3$ thin films. (b) Schematic of the discretized 17-level conduction-band manifold; simulated populations are shown at t= 0 (immediately after laser excitation) and at t= 2ps. (c) Noncollinear optical parametric amplifier (NOPA-B) excitation spectrum overlaid with the steady-state absorption of MAPbI$_3$ thin films. Figure adapted from **Paper IV**.

modeled on a 17-level conduction-band (CB) ladder indexed $i = 1, 2, \ldots, 17$ from the band minimum upward, with uniform spacing $\delta = 50\ \mathrm{cm}^{-1}$.

The phonon-assisted relaxation is inferred from a simulated Stokes (Raman) spectrum $I(\tilde{\nu})$, represented as a sum of Gaussian modes centered at $\tilde{\nu}_m$ with full width at half maximum (FWHM) Γ_m and amplitude A_m:[140–142]

$$I(\tilde{\nu}) = \sum_m A_m[N(\tilde{\nu}_m, T) + 1]\sigma(\tilde{\nu}; \tilde{\nu}_m, \Gamma_m) \tag{6.8}$$

where the normalized Gaussian line shape is

$$\sigma(\tilde{\nu};\tilde{\nu}_m,\Gamma_m)=\sqrt{\frac{4\ln 2}{\pi}}\frac{1}{\Gamma_m}e^{-\left[\frac{4\ln 2(\tilde{\nu}-\tilde{\nu}_m)^2}{\Gamma_m^2}\right]} \tag{6.9}$$

and the Bose–Einstein occupation is

$$N(\tilde{\nu},T)=\frac{1}{e^{\left(\frac{hc\tilde{\nu}}{k_\mathrm{B}T}\right)}-1} \tag{6.10}$$

where $hc = 1.23984\times10^{-4}$ eV·cm, $k_\mathrm{B} = 8.61733\times10^{-5}$ eV/K, and $T = 300$ K. The spectrum $I(\tilde{\nu})$ is evaluated on a dense grid $\tilde{\nu}\in[0,800]$ cm^{-1} and interpolated linearly at the discrete interlevel shifts:

$$\tilde{\nu}_{ij}\equiv\frac{E_i-E_j}{hc}=\delta(i-j)\qquad i>j \tag{6.11}$$

Downward (emission) rates are taken proportional to the Stokes intensity at the corresponding shift; the absolute scale is fixed by a reference nearest-neighbor relaxation from the 17th to 16th:

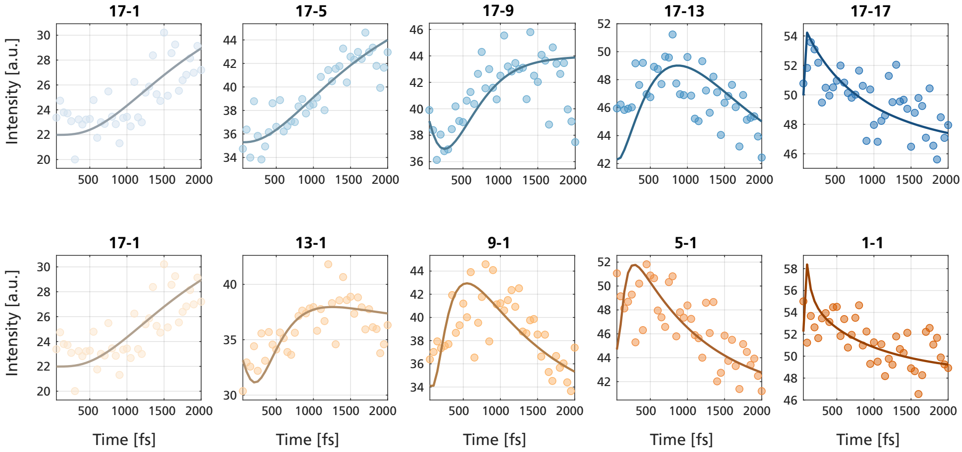

Figure 6.10: Fitting result for MA PSCs photocurrent detected dataset. The experimental raw data are plotted as scatter points, while the corresponding fits are shown as solid lines for different experimental excitation and detection conditions. Figure adapted from **Paper IV**.

$$k^{\downarrow}_{i\to j}=k_0 I(\tilde{\nu}_{ij})\qquad k_0=\frac{k^\mathrm{ref}_{17\to16}}{\tilde{\nu}_{17,16}} \tag{6.12}$$

and upward (absorption) rates follow detailed balance at temperature T:

$$k^{\uparrow}_{ji}=k^{\downarrow}_{i\to j}\frac{N(\tilde{\nu}_{ij},T)}{N(\tilde{\nu}*ij,T)+1}=k^{\downarrow}_{i\to j}e^{\left(-\frac{hc\tilde{\nu}_{ij}}{k_\mathrm{B}T}\right)} \tag{6.13}$$

The intricate set of coupled equations can be naturally formulated and solved within a master-equation framework. Let $P_i(t) = P_1(t), P_2(t), \ldots, P_{17}(t)^\top$ denote the level populations. The kinetic operator R (units ps^{-1}) collects all in- and out-fluxes:

$$\dot{P}_i(t) = RP_i(t) \tag{6.14}$$

with off-diagonal elements

$$R_{ji} = k^{\downarrow}_{i\to j} \quad i > j \tag{6.15}$$

$$R_{ij} = k^{\uparrow}_{j\to i} \quad i > j \tag{6.16}$$

and diagonal entries enforcing probability conservation

$$R_{ii} = -\sum_{j<i} k^{\downarrow}_{i\to j} - \sum_{j>i} k^{\uparrow}_{j\to i} \tag{6.17}$$

Thus R is a 17×17 generator with non-positive eigenvalues and column sums equal to zero. Under laser excitation, a source term distributes photoexcitation across the ladder according to the product of the laser spectrum and the perovskite absorption:

$$\dot{P}_i(t) = RP_i(t) + \alpha_i G(t) \qquad \alpha_i = \alpha_1, \alpha_2, \ldots, \alpha_{17} \tag{6.18}$$

where $G(t)$ prescribes the temporal envelope (and spectral weighting) of the pumping for each sublevel. By adopting this model, it was possible to determine the base relaxation rate:

$$k_{base} = 1.05 \cdot 10^{12}\mathrm{s}^{-1} \tag{6.19}$$

with the base rate ratio defined relative to $k^{\downarrow}_{17\to 16}$. The other phonon-mediated rates $k^{\downarrow}_{i\to j}$ and $k^{\uparrow}_{j\to i}$ were obtained by scaling k_{base} with the relative Raman spectral intensities. In addition, the effective relaxation rate was found to be:

Table 6.1: Values of A_{ij} associated to relevant transitions.

i	j	A_{ij}
17	1	0
17	5	0
17	9	200
17	13	125
17	17	561
17	1	0
13	1	250
9	1	150
5	1	100
1	1	100

$$k_{relax} = 1 \cdot 10^{9}\mathrm{s}^{-1} \tag{6.20}$$

The extracted coefficients A_{ij} for the relevant transitions are reported in tab. 6.1.

CHAPTER 7

Fluorescence detection: LHCII

Photosynthetic light harvesting begins with antenna complexes that capture photons and direct excitation energy to the reaction centers with high speed and fidelity. Among these, light-harvesting complex II (LHCII) is the principal antenna of Photosystem II (PSII) in plant thylakoid membranes, where it serves as both the principal collector of solar photons and a versatile regulator of excitation pressure. Structurally, LHCII is a trimer of homologous Lhcb1–Lhcb3 subunits; each monomer binds fourteen chlorophylls (eight a and six b) and four carotenoids arranged in a highly conserved topology that underpins both rapid energy transfer and efficient photoprotection. Its trimeric protein scaffold positions chlorophylls *a* and *b* (Chl *a* and Chl *b*), together with carotenoids, to broaden absorption in the Q_y region and to promote rapid, directed energy transfer on sub-picosecond to picosecond timescales. Beyond capture and funneling, LHCII also modulates energy flow through photoprotective pathways and state transitions, ensuring efficient operation across changing light conditions. In this chapter, we first describe the architecture and photophysical roles of LHCII and then present the main results of **Paper V**, which reports low-temperature measurements on LHCII using C-2DES and A-2DES. The side-by-side comparison at cryogenic temperature highlights the complementary information content of field-detected versus fluorescence-detected signals, with C-2DES resolving the time evolution of diagonal and cross peaks associated with energy relaxation, and A-2DES reporting incoherent mixing signatures, thereby providing a consolidated view of excitonic structure and dynamics in LHCII.

7.1 Introduction to LHCII

The LHCII stands as the most abundant antenna complex in higher plants and green algae, playing a crucial role in the initial capture of solar energy and its efficient transfer to the photosynthetic reaction centers.[145] This intricate pigment-protein complex is not merely a passive light collector but a highly dynamic entity, central to both the efficiency of photosynthesis and the crucial photoprotective mechanisms that safeguard the photosynthetic apparatus from excessive light energy.

Its multifaceted nature has been a subject of extensive research, revealing layers of structural sophistication and functional adaptability. The primary function of LHCII involves the absorption of photons across a broad spectrum of visible light and the subsequent funneling of this excitation energy to PSII. This process relies on a precise arrangement of chlorophylls (Chl) and carotenoids (Car) within the protein scaffold. The detailed architecture of LHCII, including the specific binding sites and interactions of its constituent pigments, has been progressively unveiled through advanced structural biology techniques.[146–151] The efficient energy transfer within LHCII is driven by Förster Resonance Energy Transfer (FRET) and other coherent mechanisms. Spectroscopic investigations have been instrumental in dissecting these ultrafast processes.[152–157] Beyond its role in light harvesting, LHCII is indispensable for photoprotection, a critical process that prevents photodamage when light absorption exceeds the capacity for photosynthetic electron transport. This involves the dynamic regulation of energy dissipation, primarily through a process known as Non-Photochemical Quenching (NPQ). NPQ is a complex mechanism that involves conformational changes within LHCII, leading to the formation of quenched states where excess excitation energy is safely dissipated as heat, rather than being transferred to the reaction centers where it could generate harmful reactive oxygen species.[158–162] The dynamic nature of LHCII extends to its ability to undergo reversible phosphorylation, a key

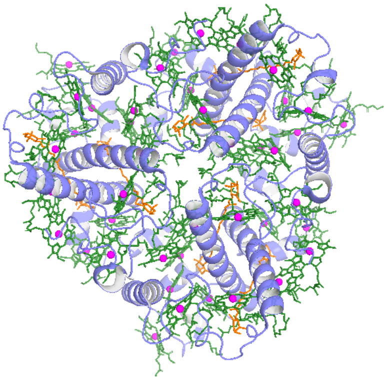

Figure 7.1: LHCII. Cartoon of LHCII structure. Image produced with PyMOL software.

regulatory mechanism that modulates its association with PSII and Photosystem I (PSI), thereby balancing excitation energy distribution between the two photosystems. This process, known as state transitions, ensures optimal light utilization under varying light conditions.[163] In addition, the ability of LHCII to dynamically adjust its light-harvesting capacity and energy dissipation pathways through its intricate regulatory networks is crucial for plant survival and productivity in fluctuating light environments.[164] The structural plasticity of LHCII is also evident in its ability to form various supramolecular organizations, ranging from monomeric units to trimers and larger aggregates, which can influence both light harvesting and photoprotection. The formation of these aggregates, often induced by changes in pH or lipid environment, is thought to be crucial for the induction of NPQ.[165–168] Furthermore, the efficiency and regulation of LHCII are critical for overall photosynthetic performance, impacting biomass production and plant resilience.[169–171] The ongoing investigation into LHCII, from its atomic structure to its dynamic regulation in living plants, underscores its central and complex role in sustaining life on Earth through the capture and conversion of solar energy.

7.2 Complementary insights into cryogenic LHCII dynamics: a comparative study of coherent and action-detected 2D electronic spectroscopies

C-2DES and A-2DES measurement were performed on LHCII at cryogenic temperature (78 K). Both modalities address the chlorophyll Q_y manifold, where LHCII exhibits the familiar Chl *b* band near 650 nm and Chl *a* near 675 nm. The excitation bandwidth was 100 nm, ensuring coverage of the structured Q_y band. In C-2DES the heterodyned third-order polarization was recorded and decomposed into rephasing and nonrephasing contributions. In A-2DES four phase-modulated pulse replicas were streamed by a Dazzler pulse shaper and fluorescence was detected to yield the action signal: the rephasing and

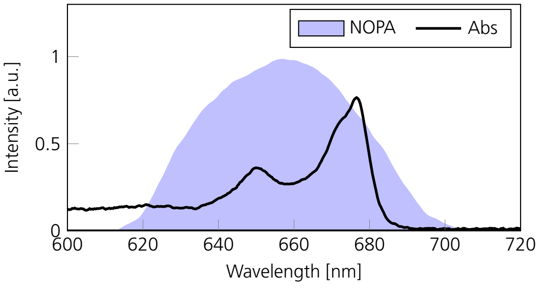

Figure 7.2: LHCII absorption spectrum and laser profile. The figure reports the linear absorption spectra for LHCII recorded at 78K (black solid line) with the laser profile covering the principal peaks (purple shaded area). Figure adapted from **Paper V**.

non-rephasing components were extracted by adopting the phase-modulation scheme. Coherence time was scanned identically across the two experiments to enable direct comparison. Fig. 7.2 presents the absorption spectrum together with the laser spectral profile. The low-temperature absorption recapitulates the canonical features of LHCII: in the Q_y region two dominant peaks are observed, with a band near 650 nm from Chl *b* and a band near 675 nm from Chl *a*, accompanied by a shoulder on the higher-energy (shorter-wavelength) side. A primary and critical result of this work was the identification and subsequent correction of a significant instrumental artifact inherent to the Dazzler-based A-2DES setup. Initial A-2DES spectra of LHCII display a dense pattern of cross-peaks that is inconsistent with the well-established photophysics of the complex, indicating significant instrumental aberrations. To obtain a high-resolution, artifact-free A-2DES dataset, we performed two

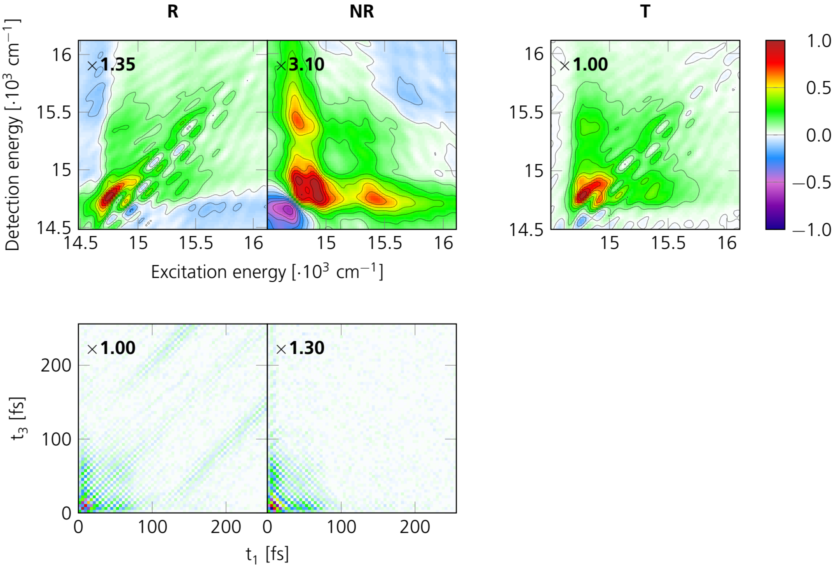

Figure 7.3: **A-2DES 2D maps in time- and frequency- domain displaying pulse shaper nonlinearity.** Time- (left) and frequency-domain (right) A-2DES 2D maps of LHCII measured at 78 K. Both R and NR display distortion effects arising from spurious nonlinear components due to limitations of the Dazzler pulse shaper. The nonlinearity affects more R signal, which is reflected also in the absorptive map (T) which is obtained by combining R and NR. Figure adapted from **Paper V**.

nominally identical measurements under the same optical settings: one with the sample present and one with only the glass cuvette acting as a scattering medium, while holding all other conditions fixed (temperature, pulse-shaper parameters, pulse energy at the sample position, and focused-spot size). Because a sample-free cuvette cannot generate a fourth-order molecular response, any structured signal in this control measurement can be unambiguously ascribed to instrumental artifacts. The scattering measurement, shown in fig.7.4, exhibits clear nonlinear structure in the time domain; following a 2D-FT, these produce spurious features that closely mimic genuine spectral signatures. The scattering control implicates the pulse shaper as the source of the spurious cross-peaks. In our data, these artifacts are most prominent at coherence times $t_{1,3} \gtrsim 100\,\text{fs}$; at shorter delays the maps are notably cleaner. The effect is strongly pathway dependent, which is pronounced in the rephasing (R) signal, where it produces conspicuous, diagonally aligned peaks, and much weaker for the nonrephasing (NR). Extending the population time beyond 300 fs the Dazzler-induced cross-peak artifact becomes weaker. Moreover, the diagonal stripe pattern in the time domain for the R signal evolves asymmetrically with the population time t_2 as the delay between the two pulse pairs increases.

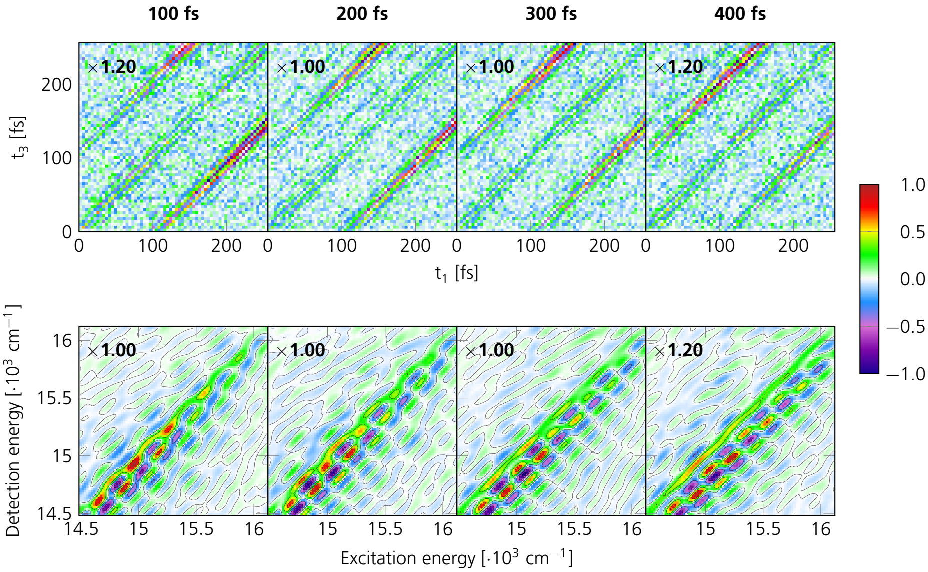

Figure 7.4: **Scattering A-2DES 2D maps in time- and frequency- domain displaying pulse shaper nonlinearity.** Evolution of nonlinear artifacts in the scattering control as a function of population time. As the population time t_2 increases, and therefore the temporal separation between the pump and probe waveform pairs streamed by the pulse shaper grows, the spurious nonlinear response systematically migrates toward higher excitation energies. Figure adapted from **Paper V**.

Restricting the analysis to the initial 100 fs suppresses most pulse-shaper artifacts, yielding a cleaner, easier-to-interpret map. The expected trade-off is diminished spectral resolution: narrow features coalesce, fine structure is blurred, and only two dominant peaks persist. Alternatively, it is possible to retain the full dataset by subtracting the time-domain 2D map from the scattering control from the corresponding sample map, for each population time t_2. This approach helps removing instrument-borne background and yielding a cleaned response. This subtraction is justified because the spurious features are effectively additive: for a given t_2 they appear at regular positions with fixed relative intensities.

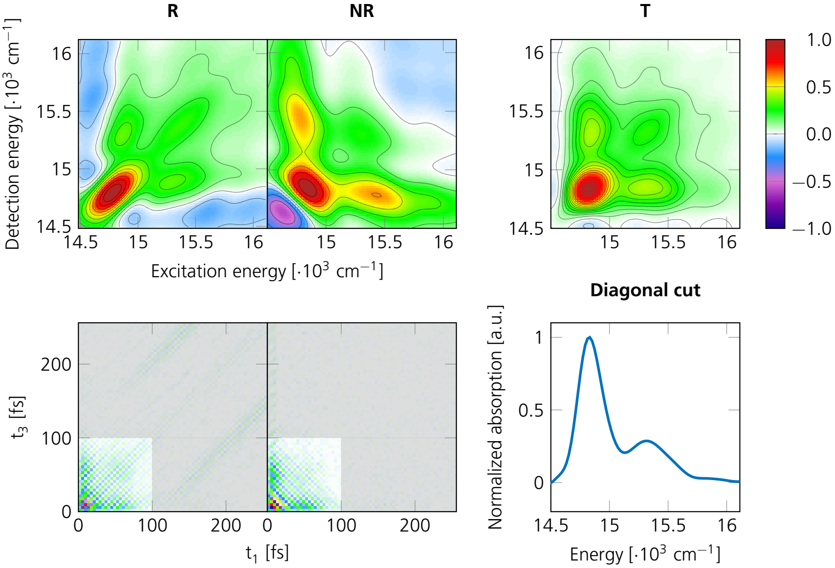

Figure 7.5: A-2DES 2D maps for by considering coherence time up to 100 fs. 2D dataset for R, NR and T by considering only time-domain dataset within the first 100 fs of coherence times (t1,3 < 100 fs). The 2D maps in frequency domain show clean features. However the fine resolution is lost, as visualized by the diagonal cut of T which now shows only 2 distinct features. Figure adapted from **Paper V**.

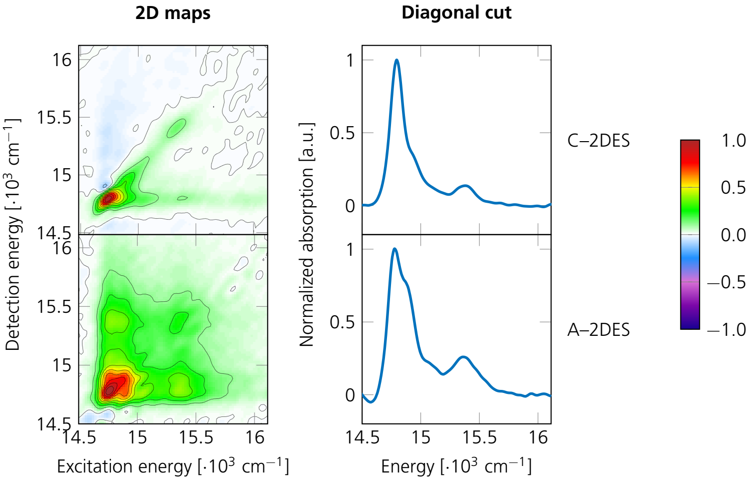

Figure 7.6: C-2DES and A-2DES 2D maps LHCII with diagonal cut. C-2DES (top row) and A-2DES (bottom row) 2D maps at population time of 200 fs with diagonal cut of the respective 2D maps. Figure adapted from **Paper V**.

At a population time of 200 fs, the C-2DES and A-2DES 2D maps showed fundamental analogies in their overall topology, both resolving the dominant excitonic peaks along the main diagonal at approximately 14800 cm^{-1}, 14900 cm^{-1}, 15100 cm^{-1}, and 15400 cm^{-1}, confirming the characteristic absorption properties of the chlorophylls, as displayed in fig. 7.6. Nevertheless, the differences between C-2DES and A-2DES are substantial and arise from their detection schemes. C-2DES captures the system's coherent response to the excitation pulses. Under the three-pulse interaction, three primary contributions are observed: ESA (negative), GSB (positive), and SE (positive). By contrast, A-2DES involves a fourth-field interaction. For GSB and SE (both positive) the pathways remain analogous

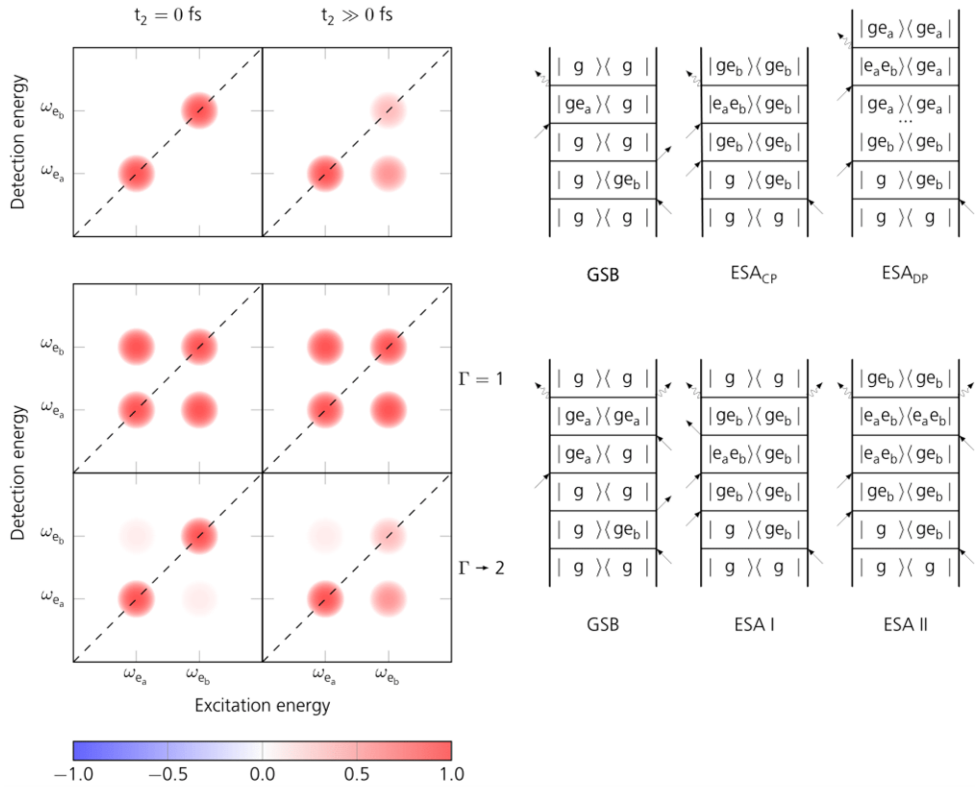

Figure 7.7: Schematic of R 2D spectra: C-2DES vs A-2DES for a coupled system. Top: C-2DES. At $t_2 = 0$ fs two diagonal peaks are present; at longer t_2 the upper diagonal feature weakens due to population relaxation from e_a (Chl *a*) to e_b (Chl *b*). Bottom: A-2DES, arising from incoherent mixing of excited-state populations. The mixing order Γ parameterizes the detection nonlinearity: for $\Gamma \approx 1$ (strong EEA), incomplete cancellation between ESA I and ESA II yields pronounced cross-peaks; as $\Gamma \rightarrow 2$ (no EEA), the A-2DES progressively resembles the C-2DES map. In the Feynman diagrams g refers to the common ground state, ge$_a$ to the situation on which Chl *a* is in the excited state and Chl *b* is in the ground state (and viceversa for ge$_b$), and e$_a$e$_b$ to the case in which both systems are in their excited state. Figure adapted from **Paper V**.

to C-2DES, but ESA splits into two pathways: ESA I (negative), in which the fourth interaction returns the system to the first excited state, and ESA II (positive), in which the fourth interaction promotes the system to a doubly excited state. The doubly excited manifold may correspond either to a higher electronic state of a single Chl or to a state with two distinct Chls excited. In the former case, rapid internal conversion funnels population to the lowest excited state, which subsequently emits. In the latter case, the presence of two excitations within the same antenna complex can lead to exciton–exciton annihilation, after which only one excitation remains. Since A-2DES detection integrates over comparatively long timescales, EEA has ample time to occur and can significantly influence the measured signal. Building on the distinctions above, EEA is a key nonradiative channel in multichromophoric systems, and the emergence of cross-peaks in action-detected 2D spectra provides a direct, sensitive readout of its efficiency: an effect commonly termed incoherent mixing. Mechanistically, the off-diagonal signal arises because EEA suppresses the ESA II pathway, breaking the otherwise perfect destructive interference with ESA I. In the ideal limit of uncoupled molecules with no annihilation, ESA II contributes with twice the amplitude and opposite sign relative to ESA I, yielding complete cancellation of the cross-peak. When EEA is operative, the quantum yield of ESA II is reduced and a net cross-peak remains. Although secondary factors (such as unequal oscillator strengths) can also lead to imperfect cancellation, EEA is often the dominant origin of these features in coupled aggregates. This ESA-cancellation behavior can be described by a phenomenological factor Γ that represents the effective quantum yield of ESA II: $\Gamma = 2$ when the doubly excited manifold contributes two units of signal (no annihilation), and $\Gamma = 1$ when annihilation is the exclusive decay pathway, yielding only one unit of signal.

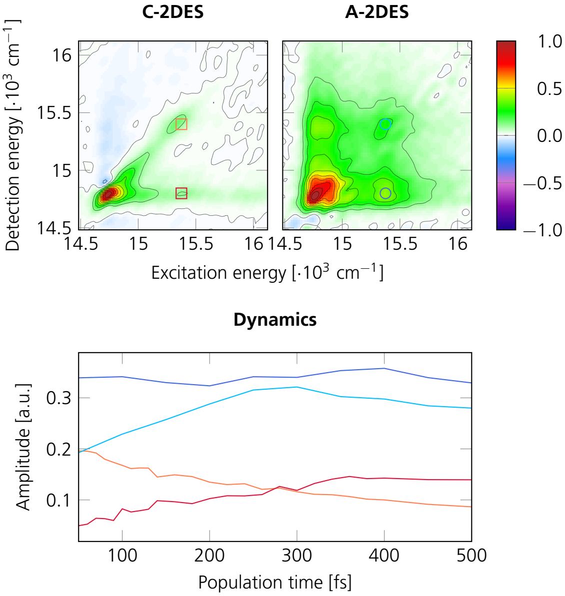

Figure 7.8: Dynamics of LHCII probed by C-2DES and A-2DES. C-2DES (top row) and A-2DES (bottom row) 2D maps at population time of 200 fs with diagonal cut of the respective 2D maps. Figure adapted from **Paper V**.

In fig. 7.8, C-2DES traces the expected population-time (t_2) evolution: upper-diagonal features associated with the higher-energy manifold decay as population relaxes toward the ground state; cross-peaks that report downhill transfer grow in; and the lower-energy diagonal band sharpens and intensifies at later t_2. By contrast, the A-2DES maps show minimal t_2 dependence. Incoherent mixing contributes a quasi-static background that obscures subtle population-time kinetics.

CHAPTER 8

Conclusion and Outlook

This work has successfully advanced the implementation and application of A-2DES, establishing a robust single-pulse-shaper methodology and leveraging it to investigate the primary photophysical processes in disparate yet significant systems: operational perovskite solar cells and LHCII. The development of the experimental apparatus necessitated a rigorous characterization of instrumental nonlinearities and artifacts, particularly those intrinsic to the AOPDF. Methodological strategies were devised and validated to mitigate these distortions, including precise data trimming protocols, power-dependent signal analysis, and a critical scattering-based background subtraction procedure. These technical refinements proved indispensable for obtaining high-fidelity data and were foundational to answer scientific questions, ensuring that the retrieved spectral dynamics accurately reflected the molecular response rather than instrumental imperfections. The application of photocurrent-detected 2DES to a series of high-efficiency perovskite solar cells provided direct insight into the influence of A-site cation composition on ultrafast charge carrier dynamics. By systematically varying the cation from pure formamidinium to methylammonium and a mixed-cation formulation, it was possible to trace the evolution of photoexcited carrier populations within the conduction band on a sub-picosecond timescale. The experiments revealed distinct carrier cooling and relaxation signatures contingent upon the perovskite composition, directly linking the initial energy dissipation pathways to the functional photocurrent output of the fully encapsulated devices. A detailed kinetic model, informed by the experimental data from the methylammonium-based device, quantitatively described the phonon-assisted intraband relaxation cascade, thereby bridging the gap between the microscopic scattering events and the macroscopic device response. In parallel, the investigation of the LHCII pigment-protein complex at cryogenic temperature through a comparative application of both coherent- and action-detected 2DES offered a powerful demonstration of the complementary nature of these techniques. Whereas C-2DES provided a clear visualization of population relaxation and downhill energy transfer between chlorophyll manifolds, the A-2DES spectra were dominated by features originating from incoherent mixing. This observation strongly indicated that the fluorescence-detected signal was profoundly influenced by many-body interactions, specifically efficient exciton-exciton annihilation, where incomplete suppression of the ESA Liouville pathways occurs, with the appearance of distinct spectral features. The side-by-side analysis underscored that while C-2DES maps the coherent evolution and energy flow, A-2DES serves as a highly sensitive probe of higher-order processes and excitonic interactions that govern the multichromophoric assembly. In synthesizing these findings, a central conclusion emerges: A-2DES is not merely a substitute for coherent detection but a distinct spectroscopic tool that provides unique access to the functional dynamics of complex systems. Its capacity to probe intact, operational optoelectronic devices and its inherent sensitivity to many-body interactions offer capabilities beyond those of conventional third-order techniques. The research presented herein establishes a validated framework for employing A-2DES and demonstrates its utility in resolving fundamental photophysical questions in both advanced materials and biological complexes, paving the way for future investigations into energy conversion and dissipation processes in ever more complex and heterogeneous environments.

References

[1] Maiman, T. H. Stimulated optical radiation in ruby. *Nature* **1960**, *187* (4736), 493 – 494.

[2] Zewail, A. H. Laser femtochemistry. *Science* **1988**, *242* (4886), 1645 – 1653.

[3] Wasielewski, M. R.; Johnson, D. G.; Seibert, M.; Govindjee. Determination of the primary charge separation rate in isolated photosystem II reaction centers with 500-fs time resolution. *PNAS* **1989**, *86* (2), 524 – 528.

[4] Hybl, J. D.; Albrecht, A. W.; Faeder, S. M. G.; Jonas, D. M. Two-dimensional electronic spectroscopy. *Chem. Phys. Lett.* **1998**, *297* (3 – 4), 307 – 313.

[5] Jonas, D. M. Two-dimensional femtosecond spectroscopy. *Annu. Rev. Phys. Chem.* **2003**, *54* (Volume 54, 2003), 425 – 463.

[6] Weiner, A. M. *Ultrafast Optics*; John Wiley & Sons, Inc.: Hoboken, NJ, USA, 2009.

[7] Planck, M. Ueber das Gesetz der Energieverteilung im Normalspectrum. *Ann. Phys.* **1901**, *309* (3), 553 – 563.

[8] Koch, T.; Bowers, J. Nature of wavelength chirping in directly modulated semiconductor lasers. *Electron. Lett.* **1984**, *20*, 1038 – 1040.

[9] Lazaridis, P.; Debarge, G.; Gallion, P. Time-bandwidth product of chirped sech^2 pulses: application to phase-amplitude-coupling factor measurement. *Opt. Lett.* **1995**, *20* (10), 1160 – 1162.

[10] Rullière, C. *Femtosecond Laser Pulses*; Springer: New York, NY, USA, 2005.

[11] Saleh, B. E. A.; Teich, M. C. *Fundamentals of Photonics*; John Wiley & Sons, Inc.: New York, NY, USA, 2007.

[12] Diels, J.-C.; Rudolph, W. *Ultrashort Laser Pulse Phenomena*, second edition ed.; Academic Press: Burlington, MA, USA, 2006.

[13] Träger, F. *Springer Handbook of Lasers and Optics*; Springer: New York, NY, USA, 2007.

[14] Thomson, R.; Leburn, C.; Reid, D. T. *Ultrafast Nonlinear Optics*; Springer: Heidelberg, Germany, 2013.

[15] Svelto, O. *Principles of Lasers*; Springer: New York, NY, USA, 2010.

[16] Trebino, R. *Frequency-Resolved Optical Gating: the Measurement of Ultrashort Laser Pulses*; Springer: New York, NY, USA, 2000.

[17] Grynberg, G.; Aspect, A.; Fabre, C. *Introduction to Quantum Optics: from the Semi-Classical Approach to Quantized Light*; Cambridge University Press: Cambridge, UK, 2010.

[18] Scully, M. O.; Zubairy, M. S. *Quantum Optics*; Cambridge University Press: Cambridge, UK, 1997.

[19] Boyd, R. W. *Nonlinear Optics*, 3rd ed.; Academic Press: Orlando, FL, USA, 2008.

[20] Bloembergen, N.; Pershan, P. S. Light waves at the boundary of nonlinear media. *Phys. Rev.* **1962**, *128*, 606 – 622.

[21] McHale, J. L. *Molecular Spectroscopy*, 2nd ed.; CRC Press: Boca Raton, FL, USA, 2017.

[22] Cho, M. *Two-Dimensional Optical Spectroscopy*; CRC Press: Boca Raton, FL, USA, 2009.

[23] Fano, U. Description of states in quantum mechanics by density matrix and operator techniques. *Rev. Mod. Phys.* **1957**, *29*, 74 – 93.

[24] Mukamel, S. *Principles of Nonlinear Optical Spectroscopy*; Oxford University Press: New York, NY, USA, 1995.

[25] Hamm, P.; Zanni, M. *Concepts and Methods of 2D Infrared Spectroscopy*; Cambridge University Press: Cambridge, UK, 2011.

[26] Dorfman, K. E.; Schlawin, F.; Mukamel, S. Nonlinear optical signals and spectroscopy with quantum light. *Rev. Mod. Phys.* **2016**, *88*, 045008.

[27] Perdomo-Ortiz, A.; Widom, J. R.; Lott, G. A.; Aspuru-Guzik, A.; Marcus, A. H. Conformation and electronic population transfer in membrane-supported self-assembled porphyrin dimers by 2D fluorescence spectroscopy. *J. Phys. Chem. B* **2012**, *116* (35), 10757 – 10770.

[28] Kubo, R. Statistical-mechanical theory of irreversible processes. I. General theory and simple applications to magnetic and conduction problems. *J. Phys. Soc. Jpn.* **1957**, *12* (6), 570 – 586.

[29] Malý, P.; Lüttig, J.; Müller, S.; Schreck, M. H.; Lambert, C.; Brixner, T. Coherently and fluorescence-detected two-dimensional electronic spectroscopy: direct comparison on squaraine dimers. *Phys. Chem. Chem. Phys.* **2020**, *22*, 21222 – 21237.

[30] Bruschi, M.; Gallina, F.; Fresch, B. Simulating action-2D electronic spectroscopy of quantum dots: insights on the exciton and biexciton interplay from detection-mode and time-gating. *Phys. Chem. Chem. Phys.* **2022**, *24*, 27645–27659.

[31] Kunsel, T.; Tiwari, V.; Matutes, Y. A.; Gardiner, A. T.; Cogdell, R. J.; Ogilvie, J. P.; Jansen, T. L. C. Simulating fluorescence-detected two-dimensional electronic spectroscopy of multichromophoric systems. *J. Phys. Chem. B* **2019**, *123* (2), 394 – 406.

[32] Schröter, M.; Pullerits, T.; Kühn, O. Using fluorescence detected two-dimensional spectroscopy to investigate initial exciton delocalization between coupled chromophores. *J. Chem. Phys.* **2018**, *149* (11), 114107.

[33] Agarwalla, B. K.; Harbola, U.; Hua, W.; Zhang, Y.; Mukamel, S. Coherent (photon) vs incoherent (current) detection of multidimensional optical signals from single molecules in open junctions. *J. Chem. Phys.* **2015**, *142* (21), 212445.

[34] Chen, Q.; Kwok, Y. H.; Zhou, W.; Chen, G.; Mukamel, S. Time-dependent simulation of photocurrent-detected two-dimensional spectroscopy of open systems. *J. Chem. Phys.* **2021**, *155* (19), 194113.

[35] Sun, H.; Harbola, U.; Mukamel, S.; Galperin, M. Two-dimensional spectroscopy of open quantum systems: nonequilibrium green's function formulation. *J. Phys. Chem. Lett.* **2025**, *16* (8), 2008 – 2015.

[36] Sidler, D.; Hamm, P. Feynman diagram description of 2D-Raman-THz spectroscopy applied to water. *J. Chem. Phys.* **2019**, *150* (4), 044202.

[37] Rose, P. A.; Krich, J. J. Automatic Feynman diagram generation for nonlinear optical spectroscopies and application to fifth-order spectroscopy with pulse overlaps. *J. Chem. Phys.* **2021**, *154* (3), 034109.

[38] Abramavičius, D. Revealing a full quantum ladder by nonlinear spectroscopy. *Lith. J. Phys.* **2020**, *60* (3).

[39] Tan, H.-S. Theory and phase-cycling scheme selection principles of collinear phase coherent multi-dimensional optical spectroscopy. *J. Chem. Phys.* **2008**, *129* (12), 124501.

[40] Kühn, O.; Mančal, T.; Pullerits, T. Interpreting fluorescence detected two-dimensional electronic spectroscopy. *J. Phys. Chem. Lett.* **2020**, *11* (3), 838 – 842.

[41] Tian, P.; Keusters, D.; Suzaki, Y.; Warren, W. S. Femtosecond phase-coherent two-dimensional spectroscopy. *Science* **2003**, *300* (5625), 1553 – 1555.

[42] Zhang, C.; Son, Y.; Kim, H.; Lee, S.-H.; Liang, X.; Fu, G.; Lee, S.-U.; Park, D.-A.; Jiang, Q.; Zhu, K.; Park, N.-G. Work function tuning of a weak adhesion homojunction for stable perovskite solar cells. *Joule* **2024**, *8* (5), 1394 – 1411.

[43] Tekavec, P. F.; Dyke, T. R.; Marcus, A. H. Wave packet interferometry and quantum state reconstruction by acousto-optic phase modulation. *J. Chem. Phys.* **2006**, *125* (19), 194303.

[44] Tekavec, P. F.; Lott, G. A.; Marcus, A. H. Fluorescence-detected two-dimensional electronic coherence spectroscopy by acousto-optic phase modulation. *J. Chem. Phys.* **2007**, *127* (21), 214307.

[45] Keusters, D.; Tan, H.-S.; Warren. Role of pulse phase and direction in two-dimensional optical spectroscopy. *J. Phys. Chem. A* **1999**, *103* (49), 10369 – 10380.

[46] Ernst, R. R.; Bodenhausen, G.; Wokaun, A. *Principles of Nuclear Magnetic Resonance in One and Two Dimensions*; Oxford University Press: 1990.

[47] Zuckerstätter, G.; Müller, N. Coherence pathway selection by cogwheel phase cycling in liquid-state NMR. *Concepts Magn. Reson. A* **2007**, *30A* (2), 81 – 99.

[48] Li, C.; Wagner, W.; Ciocca, M.; Warren, W. S. Multiphoton femtosecond phase-coherent two-dimensional electronic spectroscopy. *J. Chem. Phys.* **2007**, *126* (16), 164307.

[49] Jayachandran, A.; Müller, S.; Brixner, T. Cogwheel phase cycling in population-detected optical coherent multidimensional spectroscopy. *J. Chem. Phys.* **2024**, *161* (22), 224202.

[50] Wagner, W.; Li, C.; Semmlow, J.; Warren, W. S. Rapid phase-cycled two-dimensional optical spectroscopy in fluorescence and transmission mode. *Opt. Express* **2005**, *13* (10), 3697 – 3706.

[51] Roeding, S.; Brixner, T. Coherent two-dimensional electronic mass spectrometry. *Nat. Commun.* **2018**, *9* (1), 2519.

[52] Yan, S.; Tan, H.-S. Phase cycling schemes for two-dimensional optical spectroscopy with a pump–probe beam geometry. *Chem. Phys.* **2009**, *360* (1), 110 – 115.

[53] Zhang, Z.; Wells, K. L.; Hyland, E. W. J.; Tan, H.-S. Phase-cycling schemes for pump–probe beam geometry two-dimensional electronic spectroscopy. *Chem. Phys. Lett.* **2012**, *550*, 156 – 161.

[54] Cho, D.; Rouxel, J. R.; Kowalewski, M.; Saurabh, P.; Lee, J. Y.; Mukamel, S. Phase cycling RT-TDDFT simulation protocol for nonlinear XUV and X-ray molecular spectroscopy. *J. Phys. Chem. Lett.* **2018**, *9* (5), 1072 – 1078.

[55] Munoz, M. F.; Medina, A.; Autry, T. M.; Moody, G.; Siemens, M. E.; Bristow, A. D.; Cundiff, S. T.; Li, H. Fast phase cycling in non-collinear optical two-dimensional coherent spectroscopy. *Opt. Lett.* **2020**, *45* (20), 5852 – 5855.

[56] De, A. K.; Monahan, D.; Dawlaty, J. M.; Fleming, G. R. Two-dimensional fluorescence-detected coherent spectroscopy with absolute phasing by confocal imaging of a dynamic grating and 27-step phase-cycling. *J. Chem. Phys.* **2014**, *140* (19), 194201.

[57] Jayachandran, A.; Müller, S.; Brixner, T. Fluorescence-detected two-quantum photon echoes via cogwheel phase cycling. *J. Phys. Chem. Lett.* **2022**, *13* (50), 11710 – 11719.

[58] Damtie, F. A.; Wacker, A.; Pullerits, T. o.; Karki, K. J. Two-dimensional action spectroscopy of excitonic systems: Explicit simulation using a phase-modulation technique. *Phys. Rev. A* **2017**, *96*, 053830.

[59] Javed, A.; Lüttig, J.; Sanders, S. E.; Sessa, F.; Gardiner, A. T.; Joffre, M.; Ogilvie, J. P. Broadband rapid-scanning phase-modulated Fourier transform electronic spectroscopy. *Opt. Express* **2024**, *32* (16), 28035 – 28047.

[60] Nardin, G.; Autry, T. M.; Silverman, K. L.; Cundiff, S. T. Multidimensional coherent photocurrent spectroscopy of a semiconductor nanostructure. *Opt. Express* **2013**, *21* (23), 28617 – 28627.

[61] Lott, G. A.; Perdomo-Ortiz, A.; Utterback, J. K.; Widom, J. R.; Aspuru-Guzik, A.; Marcus, A. H. Conformation of self-assembled porphyrin dimers in liposome

vesicles by phase-modulation 2D fluorescence spectroscopy. *PNAS* **2011**, *108* (40), 16521 – 16526.

[62] Ekimov, A. I.; Onushchenko, A. A. Quantum size effect in three-dimensional microscopic semiconductor crystals. *JETP Lett.* **1981**, *34*, 345 – 349.

[63] Efros, A.; Efros, A. Interband light absorption in semiconductor spheres. *Sov. Phys. Semicond.* **1982**, *16* (7), 772 – 775.

[64] Brus, L. E. A simple model for the ionization potential, electron affinity, and aqueous redox potentials of small semiconductor crystallites. *J. Chem. Phys.* **1983**, *79* (11), 5566 – 5571.

[65] Bruchez Jr., M. Semiconductor nanocrystals as fluorescent biological labels. *Science* **1998**, *281* (5385), 2013 – 2016.

[66] Medintz, I. L.; Uyeda, H. T.; Goldman, E. R.; Mattoussi, H. Quantum dot bioconjugates for imaging, labelling and sensing. *Nat. Mater.* **2005**, *4* (6), 435 – 446.

[67] Kairdolf, B. A.; Smith, A. M.; Stokes, T. H.; Wang, M. D.; Young, A. N.; Nie, S. Semiconductor quantum dots for bioimaging and biodiagnostic applications. *Annu. Rev. Anal. Chem.* **2013**, *6* (1), 143 – 162.

[68] Colvin, V. L.; Schlamp, M. C.; Alivisatos, A. P. Light-emitting diodes made from cadmium selenide nanocrystals and a semiconducting polymer. *Nature* **1994**, *370* (6488), 354 – 357.

[69] Shirasaki, Y.; Supran, G. J.; Bawendi, M. G.; Bulović, V. Emergence of colloidal quantum-dot light-emitting technologies. *Nat. Photon.* **2013**, *7* (1), 13 – 23.

[70] Jang, E.; Jang, H. Quantum dot light-emitting diodes. *Chem. Rev.* **2023**, *123* (8), 4663 – 4692.

[71] Nozik, A. J. Quantum dot solar cells. *Phys. E: Low-Dimens. Syst. Nanostruct.* **2002**, *14* (1—2), 115 – 120.

[72] Nozik, A. J.; Beard, M. C.; Luther, J. M.; Law, M.; Ellingson, R. J.; Johnson, J. C. Semiconductor quantum dots and quantum dot arrays and applications of multiple exciton generation to third-generation photovoltaic solar cells. *Chem. Rev.* **2010**, *110* (11), 6873 – 6890.

[73] Carey, G. H.; Abdelhady, A. L.; Ning, Z.; Thon, S. M.; Bakr, O. M.; Sargent, E. H. Colloidal quantum dot solar cells. *Chem. Rev.* **2015**, *115* (23), 12732 – 12763.

[74] Jung, H.; Ahn, N.; Klimov, V. I. Prospects and challenges of colloidal quantum dot laser diodes. *Nat. Photon.* **2021**, *15* (9), 643 – 655.

[75] Park, Y.-S.; Roh, J.; Diroll, B. T.; Schaller, R. D.; Klimov, V. I. Colloidal quantum dot lasers. *Nat. Rev. Mater.* **2021**, *6* (5), 382 – 401.

[76] Rafailov, E. U.; Cataluna, M. A.; Sibbett, W. Mode-locked quantum-dot lasers. *Nat. Photon.* **2007**, *1* (7), 395 – 401.

[77] The Nobel Prize in Chemistry 2023. NobelPrize.org.

[78] Neeleshwar, S.; Chen, C. L.; Tsai, C. B.; Chen, Y. Y.; Chen, C. C.; Shyu, S. G.; Seehra, M. S. Size-dependent properties of CdSe quantum dots. *Phys. Rev. B* **2005**, *71*, 201307.

[79] Cordero, S. R.; Carson, P. J.; Estabrook, R. A.; Strouse, G. F.; Buratto, S. K. Photo-activated luminescence of CdSe quantum dot monolayers. *J. Phys. Chem. B* **2000**, *104* (51), 12137 – 12142.

[80] Klimov, V. I. Spectral and dynamical properties of multiexcitons in semiconductor nanocrystals. *Annu. Rev. Phys. Chem.* **2007**, *58* (1), 635 – 673.

[81] Davydov, A. S. *Theory of Molecular Excitons*, 1st ed.; Plenum Press: New York, NY, USA, 1971.

[82] Scholes, G. D.; Rumbles, G. Excitons in nanoscale systems. *Nat. Mater.* **2006**, *5* (9), 683 – 696.

[83] Dramićanin, M. *Luminescence Thermometry*; Elsevier: Amsterdam, NL, 2018.

[84] Klimov, V. I. *Nanocrystal Quantum Dots*, 2nd ed.; CRC Press: Boca Raton, FL, USA, 2017.

[85] Gaponenko, S. V. *Optical Properties of Semiconductor Nanocrystals*; Cambridge University Press: Cambridge, UK, 1998.

[86] Alivisatos, A. P. Semiconductor clusters, nanocrystals, and quantum dots. *Science* **1996**, *271* (5251), 933 – 937.

[87] Seibt, J.; Hansen, T.; Pullerits, T. 3D spectroscopy of vibrational coherences in quantum dots: theory. *J. Phys. Chem. B* **2013**, *117* (38), 11124 – 11133.

[88] Seibt, J.; Pullerits, T. Beating signals in 2D spectroscopy: electronic or nuclear coherences? Application to a quantum dot model system. *J. Phys. Chem. C* **2013**, *117* (36), 18728 – 18737.

[89] Shionoya, S.; Saito, H.; Hanamura, E.; Akimoto, O. Anisotropic excitonic molecules in CdS and CdSe. *Solid State Commun.* **1973**, *12* (3), 223 – 226.

[90] Achermann, M.; Hollingsworth, J. A.; Klimov, V. I. Multiexcitons confined within a subexcitonic volume: Spectroscopic and dynamical signatures of neutral and charged biexcitons in ultrasmall semiconductor nanocrystals. *Phys. Rev. B* **2003**, *68*, 245302.

[91] Oron, D.; Kazes, M.; Banin, U. Multiexcitons in type-II colloidal semiconductor quantum dots. *Phys. Rev. B* **2007**, *75*, 035330.

[92] Nanda, J.; Ivanov, S. A.; Achermann, M.; Bezel, I.; Piryatinski, A.; Klimov, V. I. Light amplification in the single-exciton regime using exciton-exciton repulsion in type-II nanocrystal quantum dots. *J. Phys. Chem. C* **2007**, *111* (42), 15382 – 15390.

[93] Ekimov, A. I.; Hache, F.; Schanne-Klein, M.; Ricard, D.; Flytzanis, C.; Kudryavtsev, I.; Yazeva, T.; Rodina, A.; Efros, A. L. Absorption and intensity-dependent photoluminescence measurements on CdSe quantum dots: assignment of the first electronic transitions. *Journal of the Optical Society of America B* **1993**, *10* (1), 100 – 107.

[94] Gao, Y.; Yin, P. Synthesis of cubic CdSe nanocrystals and their spectral properties. *Nanomater. Nanotech.* **2017**, *7*, 1847980417701747.

[95] Lenngren, N.; Abdellah, M. A.; Zheng, K.; Al-Marri, M. J.; Zigmantas, D.; Žídek, K.; Pullerits, T. Hot electron and hole dynamics in thiol-capped CdSe quantum dots revealed by 2D electronic spectroscopy. *Phys. Chem. Chem. Phys.* **2016**, *18*, 26199 – 26204.

[96] Wang, Z.; Lenngren, N.; Amarotti, E.; Hedse, A.; Zidek, K.; Zheng, K.; Zigmantas, D.; Pullerits, T. Excited states and their dynamics in cdse quantum dots studied by two-color 2D spectroscopy. *J. Phys. Chem. Lett.* **2022**, *13* (5), 1266 – 1271.

[97] Gelzinis, A.; Augulis, R.; Butkus, V.; Robert, B.; Valkunas, L. Two-dimensional spectroscopy for non-specialists. *Biochim. Biophys. Acta, Bioenerg.* **2019**, *1860* (4), 271 – 285.

[98] Augulis, R.; Zigmantas, D. Two-dimensional electronic spectroscopy with double modulation lock-in detection: enhancement of sensitivity and noise resistance. *Opt. Express.* **2011**, *19* (14), 13126 – 13133.

[99] Konar, A.; Sechrist, R.; Song, Y.; Policht, V. R.; Laible, P. D.; Bocian, D. F.; Holten, D.; Kirmaier, C.; Ogilvie, J. P. Electronic interactions in the bacterial reaction center revealed by two-color 2D electronic spectroscopy. *J. Phys. Chem. Lett.* **2018**, *9* (18), 5219 – 5225.

[100] Norris, D. J.; Bawendi, M. Measurement and assignment of the size-dependent optical spectrum in CdSe quantum dots. *Phys. Rev. B* **1996**, *53* (24), 16338.

[101] Wang, Z.; Hedse, A.; Amarotti, E.; Lenngren, N.; Žídek, K.; Zheng, K.; Zigmantas, D.; Pullerits, T. Beating signals in CdSe quantum dots measured by low-temperature 2D spectroscopy. *J. Chem. Phys.* **2022**, *157* (1).

[102] Rose, G. Ueber einige neue Mineralien des Urals. *Journal für praktische Chemie* **1840**, *19* (1), 459 – 468.

[103] Zhang, L.; Mei, L.; Wang, K.; Lv, Y.; Zhang, S.; Lian, Y.; Liu, X.; Ma, Z.; Xiao, G.; Liu, Q.; et al. Advances in the application of perovskite materials. *Nano-Micro Lett.* **2023**, *15* (1), 177.

[104] Choi, K. J.; Biegalski, M.; Li, Y.; Sharan, A.; Schubert, J.; Uecker, R.; Reiche, P.; Chen, Y.; Pan, X.; Gopalan, V.; et al. Enhancement of ferroelectricity in strained BaTiO3 thin films. *Science* **2004**, *306* (5698), 1005 – 1009.

[105] Wang, D.; Wang, G.; Lu, Z.; Al-Jlaihawi, Z.; Feteira, A. Crystal structure, phase transitions and photoferroelectric properties of KNbO3-based lead-free ferroelectric ceramics: a brief review. *Front. Mater.* **2020**, *7*, 91.

[106] Li, F.; Zhang, S.; Yang, T.; Xu, Z.; Zhang, N.; Liu, G.; Wang, J.; Wang, J.; Cheng, Z.; Ye, Z.-G.; et al. The origin of ultrahigh piezoelectricity in relaxor-ferroelectric solid solution crystals. *Nat. Commun.* **2016**, *7* (1), 13807.

[107] Zheng, T.; Wu, J.; Xiao, D.; Zhu, J. Recent development in lead-free perovskite piezoelectric bulk materials. *Prog. Mater. Sci.* **2018**, *98*, 552 – 624.

[108] Jin, S.; Tiefel, T. H.; McCormack, M.; Fastnacht, R. A.; Ramesh, R.; Chen, L. H. Thousandfold change in resistivity in magnetoresistive La-Ca-Mn-O films. *Science* **1994**, *264* (5157), 413 – 415.

[109] Rao, C. N. R.; Cheetham, A. K. Giant magnetoresistance in transition metal oxides. *Science* **1996**, *272* (5260), 369 – 370.

[110] Maeno, Y.; Hashimoto, H.; Yoshida, K.; Nishizaki, S.; Fujita, T.; Bednorz, J.; Lichtenberg, F. Superconductivity in a layered perovskite without copper. *Nature* **1994**, *372* (6506), 532 – 534.

[111] Wenk, H.-R.; Bulakh, A. *Minerals: their Constitution and Origin*; Cambridge University Press: Cambridge, 2004.

[112] Kim, J. Y.; Lee, J.-W.; Jung, H. S.; Shin, H.; Park, N.-G. High-efficiency perovskite solar cells. *Chem. Rev.* **2020**, *120* (15), 7867 – 7918.

[113] O'regan, B.; Grätzel, M. A low-cost, high-efficiency solar cell based on dye-sensitized colloidal TiO2 films. *Nature* **1991**, *353* (6346), 737 – 740.

[114] Kojima, A.; Teshima, K.; Shirai, Y.; Miyasaka, T. Organometal halide perovskites as visible-light sensitizers for photovoltaic cells. *J. Am. Chem. Soc.* **2009**, *131* (17), 6050 – 6051.

[115] Im, J.-H.; Lee, C.-R.; Lee, J.-W.; Park, S.-W.; Park, N.-G. 6.5% efficient perovskite quantum-dot-sensitized solar cell. *Nanoscale* **2011**, *3* (10), 4088 – 4093.

[116] Kim, H.-S.; Lee, C.-R.; Im, J.-H.; Lee, K.-B.; Moehl, T.; Marchioro, A.; Moon, S.-J.; Humphry-Baker, R.; Yum, J.-H.; Moser, J. E.; et al. Lead iodide perovskite sensitized all-solid-state submicron thin film mesoscopic solar cell with efficiency exceeding 9%. *Sci. Rep.* **2012**, *2* (1), 591.

[117] Lee, M. M.; Teuscher, J.; Miyasaka, T.; Murakami, T. N.; Snaith, H. J. Efficient hybrid solar cells based on meso-superstructured organometal halide perovskites. *science* **2012**, *338* (6107), 643 – 647.

[118] Tan, Z.-K.; Moghaddam, R. S.; Lai, M. L.; Docampo, P.; Higler, R.; Deschler, F.; Price, M.; Sadhanala, A.; Pazos, L. M.; Credgington, D.; et al. Bright light-emitting diodes based on organometal halide perovskite. *Nat. Nanotechnol.* **2014**, *9* (9), 687 – 692.

[119] Kim, Y.-H.; Cho, H.; Heo, J. H.; Kim, T.-S.; Myoung, N.; Lee, C.-L.; Im, S. H.; Lee, T.-W. Multicolored organic/inorganic hybrid perovskite light-emitting diodes. *Adv. Mater.* **2015**, *27* (7), 1248 – 1254.

[120] Dou, L.; Yang, Y.; You, J.; Hong, Z.; Chang, W.-H.; Li, G.; Yang, Y. Solution-processed hybrid perovskite photodetectors with high detectivity. *Nat. Commun.* **2014**, *5* (1), 5404.

[121] Ahmadi, M.; Wu, T.; Hu, B. A review on organic–inorganic halide perovskite photodetectors: device engineering and fundamental physics. *Adv. Mater.* **2017**, *29* (41), 1605242.

[122] Kieslich, G.; Sun, S.; Cheetham, A. K. Solid-state principles applied to organic–inorganic perovskites: new tricks for an old dog. *Chem. Sci.* **2014**, *5* (12), 4712 – 4715.

[123] Park, N.-G. Perovskite solar cells: an emerging photovoltaic technology. *Mater. today* **2015**, *18* (2), 65 – 72.

[124] Goldschmidt, V. M. Die Gesetze der Krystallochemie. *Naturwissenschaften* **1926**, *14* (21), 477 – 485.

[125] Li, C.; Lu, X.; Ding, W.; Feng, L.; Gao, Y.; Guo, Z. Formability of abx3 (x= f, cl, br, i) halide perovskites. *Structural Science* **2008**, *64* (6), 702 – 707.

[126] Leguy, A. M.; Frost, J. M.; McMahon, A. P.; Sakai, V. G.; Kockelmann, W.; Law, C.; Li, X.; Foglia, F.; Walsh, A.; O'regan, B. C.; et al. The dynamics of methylammonium ions in hybrid organic–inorganic perovskite solar cells. *Nat. Commun.* **2015**, *6* (1), 7124.

[127] Zhu, H.; Miyata, K.; Fu, Y.; Wang, J.; Joshi, P. P.; Niesner, D.; Williams, K. W.; Jin, S.; Zhu, X.-Y. Screening in crystalline liquids protects energetic carriers in hybrid perovskites. *Science* **2016**, *353* (6306), 1409 – 1413.

[128] Chen, T.; Chen, W.-L.; Foley, B. J.; Lee, J.; Ruff, J. P. C.; Ko, J. Y. P.; Brown, C. M.; Harriger, L. W.; Zhang, D.; Park, C.; Yoon, M.; Chang, Y.-M.; Choi, J. J.; Lee, S.-H. Origin of long lifetime of band-edge charge carriers in organic–inorganic lead iodide perovskites. *PNAS* **2017**, *114* (29), 7519 – 7524.

[129] Eperon, G. E.; Stranks, S. D.; Menelaou, C.; Johnston, M. B.; Herz, L. M.; Snaith, H. J. Formamidinium lead trihalide: a broadly tunable perovskite for efficient planar heterojunction solar cells. *Energy Environ. Sci.* **2014**, *7*, 982 – 988.

[130] Kubicki, D. J.; Prochowicz, D.; Hofstetter, A.; Pechy, P.; Zakeeruddin, S. M.; Gratzel, M.; Emsley, L. Cation dynamics in mixed-cation (MA) x (FA) 1–x PbI3 hybrid perovskites from solid-state NMR. *J. Am. Chem. Soc.* **2017**, *139* (29), 10055 – 10061.

[131] Kubicki, D. J.; Prochowicz, D.; Hofstetter, A.; Saski, M.; Yadav, P.; Bi, D.; Pellet, N.; Lewinski, J.; Zakeeruddin, S. M.; Gratzel, M.; et al. Formation of stable mixed guanidinium–methylammonium phases with exceptionally long carrier lifetimes for high-efficiency lead iodide-based perovskite photovoltaics. *J. Am. Chem. Soc.* **2018**, *140* (9), 3345 – 3351.

[132] Ma, F.; Li, J.; Li, W.; Lin, N.; Wang, L.; Qiao, J. Stable α/δ phase junction of formamidinium lead iodide perovskites for enhanced near-infrared emission. *Chem. Sci.* **2017**, *8*, 800 – 805.

[133] Chen, T.; Foley, B. J.; Park, C.; Brown, C. M.; Harriger, L. W.; Lee, J.; Ruff, J.; Yoon, M.; Choi, J. J.; Lee, S.-H. Entropy-driven structural transition and kinetic trapping in formamidinium lead iodide perovskite. *Sci. Adv.* **2016**, *2* (10), e1601650.

[134] Lee, J.-W.; Kim, D.-H.; Kim, H.-S.; Seo, S.-W.; Cho, S. M.; Park, N.-G. Formamidinium and cesium hybridization for photo-and moisture-stable perovskite solar cell. *Adv. Energy Mater.* **2015**, *5* (20), 1501310.

[135] Lin, J.; Lai, M.; Dou, L.; Kley, C. S.; Chen, H.; Peng, F.; Sun, J.; Lu, D.; Hawks, S. A.; Xie, C.; et al. Thermochromic halide perovskite solar cells. *Nat. Mater.* **2018**, *17* (3), 261 – 267.

[136] Park, N.-G. Perovskite Solar Cell: Research Direction for Next 10 Years. *ACS Energy Lett.* **2019**, *4* (12), 2983 – 2985.

[137] NREL. Best research-cell efficiencies. **2025**.

[138] Jeon, N. J.; Na, H.; Jung, E. H.; Yang, T.-Y.; Lee, Y. G.; Kim, G.; Shin, H.-W.; Il Seok, S.; Lee, J.; Seo, J. A fluorene-terminated hole-transporting material for highly efficient and stable perovskite solar cells. *Nat. Energy* **2018**, *3* (8), 682 – 689.

[139] Kim, G.-H.; Kim, D. S. Development of perovskite solar cells with >25conversion efficiency. *Joule* **2021**, *5* (5), 1033–1035.

[140] Quarti, C.; Grancini, G.; Mosconi, E.; Bruno, P.; Ball, J. M.; Lee, M. M.; Snaith, H. J.; Petrozza, A.; De Angelis, F. The Raman Spectrum of the CH3NH3PbI3 Hybrid Perovskite: Interplay of Theory and Experiment. *J. Phys. Chem. Lett.* **2014**, *5* (2), 279 – 284.

[141] Lin, W.; Liang, M.; Niu, Y.; Chen, Z.; Cherasse, M.; Meng, J.; Zou, X.; Zhao, Q.; Geng, H.; Papalazarou, E.; Marsi, M.; Perfetti, L.; Canton, S. E.; Zheng, K.; Pullerits, T. Combining two-photon photoemission and transient absorption spectroscopy to resolve hot carrier cooling in 2D perovskite single crystals: the effect of surface layer. *J. Mater. Chem. C* **2022**, *10*, 16751 – 16760.

[142] Rosenkampff, I.; Pullerits, T. Microcavity-enhanced exciton dynamics in light-harvesting complexes: insights from Redfield theory. *J. Chem. Phys.* **2025**, *163* (4), 044305.

[143] Shacklette, J. M.; Cundiff, S. T. Role of excitation-induced shift in the coherent optical response of semiconductors. *Phys. Rev. B* **2002**, *66*, 045309.

[144] Li, X.; Zhang, T.; Borca, C. N.; Cundiff, S. T. Many-body interactions in semiconductors probed by optical two-dimensional Fourier transform spectroscopy. *Phys. Rev. Lett.* **2006**, *96* (5), 057406.

[145] Croce, R.; van Grondelle, R.; van Amerongen, H.; van Stokkum, I. *Light Harvesting in Photosynthesis*, 1st ed.; CRC Press: 2018.

[146] Müller, P.; Li, X.-P.; Niyogi, K. K. Non-photochemical quenching. A response to excess light energy. *Plant Physiol.* **2001**, *125* (4), 1558 – 1566.

[147] Pascal, A. A.; Liu, Z.; Broess, K.; van Oort, B. F.; van Amerongen, H.; Wang, C.; Horton, P.; Robert, B.; Chang, W.; Ruban, A. V. Molecular basis of photoprotection and control of photosynthetic light-harvesting. *Nature* **2005**, *436* (7047), 134 – 137.

[148] Holt, N. E.; Zigmantas, D.; Valkunas, L.; Li, X.-P.; Niyogi, K. K.; Fleming, G. R. Carotenoid cation formation and the regulation of photosynthetic light harvesting. *Science* **2005**, *307* (5708), 433 – 436.

[149] Wang, W.; Yu, L.-J.; Xu, C.; Tomizaki, T.; Zhao, S.; Umena, Y.; Chen, X.; Qin, X.; Xin, Y.; Suga, M.; Han, G.; Kuang, T.; Shen, J.-R. Structural basis for blue-green light harvesting and energy dissipation in diatoms. *Science* **2019**, *363* (6427), eaav0365.

[150] Zheng, M.; Pang, X.; Chen, M.; Tian, L. Ultrafast energy quenching mechanism of LHCSR3-dependent photoprotection in Chlamydomonas. *Nat. Commun.* **2024**, *15* (1), 4437.

[151] Accomasso, D.; Londi, G.; Cupellini, L.; Mennucci, B. The nature of carotenoid S* state and its role in the nonphotochemical quenching of plants. *Nat. Commun.* **2024**, *15*, 847.

[152] van Oort, B.; Marechal, A.; Ruban, A. V.; Robert, B.; Pascal, A. A.; de Ruijter, N. C.; van Grondelle, R.; van Amerongen, H. Different crystal morphologies lead to slightly different conformations of light-harvesting complex II as monitored by variations of the intrinsic fluorescence lifetime. *Phys. Chem. Chem. Phys.* **2011**, *13* (27), 12614 – 12622.

[153] Van Oort, B.; Van Grondelle, R.; Van Stokkum, I. H. A hidden state in light-harvesting complex II revealed by multipulse spectroscopy. *J. Phys. Chem. B* **2015**, *119* (16), 5184 – 5193.

[154] Wells, K. L.; Lambrev, P. H.; Zhang, Z.; Garab, G.; Tan, H.-S. Pathways of energy transfer in LHCII revealed by room-temperature 2D electronic spectroscopy. *Phys. Chem. Chem. Phys.* **2014**, *16* (23), 11640 – 11646.

[155] Ostroumov, E. E.; Götze, J. P.; Reus, M.; Lambrev, P. H.; Holzwarth, A. R. Characterization of fluorescent chlorophyll charge-transfer states as intermediates in the excited state quenching of light-harvesting complex II. *Photosynth. Res.* **2020**, *144* (2), 171 – 193.

[156] Son, M.; Moya, R.; Pinnola, A.; Bassi, R.; Schlau-Cohen, G. S. Protein–protein interactions induce pH–dependent and zeaxanthin-independent photoprotection in the plant light-harvesting complex, LHCII. *J. Am. Chem. Soc.* **2021**, *143* (42), 17577 – 17586.

[157] Wu, Y.; Zheng, Y.; Yang, H.; Sun, C.; Dong, Y.; Cui, C.; Yan, H.; Li, Y. Rationally pairing photoactive materials for high-performance polymer solar cells with efficiency of 16.53%. *Sci. China Chem.* **2020**, *63* (2), 265 – 271.

[158] Ruban, A. V.; Johnson, M. P.; Duffy, C. D. The photoprotective molecular switch in the photosystem II antenna. *Biochim. Biophys. Acta – Bioenerg.* **2012**, *1817* (1), 167 – 181.

[159] Dall'Osto, L.; Cazzaniga, S.; Bressan, M.; Paleček, D.; Židek, K.; Niyogi, K. K.; Fleming, G. R.; Zigmantas, D.; Bassi, R. Two mechanisms for dissipation of excess light in monomeric and trimeric light-harvesting complexes. *Nat. Plants.* **2017**, *3* (5), 1 – 9.

[160] Dinc, E.; Tian, L.; Roy, L. M.; Roth, R.; Goodenough, U.; Croce, R. LHCSR1 induces a fast and reversible pH-dependent fluorescence quenching in LHCII in Chlamydomonas reinhardtii cells. *PNAS* **2016**, *113* (27), 7673 – 7678.

[161] Bode, S.; Quentmeier, C. C.; Liao, P.-N.; Hafi, N.; Barros, T.; Wilk, L.; Bittner, F.; Walla, P. J. On the regulation of photosynthesis by excitonic interactions between carotenoids and chlorophylls. *PNAS* **2009**, *106* (30), 12311 – 12316.

[162] Mascoli, V.; Liguori, N.; Xu, P.; Roy, L. M.; van Stokkum, I. H.; Croce, R. Capturing the quenching mechanism of light-harvesting complexes of plants by zooming in on the ensemble. *Chem* **2019**, *5* (11), 2900 – 2912.

[163] Johnson, M. P.; Ruban, A. V. Photoprotective energy dissipation in higher plants involves alteration of the excited state energy of the emitting chlorophyll (s) in the light harvesting antenna II (LHCII). *J. Biol. Chem.* **2009**, *284* (35), 23592 – 23601.

[164] Croce, R.; Carmo-Silva, E.; Cho, Y. B.; Ermakova, M.; Harbinson, J.; Lawson, T.; McCormick, A. J.; Niyogi, K. K.; Ort, D. R.; Patel-Tupper, D.; et al. Perspectives on improving photosynthesis to increase crop yield. *The plant cell* **2024**, *36* (10), 3944 – 3973.

[165] Liguori, N.; Periole, X.; Marrink, S. J.; Croce, R. From light-harvesting to photoprotection: structural basis of the dynamic switch of the major antenna complex of plants (LHCII). *Sci. Rep.* **2015**, *5* (1), 15661.

[166] Liguori, N.; Xu, P.; Van Stokkum, I. H.; Van Oort, B.; Lu, Y.; Karcher, D.; Bock, R.; Croce, R. Different carotenoid conformations have distinct functions in light-harvesting regulation in plants. *Nat. Commun.* **2017**, *8* (1), 1994.

[167] Son, M.; Pinnola, A.; Gordon, S. C.; Bassi, R.; Schlau-Cohen, G. S. Observation of dissipative chlorophyll-to-carotenoid energy transfer in light-harvesting complex II in membrane nanodiscs. *Nat. Commun.* **2020**, *11* (1), 1295.

[168] Harris, J. R.; Marles-Wright, J. *Macromolecular Protein Complexes IV: Structure and Function*; volume 99. Springer, Cham: 2022.

[169] Najafpour, M. M.; Shen, J.-R.; Allakhverdiev, S. I. Natural and artificial photosynthesis: fundamentals, progress, and challenges. *Photosynth. Res.* **2022**, *154* (3), 229 – 231.

[170] Zaks, J.; Amarnath, K.; Sylak-Glassman, E. J.; Fleming, G. R. Models and measurements of energy-dependent quenching. *Photosynth. Res.* **2013**, *116* (2), 389 – 409.

[171] Structural analysis and comparison of light-harvesting complexes I and II. *Biochim. Biophys. Acta – Bioenerg.* **2020**, *1861* (4), 148038.

Acknowledgments

After four and a half years in Lund, and countless fikas, it is time for me to close this wonderful chapter. I still remember arriving and thinking, “A PhD is so long,” and now I look back and wonder how it passed so quickly. Perhaps Vasco Rossi is right: *la vita è un brivido che vola via…* (life is a shiver that flies away). Moving from Italy to Sweden was more than a change of address. Yet I feel extremely lucky: I left one familiar home to find another, a family shaped by mentors, expert scientists, generous colleagues, and, most important, friends. I hope to not forget anyone because, really, all the people that contribute to my journey in the past four years are enormous.

First and foremost, I would like to thank my supervisor, Tõnu, for giving me this precious opportunity. I will never be able to express enough gratitude for the wealth of experiences you made possible for me, from deep discussions on cutting-edge scientific questions to the chance to travel, attend conferences, and broaden my horizons around the world. I have always been amazed by your ability to describe the most complex concepts into a few simple, clear words. Your sharp insights and thoughtful comments have challenged me, guided me, and helped me grow in ways I could not have imagined. A special thanks also to Prof. Elisabetta Collini for encouraging me to start this experience in Lund. However, during my journey I always felt surrounded by many other supervisors, each of whom shaped me in their own way. Donatas, thank you from the bottom of my heart for the countless hours of training in the lab and the laughter we shared along the way. Almost everything I know about how to move with confidence in the laboratory, and above all about what it truly means to obtain data of real quality, because every measurement done with you was simply outstanding, I owe to you. Words will never be enough to express my gratitude for the privilege of working side by side with you, and for the gift of calling you a friend. Arkady, thank you for the fruitful discussions that deepened my understanding of physical concepts, and not least for the spirited football debates! I would also like to thank Dmitry, that wonderfully fun person who sometimes tries (not always successfully!) to hide behind the serious role of PI in our division. I will truly miss your ever-ready jokes and young spirit. I have no doubt that your scientific skills will guide you toward a brilliant and successful career. I also wish to thank Ivan, Jens, Kaibo, Pavel, Junsheng and Ebbe for the many stimulating discussions and the joyful moments we shared together in the division. I extend my sincere gratitude to Prof. Nam-Gyu Park for his generous hospitality and for introducing me to the intricacies of solar-cell fabrication. I would like to acknowledge Prof. Niek van Hulst for the nice feedbacks and for welcoming me into your group for my next chapter as a postdoctoral researcher. Last, but by no means least, thank you, Luca for supervising me: for your time, your expertise, and above all your patience. Thank you for unlocking the secrets of action spectroscopy and for not letting me sink during this journey, unlike that one time in the river. Beyond my supervisors, I owe special thanks to Christine and Susanne, whose unfailing support made my journey at Lund University as smooth as possible. A big thanks to Torbjörn for his insightful technical discussions and for developing the custom-built tool that enabled the experiments leading to this work.

Now I would like to thank all the special people I met during my journey in Lund, that contribute in making this experience unforgivable. To my colleagues, Amitav, Prasenjit, Fan, Yong, Saurabh, Ahmed, Alexander, Chandni, Lintang, Yen, Qinying, Chen, Zhengjun, Lukas, Gioele, Klara, Eglè, Christina, Boris, Sudipta, Lidia and Nils, thank you for the stimulating conversations, the quick help when things went sideways, the shared protocols and tips, and the good humor that made long days lighter. I am grateful to have learned alongside you. A sincere thanks to all my long time colleagues and friends. Edoardo, thank you for welcoming me to the division and for sharing so many memorable adventures in that first year, with your wise suggestions and your legendary gin & tonics. Weihua, thank you for welcoming me to our office, the *Tofu Box*, for all the good chats, and for the games you taught us. I am going to miss you a lot and remember: I am saving the head massages for the next time we meet. Yanmei, thank you for all the fun in the division and for your contagious smile and laugh. I wish you the brilliant future that is already waiting for you. Sankaran, thank you for all our great talks about science and life. I admire your passion for research and your always kind manner. I am sure you will become a wonderful PI, and your students will love working with you. You truly deserve it my friend. Qi, thank you for the many conversations and for the time you devoted to modeling the perovskite data. Much of this work's success is thanks to you. I wish you all the best. Zehan, thank you for brightening our dark winters with your jokes and spirit: everyone should be lucky enough to have a colleague like you. Wishing you the very best in your career. Axl: thank you for showing me just how fun a Swedish person can be! You are a wonderful and caring person, and I am sure you will achieve wonderful things ahead. Now a special thanks to my lab friends. Ajeet, I really admire your broad scientific knowledge and your curiosity. It was a joy to work with you and share a few drinks. Thank you for your help in the lab and for all the good laughs. I cannot wait to meet again in the future. Maurice, although we had only a year, I am truly grateful for that time. Your kindness, sharp mind, and quiet humor made my days better. I wish you the very best for your PhD, and I hope we meet again soon. I would also like to thank all the colleagues and friends who made my secondment in South Korea truly unforgettable. Special thanks to Dong-Ho, Sun-Ho, Sang-Uk, and Dong-Nam for the warm welcome, the help in the lab, and all the fun times inside and outside it. I am truly thankful for the people I met along the way at conferences or that came to visit our division: acquaintances became companions, and companions became dear friends. Matteo B., we have known each other since my master's thesis, and since then I can hardly go a week without talking to you. From the very first day I had a gut feeling I had found a true friend. Thank you for all the lovely times at conferences and for our many fruitful discussions about 2D. You are truly brilliant, my friend. I hope one day we will live closer and share many more moments together. Dominik, even if we have known briefly during your visit here in Lund I am grateful to have been knowing you since then. Your incredible intuitions and passion for science amaze me. I hope we can play chess and share our science more frequently in our near future. Matthias, a Viking with a warm heart: a sharp scientist and one of the funniest people I know. Thank you for your kindness and laughs. And finally, you, Julian. I struggle to put into words how much I care and admire you. You are tall in every way that matters: height, heart, and humor. Your dark jokes and that contagious, laugh could bring joy everywhere. I am truly sad you left science; you would have been an amazing professor. But beyond the lab, I am just grateful our lives crossed. Thanks for the top-shelf reach, the bottom-of-the-heart friendship, and everything in between.

Now, a special thanks to the people who made my time outside the lab truly special, filling evenings and weekends with laughter, warmth, and friendship. A big thanks to the *after gym session* crew. Matteo T., thank you for all the amazing time we spent together, from kebab nights to our storage-locking adventures, and countless little moments in between. You brought light and energy to my Swedish days, and I am going to miss you so much. To me, you are a one-of-a-kind person, with immense knowledge that spans from science to history and politics. You always find the right words, and you have magic hands in the kitchen. I hope we will see each other often; please know I will always be there for you. And of course, thanks for all our *coffee break*. Su, you are lucky to be the partner of this wonderful person, but only because you are just as wonderful yourself. Thank you for the steady moral support of these past years. Thank you for opening your home, for the long talks, the shared meals, and the calm advice. You guys made me feel like family. My door is always open for you. Shraddha, my special *human bean*. I feel so lucky to have met you and to have shared these years in Lund, from wild parties in Vildanden to trips across Europe. It is hard to think we will not see each other as often, but I want to remain part of your life and keep finding ways to meet, laugh, and make new memories. You have a big heart and an even bigger kindness. You carry others with care, and you've carried me more times than you know. Thank you. Stay foolish, stay Shraddha. Then to my Brazilian friends, Dani and Matheus. Dani, thank you for bringing joy and energy to the division and to all of us. Your smile was always there, and always contagious. You are easy to talk to, you listen with care, and you make people feel at home. Big heart, big smile: that's you. I wish you a wonderful future in your academic career. Matheus, I don't know what I'll do without you. Your face gives the headline before anyone speaks, and your body language is a live commentary I never want to miss. I admire your transparency, but even more and the sensitive, kind person it reveals after scratching the surface. I will never forget when you tried to teach me how to move the shoulders in *dos que tres* and fell off the chair (10/10 for passion, 0/10 for stability). Let's keep making stories:more trips, more music, more laughs. I'm grateful for you. Stay exactly as you are. A loud thank you to my music friends, Albin, Romain, Miguel, Lorenzo, Karolis, and all the members of *The Funktional Group* for the jams, gigs, and countless laughs. Thank you for tolerating my inability to keep quiet during rehearsals. A special thank you to Albin, who shared more of his time with me than anyone else during my PhD. I will always remember how much we both grew over these years. Thank you for your friendship, your steady support, and all the good times, trips, and laughs. Your voice and bass lines were the soundtrack of this journey. I wish you all the best as you bring your PhD to a brilliant finish. Special thanks to Romain as well, for the great times in the division, and the even better ones on our trips. To Tova, Fredrik, Marie, Carmina, Julia, Mark, Filippo, and Marzo: thank you for all the fun we shared in Lund. From spontaneous dinners to long walks and laughter that brightened both dark winters and bright summer nights, you turned free time into memories I will always keep. To my friends of a lifetime in Casale Monferrato, Padova, and Rhêmes: thank you for growing up with me, for the midnight calls and Sunday coffees, for the jokes that never get old, and for reminding me who I am no matter how far I wander. My deepest thanks go to my brother, Giacomo (the real doctor) to my parents, Giuseppe and Cristina. Whoever I am, I owe largely to your care, your patience, and your love. I am equally grateful to my uncles, Michele, Silvio and Chicca, and to all my family for widening my horizons and helping me see the world from new angles. I love you. Finally, a special thank you to Neus. I struggle to put into words what I feel for you. Brilliant and intelligent, but never loud about it. Full of kindness, patience, courage, and curiosity. Around her, everyone feel safe and warm. With your gentle words and small, loving gestures, you made me believe in love again. You bring calm to my worries, light to my days, and laughter to the quiet moments. This is the greatest gift I carry from this journey. I cannot wait to build our future together. *T'estimo molt.*